

공학박사 학위논문

**Studies on Electrochemical Synthesis
of Graphene-based Nanostructured
Materials for Energy Storage and
Conversion Applications**

에너지 저장과 전환을 위한 그래핀 기반
나노구조물질의 전기화학 합성 연구

2020년 8월

서울대학교 융합과학기술대학원

융합과학부 나노융합전공

고 동 진

Studies on Electrochemical Synthesis of Graphene-based Nanostructured Materials for Energy Storage and Conversion Applications

지도 교수 박 원 철

이 논문을 공학박사 학위논문으로 제출함
2020년 7월

서울대학교 융합과학기술대학원
융합과학부 나노융합전공
고 동 진

고동진의 공학박사 학위논문을 인준함
2020년 7월

위 원 장	_____	(인)
부위원장	_____	(인)
위 원	_____	(인)
위 원	_____	(인)
위 원	_____	(인)

Abstract

Studies on Electrochemical Synthesis of Graphene-based Nanostructured Materials for Energy Storage and Conversion Applications

Dongjin Ko

Program in Nano Science and Technology

Graduate School of Convergence Science & Technology Seoul
National University

Over the past decade, graphene-based nanomaterials have attracted significant research interest for their potential application in energy storage/conversion devices. However, the high cost and low supply limit their use in practical energy storage/conversion applications. Chemical synthesis is regarded as a scalable and

low-cost process to produce graphene and graphene nanoribbons (GNRs), but the method involves the use of strong oxidants, which may cause explosion risk and serious environmental pollution.

Recently, electrochemical processes have been explored as an attractive approach to prepare graphene-based materials because of their eco-friendly nature, and easy scalability. In this thesis, I aim to describe the electrochemical preparation of graphene and GNRs and their use in energy storage/conversion applications (*i.e.*, Li-ion batteries and electrocatalyst for hydrogen evolution reactions).

The first section of this thesis is dedicated to the electrochemical exfoliation of graphite into graphene. Electrochemically exfoliated graphene (EG) is used as a microwave susceptor to prepare a carbon-coated silicon-graphene nanocomposite film. The graphene absorbed the microwave radiation and generated heat which reduced the oxidized graphene and carbonized the polydopamine carbon precursor on the silicon nanoparticles. The

prepared carbon-coated silicon–graphene nanocomposite was used as a lithium-ion battery anode.

The electrochemical process was then extended to the preparation of a GNR. Previously, anodic oxidation in diluted sulfuric acid was used to unzip multi-walled carbon nanotubes (MWCNTs). However, several reports have shown that this method is incapable of selective unzipping. In this study, for the first time, electrochemical unzipping is performed by anodic oxidation of MWCNTs in concentrated sulfuric acid. When the MWCNTs are anodically oxidized in a concentrated acid electrolyte, they become longitudinally unzipped to form GNRs. Thus, the as-prepared GNRs were used as an anode for alkali ion capacitors in both organic and aqueous electrolytes and MoS₂ catalyst support for the hydrogen evolution reaction.

This thesis provides details of the electrochemical methods used to prepare graphene and GNRs. Such methods may pave the path for industrial production and applications of graphene and GNRs at a low cost.

Keywords: Electrochemical method, Graphene, Graphene nanoribbon,
Lithium ion battery, Hydrogen evolution reaction, Microwave

Student Number: 2014-24837

Contents

Chapter 1. Introduction

1.1. Graphene and graphene nanoribbon	25
1.2. Application of graphene and graphene nanoribbon for energy storage and conversion devices.	31
1.2.1. Active material	31
1.2.2. Inactive material	36
1.3 Synthesis strategies for graphene and graphene nanoribbon.....	41
1.3.1. Preparation of graphene.....	42
1.3.2. Preparation of graphene nanoribbon	48

1.4. Electrochemical method	49
1.4.1. Intercalation-functionalization.....	53
1.4.2. Electrochemical unzipping of graphene nanoribbon	58
1.5. Thesis Overview	64
1.6. Reference	66

Chapter 2. Electrochemically Exfoliated Graphene as a Novel Microwave Susceptor: the Ultrafast Microwave- assisted Synthesis of Carbon-coated Silicon- graphene Film as Lithium-ion Battery Anode

2.1. Introduction.....	75
2.2. Experimental Method.....	79

2.3. Results and discussion	84
2.4. Conclusion	111
2.5. References.....	112

Chapter 3. Facile and Scalable Approach to Develop Electrochemical Unzipping of Multi-walled Carbon Nanotubes to Graphene Nanoribbons

3.1. Introduction.....	117
3.2. Experimental Method.....	121
3.3. Results and discussion	131
3.4. Conclusion	174
3.5. References.....	176

Chapter 4. Conclusion and outlook181

국문 초록 (Abstract in Korean)	184
---	-----

List of Figures

Figure 1.1. Classification of carbon allotropes (from Ref. [4]).....

29

Figure 1.2. (a) Graphene can be wrapped up into 0D fullerenes, rolled into 1D nanotubes, stacked into 3D graphite, (b) cut into graphene quantum dots, sliced into nanoribbons or drilled to form holey graphene (from Refs. [9] and [10])30

Figure 1.3. Schematic illustration of the first LIBs ($\text{LiCoO}_2/\text{Li}^+$ electrolyte/graphite) (from Ref. [25]).....33

Figure 1.4. Schematic illustration of an electric double-layer capacitor (EDLC).....

36

Figure 1.5. Major graphene fabrication methods (from Ref.

[44]).....	43
Figure 1.6. Schematic representation of the liquid exfoliation process: a) intercalation, b) ion exchange and c) ultrasonic exfoliation (from Ref. [45]).	47
Figure 1.7. Preparation of reduced graphene oxide from graphite (from Ref. [46])	47
Figure 1.8. Various MWCNTs unzipping methods (from Ref. [48]).....	49
Figure 1.9. Schematic overview of cathodic and anodic exfoliation (from Ref. [57]).....	53
Figure 1.10. Mechanism of functionalized graphite formation (or graphite oxide in (a)	
Figure 1.11. Anodic oxidation methods for preparing graphite oxide (from Refs. [81, 8	
Figure 1.12. Production of few-layered graphene by the electrochemical method (fr	
Figure 2.1. Schematic illustration of a synthesis procedure for microwave irradiated polydopamine-coated silicon-	

electrochemically exfoliated graphene film (MWpSi-EG).....8

7

Figure 2.2. (a) AFM image on SiO₂ substrate and (b) thickness distribution of anodically exfoliated graphene (50 flakes)87

Figure 2.3. (a) Wide scan XPS spectra and (b) Raman analysis of EG.....

88

Figure 2.4. Digital photo images of a microwave irradiation process for pSi-EG. The yellow arrow indicates a red arc.....8

8

Figure 2.5. Digital photo image of pSi-EG and MWpSi-EG.8

Figure 2.6. SEM image of the surface of MWpSi-EG with low magnification. The yellow arrows indicate micro-sized bumps.....89

Figure 2.7. Surface SEM image of (a,b) Si-EG, (d,e) MWSi-EG and (g,h) MWpSi-EG with low and high magnification. Cross-sectional SEM image of (c) Si-EG, (f) MWSi-EG and (i) MWpSi-EG.....91

Figure 2.8. SEM image of the exposed surface of (a) MWSi-EG and (b) Si-EG.....91

Figure 2.9. HR-TEM images of MWpSi-EG with (a-b) low magnification and (c-d) high magnification. (d) is a magnified image of yellow circled region in (c).

(e) EDS analysis images of MWpSi-EG with the element mapping of silicon, oxygen, carbon and nitrogen..

.....93

Figure 2.10. HR-TEM image of HTpSi-EG.....93

Figure 2.11. HR-TEM image of HTpSi-EG & bare silicon nanoparticle with a native oxide layer.....93

Figure 2.12. (a) EDS analysis images of MWpSi-EG with the element mapping of silicon, oxygen, carbon and nitrogen. (b) The EDS line scan region and the direction. (c) The EDS line scan profiles for silicon, oxygen and carbon.....94

Figure 2.13. Raman spectra of (a) Si-EG, HTSi-EG, MWSi-EG,

(b) pSi-EG, HTpSi-EG and MWpSi-EG. (c) XRD patterns of pSi-EG, HTSi-EG and MWpSi-EG.....99

Figure 2.14. TGA data of Si, pSi, MWSi-EG and MWpSi-EG99

Figure 2.15. C1s XPS spectra of (a) EG, (b) pSi-EG, (c) HTpSi-EG and (d) MWpSi-EG. N1s XPS spectra of (e) HTpSi-EG and (f) MWpSi-EG.....100

Figure 2.16. Galvanostatic charge/discharge profiles of (a) Si-EG, (b) pSi-EG, (c) MWSi-EG and (d) MWpSi-EG. The initial cycle for each sample is at 0.1 A g^{-1} . The subsequent cycles are at 0.4 A g^{-1} 107

Figure 2.17. Cyclic voltammogram of (a) MWSi-EG and (b)

MWpSi-EG for first 5 cycles with a scan rate of 10 mV s⁻¹ in a voltage window between 0.01 - 2.0 V (vs. Li/Li⁺). (c) rate performance of MWSi-EG and MWpSi-EG with various current densities. (d) Cycling performance of MWSi-EG and MWpSi-EG for 50 cycles. (e) long-term cycling performance of MWpSi-EG with a current density of 1.0 A g⁻¹ except the initial cycle.....10

8

Figure 2.18. Rate performance of Si-EG and pSi-EG at various current densities.....109

Figure 2.19. (a) rate performance of MWpSi-EG and HTPSi-EG at various current densities. (b) Nyquist plot of MWpSi-EG, MWSi-EG, HTPSi-EG, pSi-EG and Si-EG.....109

Figure 2.20. SEM images of MWpSi-EG after 120 cycles at 1.0 A g⁻¹ with (a) low and (b) high magnification.....110

Figure 3.1. Schematic illustration of a home-made Jig setup for electrochemical unzipping of MWCNT.....122

Figure 3.2. (a) Photograph of the three-electrode cell used to perform the electrochemical reaction in concentrated sulfuric acid. (b) Hydrogen evolution (dashed-line box) was observed on the Pt ring (counter electrode) during galvanostatic charging at a current density of 0.5 mA cm⁻². (c) Photograph showing the MWCNTs after the unzipping process.....124

Figure 3.3. (a) Schematic representation of electrochemical process for unzipping MWCNT, (b) Schematic illustration of a designed cell for electrochemical

unzipping of MWCNT and Photograph of the three-electrode cell used to perform the electrochemical reaction (inset: Photograph showing the MWCNTs after the unzipping process), and (c) GNR-2.5H dispersion in ethanol (0.5 mg mL^{-1}) obtained by galvanostatic charging and washing processes for 2.5 hours. ... 133

Figure 3.4. Electrochemical measurements of MWCNT in 18 M H_2SO_4 electrolyte. (a) Galvanostatic charge curve at various charging current densities (0.5 , 1.0 , and 2.0 mA cm^{-2}), (b) Time potential versus plotted Coulomb/mass loading during the electrochemical reaction, (c) SEM images of the related byproducts (current density: 1.0 and 2.0 mA cm^{-2}), (d) Galvanostatic charging curve of MWCNT with a current density of 0.2 mA mg^{-1} in 18 M H_2SO_4 electrolyte at different mass loading, (e) SEM images obtained after electrochemical reaction for 2.5 hours, and (f) Milligram-scale synthesis of GNR-2.5H was

done in the laboratory.	134
Figure 3.5. Morphology characterization of GNRs at various potential: SEM and TEM images of a, e) pristine MWCNT, b, f) GNR-2.5H, c, g) GNR-4H and d, h) GNR-7H, respectively.. .	137
Figure 3.6. Material characterizations of the unzipped MWCNT. (denote as unzipped MWCNT- <i>i</i>) (a) and (b) TEM images, (c) XRD patterns, (d) and (e) SEM images, and (f) TGA curves. The weight loss of unzipped MWCNT- <i>i</i> observed at 800 °C is approximately 9.7 wt%..	138
Figure 3.7. (a) Galvanostatic charge curve at current density of 0.5 mA cm ⁻² . (b) TEM images of pristine S-MWCNT, (c) surface oxidation of S-MWNCT performed in 0.5 M H ₂ SO ₄ electrolyte, and (d) partially unzipped GNR performed in 18 M H ₂ SO ₄ electrolyte.. .	140
Figure 3.8. SEM image of (a) pristine M-MWCNTs. (b) and (c) SEM and TEM images of the partially unzipped GNR.	

The electrochemical charge reaction was performed in 18 M H₂SO₄ electrolyte at a current density of 0.5 mA cm⁻² for 2.5 hours.141

Figure 3.9. Physical and chemical characteristics of unzipped MWCNT products obtained at various potential: a) XRD patterns, b) Raman spectra, c) TGA curves for the decomposition of the products, and d) XPS spectra normalized to C1s intensity.....145

Figure 3.10. (a) High resolution XPS for C1s spectra of the as-prepared products and TGA thermogram of (b) concentrated sulfuric acid products. The thermogram of the products is obtained with a ramping rate of 10 °C min⁻¹ in air.....146

Figure 3.11. a) Galvanostatic charging curve of MWCNT working electrode with a platinum counter electrode and Hg/Hg₂SO₄ reference electrode, in 18 M H₂SO₄ electrolyte, recorded at current density of 0.5 mA cm⁻² at 25 °C. b) Cell potential (V) and derivative dV/dQ

plotted versus Time (h) and Coulomb (Q). c) Raman spectra and d) XRD patterns of sulfuric acid intercalated MWCNT formed at different voltage states (The broad background in XRD is due to the glass sample holder.148

Figure 3.12. Galvanostatic charge (GC) curves for concentrations varying from 0.5 M to 18 M H₂SO₄ electrolytes.149

Figure 3.13. Ex-situ Optical microscope of MWCNTs with different charging states in concentrated H₂SO₄ electrolyte. The photographs of pristine MWCNT, charge states *i* (0.5 h), a (2.5 h), and b (4 h) shows grayish-blue, dark-navy, reddish-brown, and darkish-brown colors, respectively.151

Figure 3.14. a) Galvanostatic charging curves of MWCNT working electrode with a platinum counter electrode and Hg/Hg₂SO₄ reference electrode at different H₂SO₄ concentrations at a current density of 0.5 mA cm⁻² for 7 hours and b-e) Related SEM images of the

byproducts result in the electrochemical reactions.....	154
Figure 3.15. Characterization of products obtained by electrochemical reactions at different concentrations of H ₂ SO ₄ . (a) X-ray diffraction analysis, (b) Raman spectra, and (c) FT-IR spectroscopy.	158
Figure 3.16. TEM images of the as-prepared products without caps; (a) 0.5 M Ox-MWNCT-7H, (b) 10 M Ox-MWNCT-7H, and (c) 15 M GNR-7H.....	159
Figure 3.17. TEM images of the as-prepared products caps; (a) MWCNT, (b) 0.5 M Ox-MWNCT-7H, (c) 10 M Ox-MWNCT-7H, and (d) 15 M GNR-7H....	159
Figure 3.18. The thermogram of the products is obtained by the different concentration of sulfuric acid with a ramping rate of 10 °C min ⁻¹ in N ₂ and Air atmosphere; (a) N ₂ and (b) Air....	160
Figure 3.19. Characterization on morphology of (a-c) GNR (denoted as a GNR-7H) in 18 M H ₂ SO ₄ and (e-g) oxidized MWCNT reacted in 0.5 M H ₂ SO ₄ : a) and	

e) TEM, b) and f) High resolution TEM (HR-TEM) images of corresponding the blue dashed square in a) and e), c) and g)161

Figure 3.20. Aberration-corrected scanning transmission electron microscope (STEM) and a) and c) Electron energy-loss spectroscopy (EELS) spectra obtained from the selected points 1 and 2 in b) and d) respectively.....163

Figure 3.21. Brunauer–Emmett–Teller (BET) surface areas of MWCNT and GNR-2.5H.164

Figure 3.22. (a-f) Electrochemical measurements of the alkali-ion capacitor: (a-c) Li-ion capacitor and (d-f) K-ion capacitor. a, b) Charge/discharge curves of MWCNT and GNR-2.5H for first three cycles and c) Rate performance of MWCNT and GNR-2.5H at various current densities. (d-f) Electrochemical double-layer capacitance (EDLC) performances of MWCNT and GNR-2.5H in a three-electrode system: d) Cyclic voltammetry (CV) curves at scan rate of 50 mV s^{-1} , e)

CV curves of GNR-2.5H measured at various scan rates, and f) Specific capacitance at different current densities.....1

67

Figure 3.23. SEM images of the electrochemically exfoliated graphene (EEG); (a) Low and (b) High magnification....171

Figure 3.24. SEM images of (a) MoS₂, (b) MoS₂/EEG, (c) MoS₂/MWCNT, and (d) MoS₂/GNR-2.5H.....171

Figure 3.25. Electrochemical characterization of the as-prepared catalysts; (a) HER LSV curves at a scan rate of 2 mV s⁻¹ in 0.5 m H₂SO₄ (Inset: long term stability test of the MoS₂/GNR-2.5H), (b) The corresponding Tafel plots of the catalysts. (c) Determined double layered capacitances (C_{dl}) performed by CV measurements, and (d) The electrochemical impedance spectroscopy (EIS) of the MoS₂/GNR-2.5H, MoS₂/MWCNT and

MoS₂/EEG.172

Figure 3.26. LSV curves at a scan rate of 2 mV s⁻¹ in 0.5 M H₂SO₄;

(a) bare MoS₂ and MoS₂/GNR-2.5H according to the weigh ratio of the precursor (Ammonium tetrathiomolybdate, ATTM) and (b) the MoS₂/GNR-2.5H (1:2) at different mass loading.173

Figure 3.27. Cyclic voltammograms (CV) of (a) MoS₂/GNR-2.5H,

(b) MoS₂/MWCNT, and (c) MoS₂/EEG recorded at scan rates of 20 to 80 mV s⁻¹.173

List of Tables

Table 1.1.	Prices of carbon materials for energy storage/conversion applications.....	44
Table 1.2.	Comparison of electrochemical exfoliation methods for preparing the few layered graphene.....	62
Table 1.3.	Comparison of electrochemical unzipping methods for unzipping the multi-walled carbon nanotube.....	64
Table 2.1.	Physical properties of MWSi-EG and MWpSi-EG....	110
Table 3.1.	The concentration of Fe element determined by ICP-MS measurement.....	136
Table 3.2.	The full width at half maximum (FWHM) of the pristine MWNCT and all products was evaluated from the width of (002) peak using MDI Jade 6	

software for multiple Gaussian function. A wider value of FWHM (B_{size} , °) indicates that the oxidation of MWCNT decreased the degree of crystallinity.....144

Table 3.3. Detailed oxidation levels of the products in different electrolyte concentrations analyzed by XPS and TGA curves.....1
60

Table 3.4. The sheet resistance of the samples was investigated by a four-point probe measurement. This shows that the level of oxidation affects the conductivity of products.....1
65

Chapter 1. Introduction

1.1. Graphene and graphene nanoribbon

Graphene is a two-dimensional planar sheet of sp^2 -bonded carbon atoms, and one of the most researched nanomaterials in the 21st century. In contrast to fullerene [1], carbon nanotubes [2], and other allotropes of carbon, graphene is a perfect two-dimensional material (**Figure 1.1**).

In 2004, graphene was discovered by Geim and Novoselov at the University of Manchester [3]. Previously, it was believed that this

material was thermodynamically unstable and therefore could not exist in the real world [4]. The discovery of graphene in 2004 has intrigued many researchers in scientific communities as it exhibits several unique properties that are not found in conventional three-dimensional materials. For example, perfect graphene has high electron mobility ($15,000 \text{ cm}^2\text{V}^{-1}\text{s}^{-1}$) [3], large theoretical specific surface area ($2630 \text{ m}^2 \text{ g}^{-1}$) [6], high thermal conductivity ($\sim 4.84 \pm 0.44 \times 10^3$ to $5.30 \pm 0.48 \times 10^3 \text{ W/mK}$ at room temperature)[7], and excellent mechanical properties (Young's modulus of $\sim 1.0 \text{ TPa}$) [8].

Graphene is a building block for graphitic materials (sp²) with various dimensionalities such as fullerene (0D), carbon nanotubes (1D), and graphite (3D) [9]. Graphene can also be a building block for various types of nanostructured graphene derivatives [10]. As illustrated in **Figure 1.2**, cutting graphene in small pieces yields graphene quantum dots (GQDs); slicing graphene yields graphene nanoribbons (GNRs), and making holes on the basal planes of graphene yields porous or holey graphene (hG).

Tailoring such a sheet-like morphology to this nanostructure leads to novel properties, such as edge effects and electron quantum confinements, while maintaining the intrinsic properties of graphene. For example, GNRs are narrow strips of graphene with a width of less than 100 nm. Their electrical properties dependent on the width, edge structure, and crystallographic symmetry [11]. GNRs with zigzag edge structures possess intrinsically metallic properties, whereas armchair GNRs that are <10 nm wide possess semiconducting properties.

Graphene and GNRs with excellent physicochemical properties have been explored in a wide range of applications such as touch screens [12], field-effect transistors [13], transparent conductors [14], and organic light-emitting diodes [15]. In particular, graphene and GNR with excellent electrical conductivity, chemical stability, and high surface area have been explored as the active materials or conductive additives for energy conversion/storage devices such as fuel cells, supercapacitors, and lithium-ion batteries (LIBs).

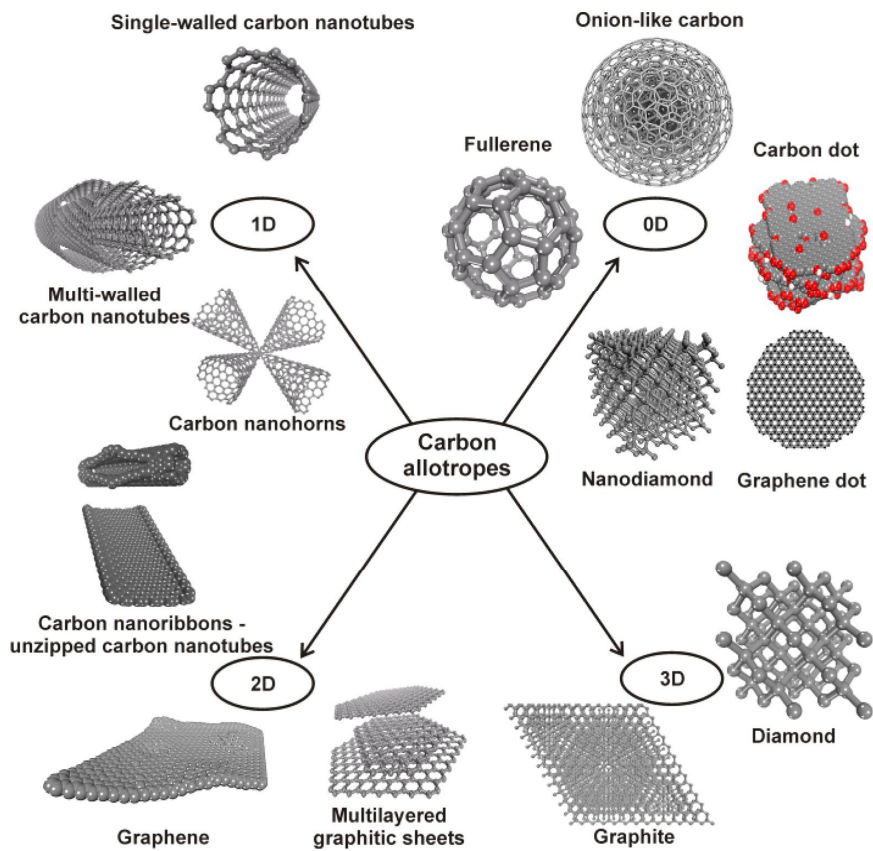


Figure 1.1. Classification of carbon allotropes. (from Ref. [4])

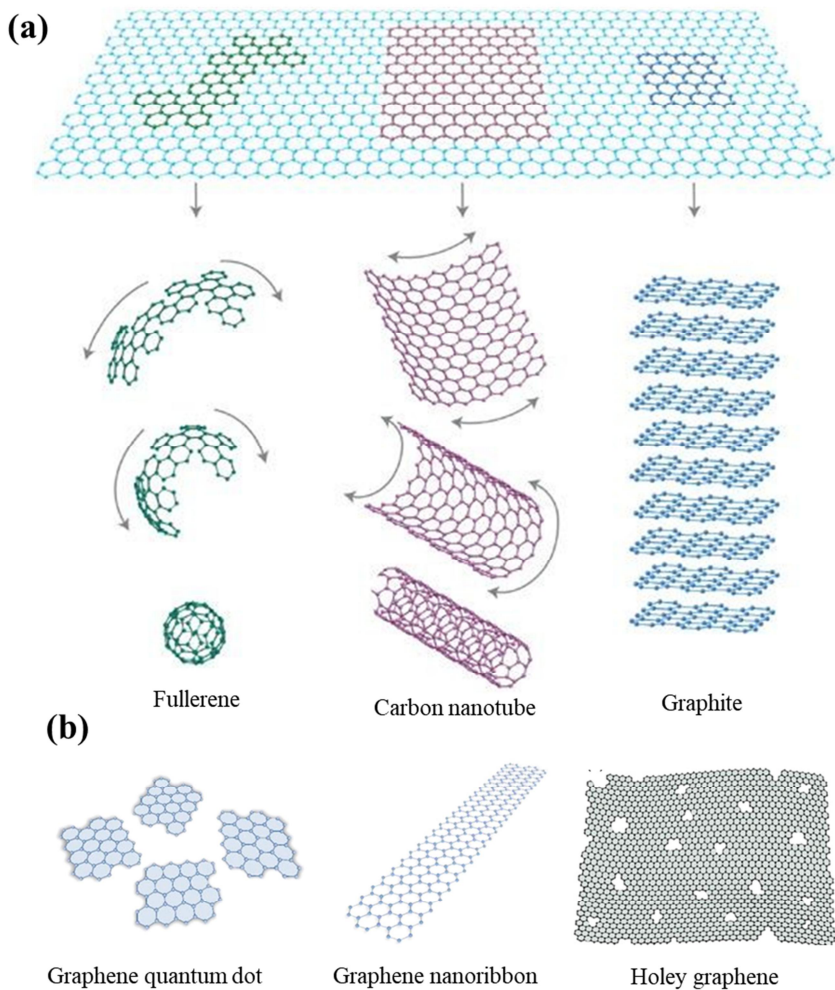


Figure 1.2 (a) Graphene can be wrapped up into 0D fullerenes, rolled into 1D nanotubes, stacked into 3D graphite, (b) cut into graphene quantum dots, sliced into nanoribbons or drilled to form holey graphene. (from Refs. [9] and [10].)

1.2. Application of graphene and graphene nanoribbons for energy storage and conversion devices

With the increase in global energy consumption, developing efficient energy storage and conversion technologies has become one of the biggest challenges for science and technology communities [16]. The remarkable properties of graphene and GNRs have the potential to revolutionize a number of technologically important areas, particularly energy storage/conversion applications [17]. Both materials have been proposed for use in several types of electrochemical energy storage/conversion devices, either as active materials [18-20] or as inactive components [21-23]. In the following section, I will briefly introduce energy storage/conversion applications such as LIBs, supercapacitors, and water electrolysis and discuss the use of both materials in these applications.

1.2.1. Active material

Graphene and GNR can be used as active materials for energy storage devices. Both materials can store charges through intercalation, electrical ion adsorption, or Faradaic reactions.

Lithium ion battery

LIBs have become the most important power source for a wide range of applications, owing to their high voltage, high coulombic efficiency, high energy density, long cycling life, and light weight [24]. LIBs consist of four main components: anode, cathode, and electrolyte, and separator (**Figure 1.3**). During charging, the lithium ions are de-intercalated from the cathode and introduced into the anode, and the reverse occurs during the discharging process [25].

Lithium-containing metal oxides such as lithium cobalt oxide and lithium iron phosphate are used as cathode materials. Graphite is

used as an anode material for commercial LIBs. However, graphite exhibits low Li storage capacity (*i.e.*, less than 372 mA h g⁻¹), because of its limited lithium ion storage (LiC₆) [26].

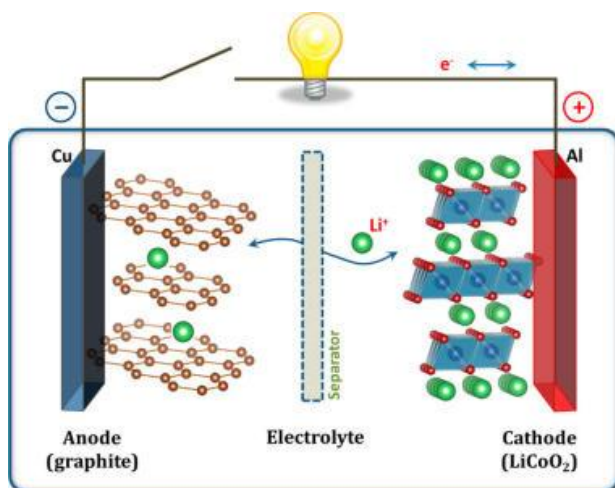


Figure 1.3. Schematic illustration of the first LIBs (LiCoO₂/Li⁺ electrolyte/graphite). (from Ref. [25])

Replacing graphite anodes with graphene can significantly improve lithium storage characteristics. Graphene exhibits high reversible capacities (794–1054 mA h/g) [27] because graphene sheets can store additional lithium ions on their internal surface and defects. Although graphene exhibits high capacities, several challenges such as high irreversible capacity loss during the first

lithiation step, low initial coulombic efficiency, and restacking issues during repeated cycling limit its practical use in LIBs.

Theoretical research suggests that the use of a GNR as the anode material enhances the adsorption and diffusion of lithium ions on the GNR surface is enhanced compared to planar graphene sheets [28]. Another benefit of GNRs is that the diffusion length of lithium ions is reduced owing to its quasi-one-dimensional morphology, which increases the rate capability. However, high irreversible capacity loss during the first lithiation step and unstable formation of the solid electrolyte interphase layer remain as an issue for both graphene and GNRs in LIB applications [29].

Supercapacitors

Supercapacitors, also known as electrochemical capacitors, are energy storage devices that can offer higher power density than other secondary batteries and higher energy density than electrical capacitors [30]. The charge storage mechanism of supercapacitors

can be typically classified into two types: electrical double-layer capacitors (EDLCs), and pseudocapacitors. In EDLCs, the capacitance arises from the physical accumulation of charges or the formation of an electrical double layer at the electrode/electrolyte interface (**Figure 1.4**). To accumulate more charges, the active materials in EDLC devices should be electrochemically stable and present a high surface area.

Thus, as graphene has high theoretical surface area ($2,675 \text{ m}^2 \text{ g}^{-1}$) and excellent electrochemical stability, it is an ideal active material for EDLC electrodes. When the entire surface of graphene is fully utilized, its theoretical specific capacitance can reach up to 550 F g^{-1} [31]. However, it is difficult to reach this capacitance in real situations because graphene sheets restack during the electrode manufacturing and electrochemical cycling processes. The use of GNRs may alleviate the restacking issue, but it is necessary to develop a strategy to fabricate a high packing density electrode without restacking of graphene sheets [32].

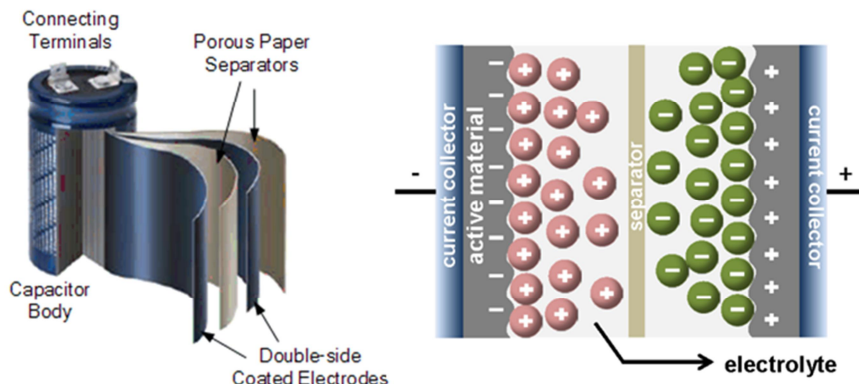


Figure 1.4. Schematic illustration of an electric double-layer capacitor (EDLC) (Left image source : <https://www.ultracapacitor.co.kr>)

1.2.2 Inactive material

Graphene can contribute in electrochemical energy storage/conversion devices without being involved in the reaction due to its impressive electrical conductivity, high surface area, and excellent mechanical properties. It can function as an efficient electron transport channel, stress-buffering material for active

materials that suffer from volume change during charging, and heat conductor to discharge the heat generated during high current loads or/and abusive conditions [33]. As a result, using graphene as an inactive component in electrochemical energy storage/conversion devices significantly improves the device performance in terms of capacity, rate capability, thermal stability, or overpotential.

As an inactive component in electrochemical energy storage/conversion devices, GNRs exhibit additional advantages over graphene sheets owing to their quasi-one-dimensional morphology [34]. When graphene is used in the electrode, the layered morphology generates tortuous pathways for ion migration, resulting in decreased ion mobility. This phenomenon becomes more apparent with thicker and denser electrodes. Compared to graphene, the high aspect ratio of GNRs significantly lowers the percolation threshold to form an electrically conducting network and generate less tortuous pathways for efficient ion migration [35].

Lithium ion battery

Tin, silicon and several transition metal-based compounds can reversibly react with lithium with high theoretical capacities [36]. However, the practical application of silicon and most transition metal-based compounds is hindered by some challenges: low electrical conductivity, poor cycle stability due to large volume expansion and instability of the solid electrolyte interface during cycling.

A general strategy has been demonstrated to achieve improved electrochemical performance by constructing nanocomposites based on the combination of nanoparticles and graphene nanosheets. In this way, graphene can buffer the volume changes of the active materials and improve the electrical conductivity. In addition, nanoparticles can prevent restacking of graphene. However, similar to graphene as an active material in LIBs, graphene-based nanocomposites suffer from high irreversible

capacity loss during the first cycle owing to the instability of the formed solid electrolyte interface during the electrochemical reactions [37].

Supercapacitor

The electrode material of the supercapacitor can be classified as EDLC or pseudocapacitor. Pseudocapacitive materials usually show higher capacitance than EDLC materials. In pseudocapacitive materials, the charge is stored by fast and reversible Faradaic processes at the electrode/electrolyte interface of the active material. Oxygen-containing functional groups in graphene, conducting polymers, or transition metal oxides have been investigated as active materials for pseudocapacitor electrodes [31].

The introduction of graphene or GNRs can improve the electrochemical performance of pseudocapacitive materials. To realize the full potential of graphene and GNRs in

pseudocapacitors, the development of nanocomposites with optimized structure (e.g., hierarchical structure) is needed [38].

Catalyst for electrochemical reactions (hydrogen evolution reaction)

Currently, a common method for producing commercial hydrogen is the steam methane reforming process, which emits carbon dioxide as a byproduct. Electrochemical water splitting is a promising method for producing carbon dioxide-free hydrogen, particularly when the electricity generated from renewable sources is used to drive the electrochemical reaction [39]. However, the current electrochemical water splitting process is far from the commercialization stage because of the following issues : (1) large overpotential of the water splitting reactions including hydrogen evolution reaction (HER) and oxygen evolution reaction (OER), and (2) high cost of Pt-based electrocatalysts in the water-splitting cell. In a material prospective, there are two strategies to

overcome the challenges [40]: minimize the Pt loading in the electrode [23], or replace the Pt with low cost and earth-abundant electrocatalysts (e.g., transition metal oxides, metal phosphides, dichalcogenides, nitrides, carbides [41]).

As a catalyst support for electrochemical reactions, graphene delivers multiple functions and has many benefits. In particular, graphene provides a large surface area for dispersing active materials, high electrical conductivity to promote charge transfer for electrochemical reactions, and excellent chemical stability to maintain the structure during severe electrocatalytic reactions. During electrochemical reactions, graphene improves the HER kinetics by generating strong synergetic coupling effects.

Similar to other applications, designing the nanostructures is critical for improving HER performance. GNRs with a high aspect ratio may be used to prepare unusual nanostructured catalysts with high performances [42].

1.3. Synthesis strategies for graphene and graphene nanoribbon

Over the past few years, many studies have explored graphene-based materials for electrochemical energy applications. The use of graphene or GNRs in energy storage devices leads to devices with longer life, faster charging, and higher energy density. In energy conversion applications, the use of graphene or GNRs significantly enhances the catalytic activity of the supported catalysts.

Although current research progress indicates future commercialization, the high cost of graphene and GNRs, caused by the lack of efficient production protocols, limits their practical usage in energy storage/conversion applications [43]. For example, the cost of activated carbon, graphite, and carbon black currently used in energy storage/conversion devices is considerably lower than that of graphene. (**Table 1.1**) The method for graphene or GNRs synthesis should be able to provide the required quantities and cost while ensuring reliable quality for the energy

storage/conversion applications.

1.3.1. Preparation of graphene

Graphene properties depend on the production method, which can be divided into two main categories: (i) top-down and (ii) bottom-up methods. (**Figure 1.5**) Graphene was first prepared by mechanical exfoliation (known as “Scotch tape” method) of highly oriented pyrolytic graphite (HOPG) [3]. The method yielded high-quality graphene which enabled the study of its fundamental properties.

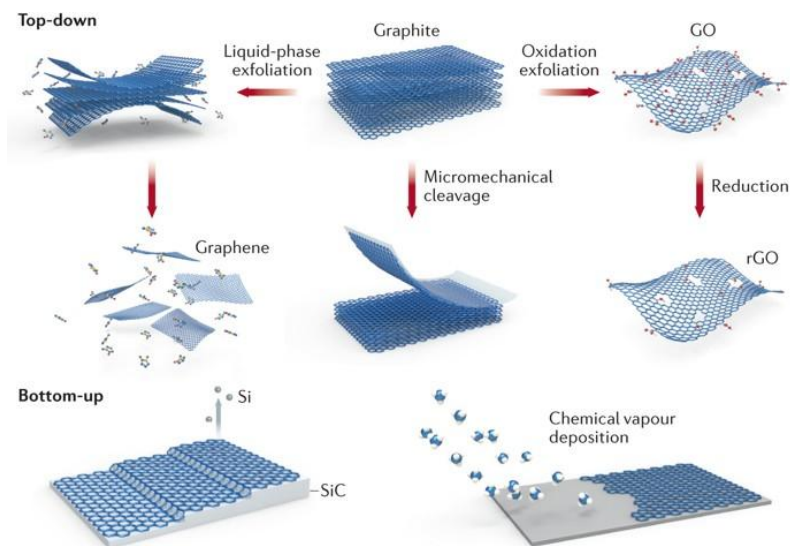


Figure 1.5. Major graphene fabrication methods (from Ref. [44]).

Table 1.1 Prices of carbon materials for energy storage/conversion applications.

Material	Cost (Sigma Aldrich)
Activated carbon	0.12 \$ g ⁻¹
Carbon black (graphitized)	32 \$ g ⁻¹
Graphite	0.07 \$ g ⁻¹
Graphene nanoplatelet	758 \$ g ⁻¹
Reduced graphene oxide	726 \$ g ⁻¹
Graphene nanoribbon	602 \$ g ⁻¹

In general, graphene prepared by bottom-up methods (*e.g.*, chemical vapor deposition method and epitaxial growth on crystalline SiC) provides structurally intact and large-area graphene films for fundamental research and electrical applications. (*e.g.*, touch screens and high-frequency transistors). However, these methods are unsuitable for the mass production of graphene for energy applications because of their high production costs [33, 43].

Top-down methods such as liquid-phase exfoliation and chemical oxidation are the well-known for the bulk production of graphene. Unlike bottom-up methods, top-down methods produce graphene of arbitrary shapes and lateral dimensions in the order of hundreds of nanometers up to tens of micrometers [43].

Graphene produced by direct liquid exfoliation is often called graphene nanoplatelets (GNPs) rather than graphene because GNPs are a mixture of single-layer, few layers, and nanostructured unexfoliated graphite [45]. In the liquid exfoliation method, graphite or expanded graphite are dispersed in a solvent

with a surface energy close to that of graphene or a surfactant solution (**Figure 1.6**). Then, the mixture is subjected to sonication, shear mixing or ball milling. The liquid exfoliation method has the advantage of a simple procedure; however, it has the drawbacks of low yield, use of organic solvents or surfactants, and the tendency of restacking of graphene layers during the subsequent solvent removal process.

Pristine graphene is prone to restacking due to van der Waals forces between the basal planes of graphene layers. One effective way to prevent this is by attaching functional groups to the graphene surface. Chemical oxidation is a well-known functionalization method. When graphite or graphitic materials are subjected to chemical oxidation, oxygen-containing functional groups are attached to the basal planes and edges of each graphene layer in graphite forming “graphite oxide”. The graphite oxide produced by chemical oxidation method can be further liquid exfoliated to form single-layered graphene oxide (GO). GO is then reduced to form reduced graphene oxide (rGO) (**Figure 1.7**) [46]. Although GO inevitably restacks during the reduction

process, this approach is particularly useful for energy-storage materials because GO can be used as a reagent or further modified with organic or inorganic materials to prepare nanocomposites [33]. Additionally, GO can be easily dispersed in a wide range of solvents, including water and other volatile solvents.

The chemical oxide method offers scalable routes for the prepare GO in high yield. Nonetheless, there are also disadvantages with chemical oxidation method [47]. First, the chemical oxidation process takes a few hours to several days. More severely, the method involves the generation of various toxic gases (NO_2 , N_2O_4 , and ClO_2) and explosive intermediates (e.g., manganese heptoxide). Furthermore, the purification steps required to remove manganese metal ions and residual acids produce a large amount of wastewater.

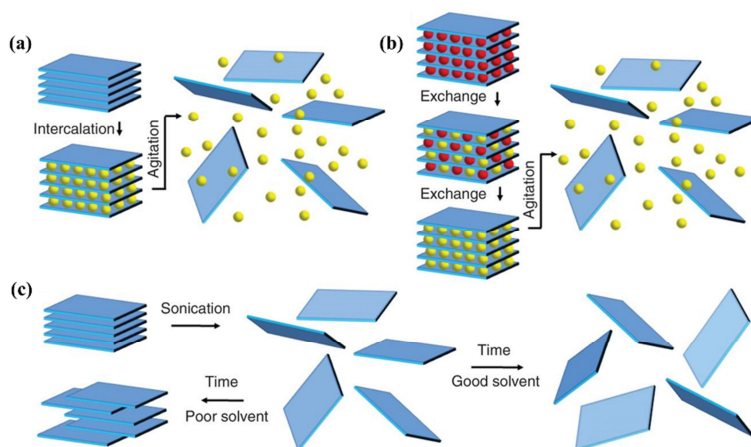


Figure 1.6. Schematic representation of liquid exfoliation process: a) intercalation, b) ion exchange and c) ultrasonic exfoliation. (from Ref. [45])

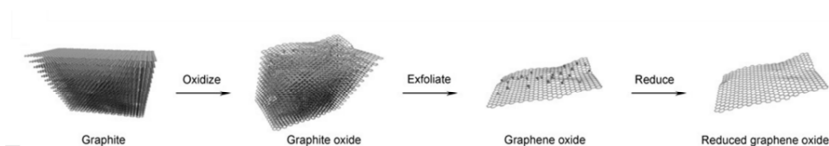


Figure 1.7. Preparation of reduced graphene oxide from graphite. (from Ref. [46])

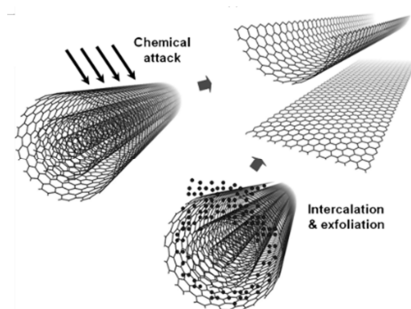
1.3.2. Preparation of Graphene nanoribbons

The synthesis of GNRs can be classified as top-down and bottom-up methods [48]. Bottom-up methods are preferred for the preparation of GNRs for electrical applications because the method can accurately control the GNR structure on the atomic scale [49]. For energy-related applications, top-down methods are more suitable in terms of scalability and production cost.

Unzipping carbon nanotubes (CNTs) are one of the most well-developed top-down methods for obtaining GNRs [50]. MWCNTs unzipping methods can be classified into three major types: reductive unzipping [51], oxidative unzipping [50], and other unzipping methods with unclear driving forces. For reductive and oxidative unzipping methods, intercalation is the driving force for unzipping; lithium and potassium metals are used as intercalants for reductive unzipping, and sulfuric acid is used as an intercalant for oxidative unzipping [52]. As the reductive unzipping method uses alkali metals, unzipping must be processed in an inert atmosphere. The oxidative unzipping process can be carried out in the ambient atmosphere, but the method has environmental and safety issues due to the use of hazardous and

explosive chemicals.

Figure 1.8. Various MWCNT unzipping methods. (from Ref. [48])



1.4. Electrochemical method

As detailed in section 1.3, current chemical methods for preparing graphene (or GNRs) are typically conducted at elevated temperatures and rely on the use of toxic, and explosive chemical reagents. In this regard, electrochemical exfoliation methods have recently been recognized as a sustainable and scalable strategy for the preparation of graphene [53] and other two-dimensional materials [54-56]. In contrast to current chemical methods, electrochemical exfoliation usually takes several minutes to hours, producing two-dimensional materials with gram-scale quantities

at the laboratory level. Furthermore, the electrochemical exfoliation method is simple, and the entire synthetic process can be performed under ambient conditions.

The electrochemical exfoliation process was performed using an electrochemical cell (**Figure 1.9**). Generally, a two-electrode setup consisting of a working electrode, counter electrode, liquid electrolyte is employed for the processes [57]. The working electrode, in the shape of rod, foil, flake, or plate, serves as either an anode or cathode for the exfoliation. For the counter electrode, a Pt wire or coil is typically used.

Once a suitable voltage is applied between the working and counter electrodes, ionic species are inserted into the interlayers. Then, the inserted intercalants decompose and expand the layered material, leading to exfoliation. The electrochemical exfoliation method can be classified into two approaches based on the applied potential: anodic and cathodic exfoliations (**Figure 1.9**).

Cathodic exfoliation

The application of a negative potential to the layered material drives the co-intercalation of cations and solvent molecules which would expand and exfoliate the layered material. Cationic species such as lithium ions [58], quaternary ammonium ions [59], and ionic liquid solutions [60] have been proposed for cathodic exfoliation of layered materials. Nevertheless, the aqueous electrolyte cannot be used for the cathodic exfoliation because hydrated cations are less likely to be intercalated into the layered materials [61].

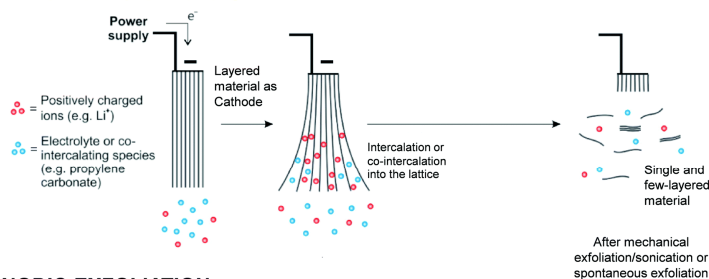
Because the reduction reactions mainly contribute to the expansion of interlayer spacing, cathodic exfoliation facilitates the isolation of large-size and highly crystalline 2D materials. However, this approach is less efficient and slow compared to anodic exfoliation. Moreover, the exfoliated materials are mainly few-layered [62].

Anodic exfoliation

Anodic exfoliation is performed by applying a positive voltage to the layered material. Conversely, the application of a positive voltage drives the co-intercalation of anions and solvent present in solution. Sulfate is the most efficient anion intercalant for the anodic exfoliation process [63]; however, other anions such as sulfonate [64], nitrate [65], perchloride [66], hydroxyl [67], carboxylate [68], and phosphate [69] have also been proposed.

For anodic exfoliation methods, naturally abundant water can be used as the solvent, and the entire process can be performed in an ambient atmosphere. Moreover, this method has an efficient and fast process. However, the exfoliated 2D sheets obtained by anodic exfoliation methods or are often rich in structural defects or functionalized with oxygen-containing organic groups [70].

CATHODIC EXFOLIATION



ANODIC EXFOLIATION

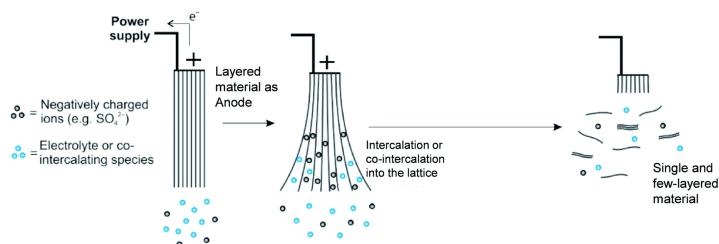


Figure 1.9 Schematic overview of cathodic and anodic exfoliation.
(from Ref. [57])

1.4.1 Electrochemical exfoliation of graphite

Intercalation-functionalization

Similar to the chemical oxidation method, intercalation is the first step in the electrochemical exfoliation process. Intercalation weakens the attractive forces between the adjacent layers of

graphite and provides a reaction pathway for the functionalization process [71]. However, intercalation itself is not sufficient to separate the graphitic layers because graphite returns to its initial phase upon deintercalation.

Electrochemical methods have been used for the synthesis of graphite intercalation compounds. When certain atomic or molecular species are inserted between the graphene layers of graphite, graphite intercalation compounds (GIC) are formed. The stage index, n , is defined as the number of graphene layers between two adjacent intercalant layers and the corresponding material is called a stage- n -GIC [72]. The electrochemical intercalation of graphite occurs at both the anode and the cathode.

The electrochemical intercalation of graphite can be dated back to the early 1980s, when stage-1-GIC bisulfate and graphite oxide were prepared by anodic oxidation of graphite in concentrated sulfuric acid (H_2SO_4) [63, 73-75]. The intercalation of sulfuric acid into the graphitic carbon depends on the concentration of the electrolyte. When the water concentration in the sulfuric acid

becomes too high (less than 15 M), the intercalation reaction is disturbed by the water decomposition (formation of high-stage GIC). Fundamentally, the anodic oxidation of graphite in H_2SO_4 or perchloric acid (HClO_4) involves three distinct steps that resemble the process of chemical oxidation: 1) formation of stage-1-GIC, 2) functionalization and 3) hydrolysis of functionalized graphene layers [76, 77] (**Figure 1.10**). The last step is also known as the “hidden second oxidation step” because graphitic domains are significantly decreased, and oxygen functional groups are significantly increased after this process [78]. The major differences between chemical and anodic oxidation methods are as follows: in the chemical oxidation method, chemical reagents homogeneously oxidize the material; in the anodic oxidation method, strong oxidative radicals (hydroxyl radical or atomic oxygen) heterogeneously oxidize the electrode [79].

Lowe et al. [80] demonstrated the synthesis of GO by the electrochemical intercalation-functionalization method. Their choice of electrolyte was 11.6 M sulfuric acid. Although the

concentration did not satisfy the criteria for intercalation (formation of stage III–IV GIC), the method met the criteria for the following functionalization step. In their method, the lowest C/O (atomic ratio) for GO was 4.07, which is a significant step towards the bulk functionalization of the graphene layer as shown in the traditional chemical oxidation method. Kinloch et al. [81], and Ren et al. [82], successively reported the synthesis of GO by separating the intercalation and functionalization steps. The graphite foil was anodically oxidized in concentrated H_2SO_4 to form the stage-1-GIC. The second functionalization step was separately held by anodically oxidizing stage-1-GIC graphite foil in 0.1M $(\text{NH}_4)_2\text{SO}_4$ aqueous solution or in 5M H_2SO_4 . By separating the intercalation and functionalization steps, stage-1-GIC was properly formed and the graphite lattice was fully oxidized within a few seconds. The obtained GO was similar to those obtained by the chemical oxidation methods. Swager et al.[83], prepared functionalized graphene using a cathodic reduction approach (**Figure 1.10**). First, “hyperstage GIC” was prepared by cathodic intercalation with tetrabutylammonium ions

(TBA⁺). The hyperstage GIC displayed a highly expanded graphite lattice with d-spacing over 15.3 Å. Then, the hyperstage GIC was reacted and functionalized with diazonium ions. As soon as the functionalization occurred, the modified hyperstage GIC underwent spontaneous exfoliation.

Partial intercalation and functionalization

Complete formation of GIC is a prerequisite for the preparation of single-or few- layered functionalization of graphene by either chemical process or electrochemical process. However, the methodology based on the exfoliation of graphite in an aqueous electrolyte which forms a high- stage GIC during the synthesis, is widely used for the electrochemical exfoliation of graphite.

Electrochemical exfoliation of graphite in diluted aqueous electrolytes is regarded as a highly scalable, eco-friendly method for the preparation of few-layered graphene with a low oxidation

degree [84]. Generally, the anodic exfoliation of graphite in an aqueous sulfate electrolyte involves the following steps: 1) generated oxygen ($\text{O}\cdot$) and hydroxyl ($\text{HO}\cdot$) radicals attack the defective sites or edges of the graphite, and expand its outer edges of graphite. 2) The outer edges of graphite further expand, facilitating the intercalation of hydrated sulfate anions to form high stage GIC [85]. 3) The intercalated hydrated sulfate anions decompose to gases (e.g., O_2 , SO_2 , and CO_x) and further expand the graphite (**Figure 1.12**).

Different types of salts have been used for electrochemical exfoliation (e.g., 0.1 M H_2SO_4 , 0.1 M $(\text{NH}_4)_2\text{SO}_4$, **Table 1.2**). For example, when 0.1 M $(\text{NH}_4)_2\text{SO}_4$ was employed for the electrochemical exfoliation process, graphene flakes with less than three layers ($\sim 85\%$) and a high C/O ratio of 17.2 were obtained [86]. However, the yield of single-layer graphene was low, and the exfoliated graphene was only dispersible in high-boiling-point solvents. Recently, Liu et al. showed that a mixture of alkaline electrolyte and aqueous sulfate solutions (0.1 M $\text{NaOH}/\text{Na}_2\text{SO}_4$) is very efficient for producing water□

dispersible and bilayer-rich graphene.

1.4.2. Electrochemical unzipping of multiwalled carbon nanotubes

Compared to the electrochemical exfoliation of graphite, there are not many studies on the electrochemical unzipping of MWCNTs. The driving force for the chemical unzipping process was proposed to be the oxidative cleavage of C–C bonds by the permanganate in acids. Similar to chemical unzipping, electrochemical unzipping focuses on cleaving the C–C bonds, which was accomplished by anodic oxidation of MWCNT in diluted sulfuric acids. However, there were difficulties in selectively cleaving the C–C bonds. For example, Lim et al.[100] showed that the incorporation of heteroatoms on MWCNTs is an essential step for selective MWCNT unzipping.

A recent study discovered that the overall unzipping process in chemical oxidative unzipping involves the same three steps as in

the course of graphite oxide production from graphite by the Hummers method: intercalation, oxidation, and exfoliation. Therefore, the current methods of electrochemical unzipping should be reconsidered.

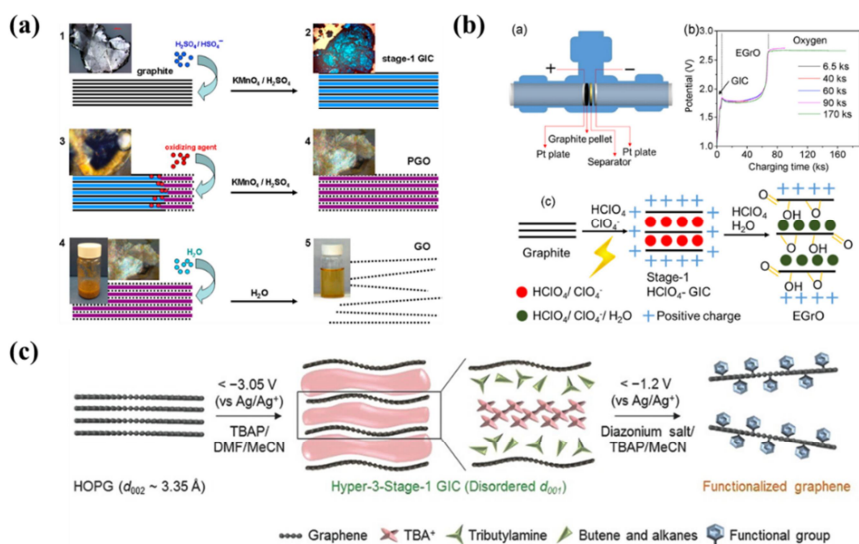


Figure 1.10. Mechanism of functionalized graphite formation (or graphite oxide in (a) and (b)) in (a) chemical and (b) anodic oxidation, and (c) cathodic reduction (from Refs. [76], [83], and [102]).

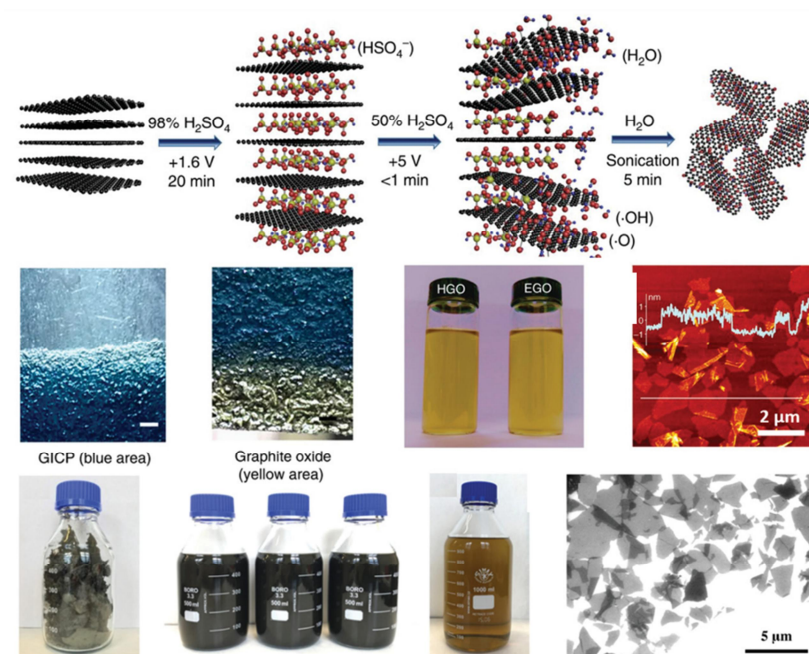


Figure 1.11. Anodic oxidation methods for preparing graphene oxide (from Ref. [81, 82])

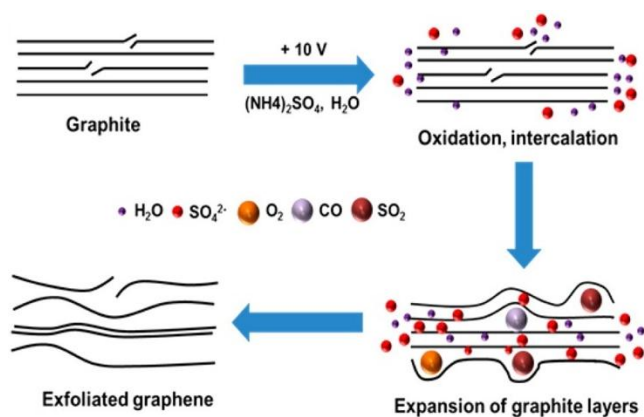


Figure 1.12. Production of few-layered graphene by the electrochemical exfoliation method (from Refs. [86]).

Table 1.2. Comparison of electrochemical synthesis for unzipping the single or multi-walled carbon nanotube.

Materials	Electrolyte	V	Yield (wt%)	I_D/I_G	Thickness	Ref.
HOPG/natural graphite	0.5 M H ₂ SO ₄ + KOH (pH \approx 1.2)	10 V	5–8	0.5–1.0	≤ 2 nm	[87]
Graphite foil	0.1 M H ₂ SO ₄	10 V	60	0.4	1–3 layers	[88]
Graphite foil	0.1 M (NH ₄) ₂ SO ₄	10 V	75	0.25	1–3 layers	[86]
Graphite foil	0.1 M (NH ₄) ₂ SO ₄	15 V	Not specified	0.4	1–2 layers	[89]
Graphite foil	0.1 M K ₂ SO ₄	10 V	Not specified	0.38	1–2 nm	[90]
Graphite rod	0.2 M (NH ₄) ₂ SO ₄	10 V	75	1.76	2	[91]
HOPG/graphite rod	0.1 M (NH ₄) ₂ SO ₄	10 V	Not specified	0.29	<5 layers	[92]
Graphite flake	0.1 M (NH ₄) ₂ SO ₄	10 V	65	0.9	2–7 nm	[93]
Graphite foil	0.1 M (NH ₄) ₂ SO ₄	10 V	Not specified	0.95	2.8 nm	[94]
Expanded graphite foil	0.1 M NaOH + 0.1 M Na ₂ SO ₄	10 V	Not specified	1.3	2–3 nm	[95]

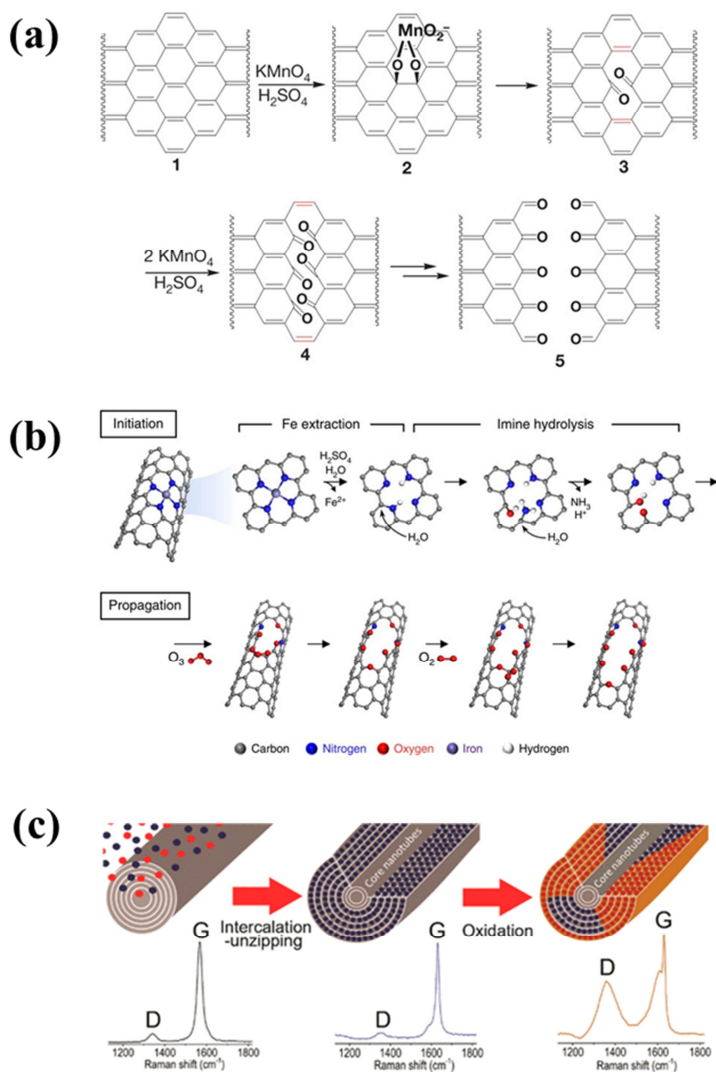


Figure 1.14. Previous mechanisms of (a) chemical and (b) electrochemical unzipping, and the current mechanism of (c) chemical unzipping (from Refs. [50, 52, 100]).

Table 1.3. Comparison of electrochemical unzipping methods for preparing GNRs.

Types of CNT	Mechanism	Working electrode	Reagents	Scalability (mass loading)	Ref.
Single- or multi-walled carbon nanotube	Oxidative cleavage of the C-C bond	GCE ^{a)} (Drop casting)	0.5 M H ₂ SO ₄	Difficult (2.5 µg)	[96]
Multi-walled carbon nanotube	Hetero atom dopant-specific unzipping	GCE ^{a)} (CNT forest on Si/SiO ₂ wafer transferred)	1 M H ₂ -SO ₄	Difficult (Not mentioned)	[97]
Single-walled carbon nanotube	Oxidative cleavage of the C-C bond	GCE ^{a)} (Drop casting)	0.5 M H ₂ SO ₄	Difficult (2.5 µg)	[98]
Multi-walled carbon nanotube	Oxidative cleavage of the C-C bond	GCE ^{a)} (Drop casting)	0.1 M H ₂ SO ₄	Difficult (10 µg)	[99]
Multi-walled carbon nanotube	Dopant-specific unzipping	GCE ^{a)} (CNT forest on Si/SiO ₂ wafer transferred)	1 M H ₂ -SO ₄	Difficult (Not mentioned)	[100]
Single-walled carbon nanotube	Oxidative cleavage of the C-C bond	GCE ^{a)} (Drop casting)	0.5 M H ₂ SO ₄	Difficult (5 µg)	[101]

^{a)}(GCE: glassy carbon electrode.)

1.5. Thesis overview

As described in the previous sections, solution-processable graphene and GNRs are promising alternatives in energy storage/conversion applications. However, the high cost and low supply are the major factors limiting their use.

Although chemical oxidation methods have kilogram-scale production capability, they suffer from safety and environmental issues due to the use of hazardous and explosive chemicals. Recently, electrochemical methods have been regarded as a facile, green, and scalable approach to prepare two-dimensional materials. In my thesis, I aim to describe the electrochemical preparation of graphene and GNRs, and demonstrate their usage in energy storage/conversion devices (*i. e.*, LIBs and electrocatalysts for HER).

Initially, electrochemical exfoliation of graphite was used to prepare graphene. EG was then used as a precursor to prepare a carbon-coated silicon-graphene nanocomposite film. Partially oxidized EG absorbed the microwave radiation and generated heat to simultaneously reduce the graphene and carbonize the polydopamine carbon precursor. The as-prepared carbon-coated silicon-graphene film was used as a LIB anode, exhibiting a reversible capacity of 1744 mAh g⁻¹ at a current density of 0.1 A g⁻¹ and 662 mAh g⁻¹ at 1.0 A g⁻¹ after 200 cycles. Thus, this method can potentially be a general approach to prepare various graphene

nanocomposites in an extremely short time.

In sequence, an electrochemical method was used to unzip MWCNTs. Unzipping of MWCNTs is one of the most promising strategies for the large-scale preparation of GNRs for use in a wide range of applications such as nanoelectronics, catalysis, and energy storage. However, current unzipping methods suffer from environmental and safety issues because of the use of toxic and explosive chemicals. Although several green approaches have been proposed to unzip MWCNTs, most of them are unscalable or are incapable of selective unzipping. In this study, an electrochemical intercalation strategy under ambient conditions is presented for the scalable preparation of GNRs. When MWCNTs are anodically oxidized in a concentrated acid electrolyte, they become longitudinally unzipped as soon as the material is completely intercalated; furthermore, few-layered GNRs are formed by a subsequent anodic oxidation reaction. This method can control the C/O ratio from 4 to 20 and the GNR unzipping level from partial to full unzipping. Moreover, the method can be scaled up to a rate of 100 g h^{-1} if a square meter-

sized electrode is used with simple washing processes. The as-prepared GNRs in this study were used as anodes for alkali ion capacitors in both organic and aqueous electrolytes and catalyst support for HER.

1.6 Reference

- [1] Kroto, H. W.; Heath, J. R.; O'Brien, S. C.; Curl, R. F.; Smalley, R. E. *Nature*, **1985**, 318, 162.
- [2] Iijima, S. *Nature*, **1991**, 354, 56.
- [3] Novoselov, K. S.; Geim, A. K.; Morozov, S. V.; Jiang, D.; Zhang, Y.; Dubonos, S. V.; Grigorieva, I. V.; Firsov, A. A. *Science*, **2004**, 306, 666.
- [4] Georgakilas, V.; Perman, J. A.; Tucek, J.; Zboril, R. *Chem. Rev.*, **2015**, 115, 4744.
- [5] Mermin, N. D.; Wagner, H. *Phys. Rev. Lett.*, **1996**, 17, 1133.
- [6] Stoller, M. D.; Park, S.; Zhu, Y.; An, J.; Ruoff, R. S. Graphene-based ultracapacitors. *Nano Lett.*, **2008**, 8, 3498.
- [7] Balandin, A. ; Ghosh, S. ; Bao, S. ; Calizo, I. ; Teweldebrhan, I. ; Miao, I. ; Lau, C.N. *Nano Lett.*, **2008**, 8, 902.
- [8] Lee, C; Wei, X.; Kysar, J. W.; Hone, J. *Science*, **2008**, 321, 385.
- [9] Geim, A. K.; Novoselov, K. S. *Nat. Mater.*, **2007**, 6, 183.

- [10] Cheng, H.; Huang, Y.; Shi, G.; Jiang, L.; Qu, L *Accounts of Chemical Research*, **2017** *50*, 1663
- [11] Nakada, K.; Fujita, M.; Dresselhaus, G.; Dresselhaus, M. *S. Phys. Rev. B: Condens. Matter Mater. Phys.*, **1996**, *54*, 17954
- [12] Bae, S.; Kim, H.; Lee, Y.; Xu, X.; Park, J.; Zheng, Y.; Balakrishnan, J.; Lei, T.; Kim, H.; Song, Y., *Nat. Nanotechnol.*, **2010**, *5*, 574
- [13] Schwierz, F. *Nat. Nanotechnol.*, **2010**, *5*, 487
- [14] Kim, K.S. ; Zhao, Y.; Jang, H.; Lee, S.Y.; Kim, J.M.; Kim, K.S.; Ahn, J.-H.; Kim, P.; Choi, J.-Y.; Hong, B.H.; *Nature*, **2009**, *457*, 706
- [15] Han, T.-H.; Lee, Y.; Choi, M.-R.; Woo, S.-H.; Bae, S.-H.; Hong, B. H.; Ahn, J.-H.; Lee, T.-W. *Nat. Photonics*, **2012**, *6*, 105
- [16] Kittner, N.; Lill, F.; Kammen, D. M. *Nat. Energy*, **2017**, *2*, 17125
- [17] El-Kady, M. F.; Shao, Y.; Kaner, R. B. *Nat. Rev. Mater.*, **2016**, *1*, 16033
- [18] Li, H.; Tao, Y.; Zheng, X.; Luo, J.; Kang, F.; Cheng, H.-M.; Yang, Q.-H. *Energy Environ. Sci.*, **2016**, *9*, 3135
- [19] Fang, R.; Chen, K.; Yin, L.; Sun, Z.; Li, F.; Cheng, H.-M. *Adv. Mater.*, **2018**, *30*, 1800863
- [20] Wang, L.; Sofer, Z.; Pumera, M. *ACS Nano*, **2020**, *14*, 1,
- [21] Pan, Z.; Liu, M.; Yang, J.; Qiu, Y.; Li, W.; Xu, Y.; Zhang, X.; Zhang, Y. *Adv. Funct. Mater.*, **2017**, *27*, 1701122
- [22] Teng, Y.; Zhao, H.; Zhang, Z.; Li, Z.; Xia, Q.; Zhang, Y.; Zhao, L.; Du, X.; Du, Z.; Lv, P.; Świerczek, K. *ACS Nano*, **2016**, *10*, 8526

- [23] Ye, S.; Luo, F.; Zhang, Q.; Zhang, P.; Xu, T.; Wang, Q.; He, D.; Guo, L.; Zhang, Y.; He, C.; Ouyang, X.; Gu, M.; Liu, J.; Sun, X. *Energy Environ. Sci.*, **2019**, *12*, 1000
- [24] Armand, M.; Tarascon, J. M. *Nature*, **2008**, *451*, 652.
- [25] Goodenough, B.; Park, K. S.; *J. Am. Chem. Soc.*, **2013**, *135*, 1167.
- [26] Persson, K.; Sethuraman, V. A.; Hardwick, L. J.; Hinuma, Y.; Meng, Y. S.; Van der Ven, A.; Srinivasan, V.; Kostecki, R.; Ceder, G.; *J. Phys. Chem. Lett.*, **2010**, *1*, 1176.
- [27] Lian, P.; Zhu, X.; Liang, S.; Li, Z.; Yang, W.; Wang, H. *Electrochim. Acta*, **2010**, *55*, 3909
- [28] Uthaisar, C.; Barone, V.; Peralta, J. E. *J. Appl. Phys.* **2009**, *106*, 113715
- [29] Mo, R.; Li, F.; Tan, X.; Xu, P.; Tao, R.; Shen, G.; Lu, X.; Liu, F.; Shen, L.; Xu, B.; Xiao, Q.; Wang, X.; Wang, C.; Li, J.; Wang, G.; Lu, Y. *Nat. Commun.* **2019**, *10*, 1474.
- [30] Conway, B. E. *Electrochemical Supercapacitors*; Springer: Boston, MA, **1999**.
- [31] Simon, P.; Gogotsi, Y. *Nat. Mater.*, **2008**, *7*, 845.
- [32] Li, Z.; Gadipelli, S.; Li, H.C.; Howard, C.A.; Brett, D.J.L.; Shearing, P.R.; Guo, Z.X.; Parkin, I.P.; Li, F.; *Nat Energy*, **2020**, *5*, 160
- [33] Raccichini, R.; Varzi, A.; Passerini, S.; Scrosati, B. *Nat. Mater.*, **2014**, *14*, 271
- [34] Li, L.; Ruan, G.; Peng, Z.; Yang, Y.; Fei, H.; Raji, A. R.; Samuel, E. L.; Tour, J. M. *ACS Appl. Mater. Interfaces*, **2014**, *6*, 15033
- [35] Lim, J.; Lee, G. Y.; Lee, H. J.; Cha, S. K.; Choi, D. S.; Koo,

- S. H.; Lee, W. J.; Kim, S. O. *Energy Storage Mater.*, **2019**, 16, 251
- [36] Jiang, J.; Li, Y.; Liu, J.; Huang, X.; Yuan, C.; Lou, X. W. *Adv. Mater.*, **2012**, 24, 5166– 5180
- [37] Raccichini, R.; Varzi, A.; Wei, D.; Passerini, S. *Adv. Mater.*, **2017**, 29, 1603421
- [38] Meng, X.; Lu, L.; Sun, C. *ACS Appl. Mater. Interfaces*, **2018**, 10, 16474
- [39] Zheng, Y.; Jiao, Y.; Jaroniec, M.; Qiao, S. Z. *Angew. Chem., Int. Ed.*, **2015**, 54, 52
- [40] Wang, X.-D.; Xu, Y.-F.; Rao, H.-S.; Xu, W.-J.; Chen, H.-Y.; Zhang, W.-X.; Kuang, D.-B.; Su, C.-Y. *Energy Environ. Sci.*, **2016**, 9, 1468
- [41] Chhowalla, M.; Shin, H. S.; Eda, G.; Li, L. J.; Loh, K. P.; Zhang, H. *Nat. Chem.*, **2013**, 5, 263
- [42] Gao, W.; Shi, Y. Q.; Zhang, Y. F.; Zuo, L. Z.; Lu, H. Y.; Huang, Y. P.; Fan, W.; Liu, T. X. *ACS Sustainable Chem. Eng.* **2016**, 4, 6313
- [43] Kong, W. ; Kum, H. ; Bae, S. H. ; Shim, J. ; Kim, H. ; Kong, L.; Meng, Y.; Wang, K.; Kim, C.; Kim, J.; *Nat. Nanotechnol.*, **2019**, 14, 927.
- [44] Wang, X.-Y.; Narita, A.; Müllen, K. *Nat. Rev. Chem.*, **2017**, 2, 0100
- [45] Nicolosi, V.; Chhowalla, M.; Kanatzidis, M. G.; Strano, M. S.; Coleman, J. N. *Science*, **2013**, 340, 1420
- [46] Yang, W.; Ratinac, K.R.; Ringer, S.P.; Thordarson, P.; Gooding, J.J.; Braet, *Angew. Chem. Int.*, **2010**, 49, 2114.
- [47] Fang, S.; Lin, Y.; Hu, Y. H. *ACS Sustainable Chem. Eng.*, **2019**, 7, 12671

- [48] Ma, L.; Wang, J.; Ding, F. *ChemPhysChem.*, **2013**, 14, 47
- [49] Narita, A.; Chen, Z.; Chen, Q.; Müllen, K. *Chem. Sci.*, **2019**, 10, 964
- [50] Kosynkin, D. V.; Higginbotham, A. L.; Sinitskii, A.; Lomeda, J. R.; Dimiev, A.; Price, B. K.; Tour, J. M. *Nature.*, **2009**, 458, 872
- [51] Kosynkin, D. V.; Lu, W.; Sinitskii, A.; Pera, G.; Sun, Z.; Tour, J. M. *ACS Nano*, **2011**, 5, 968
- [52] Dimiev, A. M.; Khannanov, A.; Vakhitov, I.; Kiiamov, A.; Shukhina, K.; Tour, J. M. *ACS Nano*, **2018**, 12, 3985
- [53] Su, C.-Y.; Lu, A.-Y.; Xu, Y.; Chen, F.-R.; Khlobystov, A. N.; Li, L.-J. *ACS Nano*, **2011**, 5, 2332
- [54] Lukatskaya, M. R.; Halim, J.; Dyatkin, B.; Naguib, M.; Buranova, Y. S.; Barsoum, M. W.; Gogotsi, Y. *Angew. Chem., Int. Ed.*, **2014**, 53, 4877
- [55] Liu, N.; Kim, P.; Kim, J. H.; Ye, J. H.; Kim, S.; Lee, C. J. *ACS Nano*, **2014**, 8, 6902
- [56] Ambrosi, A.; Sofer, Z.; Pumera, M. *Angew. Chem., Int. Ed.*, **2017**, 56, 10443
- [57] Yu, P.; Lowe, S. E.; Simon, G. P.; Zhong, Y. L. *Curr. Opin. Colloid Interface Sci.*, **2015**, 20, 329
- [58] Wang, H.; Lu, Z.; Xu, S.; Kong, D.; Cha, J. J.; Zheng, G.; Hsu, P.-C.; Yan, K.; Bradshaw, D.; Prinz, F. B.; Cui, Y. *Proc. Natl. Acad. Sci. U.S.A.*, **2013**, 110, 19701
- [59] Shuai, H.; Ge, P.; Hong, W.; Li, S.; Hu, J.; Hou, H.; Zou, G.; Ji, X. *Small Methods*, **2019**, 3, 1800328
- [60] Liu, N.; Luo, F.; Wu, H.; Liu, Y.; Zhang, C.; Chen, J. *Adv. Funct. Mater.*, **2008**, 18, 1518
- [61] Suo, L.; Borodin, O.; Gao, T.; Olguin, M.; Ho, J.; Fan,

- X.; Luo, C.; Wang, C.; Xu, K. *Science*, **2015**, 350, 938
- [62] Ambrosi, A.; Pumera, M. *Chem. Soc. Rev.* **2018**, 47, 7213
- [63] Inagaki, M.; Tashiro, R.; Washino, Y.; Toyoda, M. *J. Phys. Chem. Solids*, **2004**, 65, 133.
- [64] Kakaei, K. *Carbon*, **2013**, 51, 195
- [65] Lu, X.; Zhao, C. *Phys. Chem. Chem. Phys.*, **2013**, 15, 20005
- [66] Zhang, Y.; Xu, Y. *Adv. Funct. Mater.*, 2019, 29, 1902171.
- [67] Rao, K. S.; Senthilnathan, J.; Liu, Y.-F.; Yoshimura, M. *Sci. Rep.*, **2014**, 4, 4237
- [68] Tang, H.; He, P.; Huang, T.; Cao, Z.; Zhang, P.; Wang, G.; Wang, X.; Ding, G.; Xie, X. *Carbon*, **2019**, 143, 559
- [69] Sharif, F.; Zeraati, A. S.; Ganjeh-Anzabi, P.; Yasri, N.; Perez-Page, M.; Holmes, S. M.; Sundararaj, U.; Trifkovic, M.; Roberts, E. P. *Carbon*, **2020**, 157, 681
- [70] Yang, S.; Bruller, S.; Wu, Z. S.; Liu, Z. Y.; Parvez, K.; Dong, R. H.; Richard, F.; Samori, P.; Feng, X. L.; Mullen, K. *J. Am. Chem. Soc.*, **2015**, 137, 13927
- [71] Viculis, L. M.; Mack, J. J.; Mayer, O. M.; Hahn, H. T.; Kaner, R. B. *J. Mater. Chem.*, **2005**, 15, 974
- [72] Dresselhaus, M. S.; Dresselhaus, G. Intercalation Compounds of Graphite *Adv. Phys.*, **2002**, 51, 1
- [73] Shioyama, H.; Fujii, R. *Carbon*, **1987**, 25, 771
- [74] Metrot, A.; Fischer, J. E. *Synth. Met.*, **1981**, 3, 201
- [75] Besenhard, J. O.; Wudy, E.; Möhwald, H.; Nickl, J.; Biberacher, W.; Foag, W. *Synth. Met.*, **1983**, 7, 185
- [76] Dimiev, A. M.; Tour, J. M. *ACS Nano*, **2014**, 8, 3060
- [77] Hummers, W. S., Jr.; Offeman, R. E. *J. Am. Chem. Soc.*, **1958**, 80, 1339

- [78] Kang, J. H.; Kim, T.; Choi, J.; Park, J.; Kim, Y. S.; Chang, M. S.; Jung, H.; Park, K. T.; Yang, S. J.; Park, C. R. *Chem. Mater.*, **2016**, 28, 756
- [79] Hudson, M. J.; Hunter-Fujita, F. R.; Peckett, J. W.; Smith, P. M. *J. Mater. Chem.*, **1997**, 7, 301
- [80] Lowe, S. E.; Shi, G.; Zhang, Y.; Qin, J.; Wang, S.; Uijtendaal, A.; Sun, J.; Jiang, L.; Jiang, S.; Qi, D.; Al-Mamun, M.; Liu, P.; Zhong, Y. L.; Zhao, H. *ACS Appl. Nano Mater.*, **2019**, 2, 867
- [81] Cao, J.; He, P.; Mohammed, M. A.; Zhao, X.; Young, R. J.; Derby, B.; Kinloch, I. A.; Dryfe, R. A. W. *J. Am. Chem. Soc.*, **2017**, 139, 17446
- [82] Pei, S.; Wei, Q.; Huang, K.; Cheng, H.-M.; Ren, W. *Nat. Commun.*, **2018**, 9, 145
- [83] Jeon, I.; Yoon, B.; He, M.; Swager, T. M. *Adv. Mater.*, **2018**, 30, 1704538
- [84] Yang, S.; Lohe, M. R.; Müllen, K.; Feng, X. *Adv. Mater.*, **2016**, 28, 6213
- [85] Hathcock, K. W.; Brumfield, J. C.; Goss, C. A.; Irene, E. A.; Murray, R. W. *Anal. Chem.*, **1995**, 67, 2201
- [86] Parvez, K.; Wu, Z.-S. S.; Li, R.; Liu, X.; Graf, R.; Feng, X.; Müllen, K. *J. Am. Chem. Soc.*, **2014**, 136, 6083
- [87] Su, C. Y.; Lu, A. Y.; Xu, Y. P.; Chen, F. R.; Khlobystov, A. N.; Li, L. J. *ACS Nano*, **2011**, 5, 2332
- [88] Parvez, K.; Li, R. J.; Puniredd, S. R.; Hernandez, Y.; Hinkel, F.; Wang, S. H.; Feng, X. L.; Müllen, K. *ACS Nano*, **2013**, 7, 3598
- [89] Eredia, M.; Bertolazzi, S.; Leydecker, T.; El Garah, M.; Janica, I.; Melinte, G.; Ersen, O.; Ciesielski,

- A.; Samorì, P. *J. Phys. Chem. Lett.*, **2017**, 8, 3347
- [90] Munuera, J. M.; Paredes, J. I.; Villar-Rodil, S.; Ayán-Varela, M.; Pagán, A.; Aznar-Cervantes, S. D.; Cenis, J. L.; Martínez-Alonso, A.; Tascón, J. M. *D. Carbon*, **2015**, 94, 729
- [91] Sevilla, M.; Ferrero, G. A.; Fuertes, A. B. *Chem Eur J.*, **2016**, 22, 17351
- [92] Chen, D.; Wang, F.; Li, Y.; Wang, W.□W.; Huang, T.□X.; Li, J.□F.; Novoselov, K. S.; Tian, Z.□Q.; Zhan, D. *Chem. Commun.*, **2019**, 55, 3379
- [93] Achee, T. C.; Sun, W.; Hope, J. T.; Quitzau, S. G.; Sweeney, C. B.; Shah, S. A.; Habib, T.; Green, M. J. *Sci. Rep.*, **2018**, 8, 14525
- [94] Ambrosi, A.; Pumera, M.; *Chem. □ Eur. J.*, **2016**, 22, 153.
- [95] Liu, Z.; Zhang, H.; Eredia, M.; Qiu, H.; Baaziz, W.; Ersen, O.; Ciesielski, A.; Bonn, M.; Wang, H. I.; Samorì, P. *ACS Nano*, **2019**, 13, 9431.
- [96] Shinde, D. B.; Debgupta, J.; Kushwaha, A.; Aslam, M.; Pillai, V. K. *J. Am. Chem. Soc.*, **2011**, 133, 4168.
- [97] Sasikala, S. P.; Yun, T.; Choi, D. S.; Jeong, M. S.; *ACS Appl. Mater. Interfaces*, **2019**, 11, 38006.
- [98] Debgupta, J.; Shinde, D. B.; Pillai, V. K. *Chem. Commun.*, **2012**, 48, 3088.
- [99] Jaison, M. J.; Narayanan, T. N.; Prem Kumar, T.; Pillai, V. K. *J. Mater. Chem., A* **2015**, 3, 18222.
- [100] Lim, J.; Maiti, U. N.; Kim, N. Y.; Narayan, R.; Lee, W. J.; Choi, D. S.; Oh, Y.; Lee, J. M.; Lee, G. Y.; Kang, S. H.; Kim, H. Kim, Y. H.; Kim, S. O. *Nat. Commun.*, **2016**, 7,

10364.

- [101] John, R.; Shinde, D. B.; Liu, L.; Ding, F.; Xu, Z.; Vijayan, C.; Pillai, V. K.; Pradeep, T. *ACS Nano*, **2014**, 8, 234.
- [102] Tian, Z.; Yu, P.; Lowe, S. E.; Pandolfo, A. G.; Gengenbach, T. R.; Nairn, K. M.; Song, J.; Wang, X.; Zhong, Y. L.; Li, D. *Carbon* **2017**, 112, 185

Chapter 2. Electrochemically Exfoliated Graphene as a Novel Microwave Susceptor: the Ultrafast Microwave-assisted Synthesis of Carbon-coated Silicon-graphene Film as Lithium-ion Battery Anode

2.1. Introduction

Graphene nanocomposites have been studied in a wide variety of applications such as energy storage device[1-7], photovoltaic devices [8-10], sensors[11,12] and catalysts[13-15] due to synergistic effects between graphene and certain nanomaterials. With superior electric conductivity and large surface area, graphene is an ideal substrate for nanomaterials. Graphene

nanocomposites have been synthesized using various techniques, such as direct nanoparticle growth via chemical reaction [2-6], electrospinning [8], self-assembly [9] and radiation-based thermal shock [7]. Graphene oxide (GO) is the most common graphene precursor for the synthesis of graphene nanocomposites because its synthesis can easily be scaled-up and the low-cost[16-19]. Moreover, GO can be easily dispersed in an aqueous solution due to its functional groups, which is crucial for the synthesis of many graphene nanocomposite. However, GO requires an inevitable reduction procedure to restore its Sp^2 domain to obtain high electric conductivity[20]. Two common reduction methods are thermal reduction and chemical reduction[20]. Thermal treatment usually requires exposing the sample to high temperature (600 - 700 °C) for several hours, while chemical reduction generally uses very toxic and environmentally unfriendly reducing agents such as hydrazine and sodium borohydride.

A few years ago, an alternative microwave irradiation method was introduced to reduce and exfoliate GO [21-23]. In less than a minute, GO can be reduced and exfoliated by microwave

irradiation. The Sp^2 domains of GO absorb microwave radiation and induces high dielectric loss which generates enough heat to reduce GO. Many researchers have used this microwave absorption property of graphene to synthesize various graphene nanocomposites[24-28]. However, most research used reduced graphene oxide (rGO) as a microwave susceptor and a heat generator since GO is not an efficient microwave susceptor[24,25,29]. The oxidation level of GO is a very important factor for microwave absorption[23]. If GO is too oxidized, which is the case of most GO obtained directly from Hummer's method, Sp^2 domain becomes small and microwave energy conversion is inefficient[23]. To generate enough heat, efficient microwave energy conversion is required by increasing the size of the electrically conductive regions. However, when the electrical conductivity is too high, the material will reflect most of the microwave leading to inefficient microwave conversion to heat. Thus, the latest research has focused on using mildly reduced GO as a microwave susceptor, which requires a time and energy consuming thermal treatment[24,25,27,29].

Herein, I introduce electrochemically exfoliated graphene (EG) as a good microwave susceptor in the synthesis of graphene nanocomposites, eliminating the need for any pre-thermal treatment. Unlike GO prepared by Hummer's method, EG prepared by anodic exfoliation has larger Sp² domain for the efficient microwave absorption and can be prepared in a short amount of time. Yet, there are still unavoidable oxygen functional groups formation that requires a reduction process [30,31]. During electrochemical exfoliation, these functional groups facilitate intercalation of anions and enables higher exfoliation degree of graphene [32-34]. However, the most functional groups are located on the edge of graphene not on the basal plane, which allows EG to disperse in alcohol medium for graphene nanocomposite synthesis while maintaining sufficient Sp² domains for the efficient microwave energy conversion.

Therefore, I propose a rapid and simple simultaneous reduction and carbonization method to prepare graphene-silicon nanocomposite film by microwave irradiation using EG. I used polydopamine-coated silicon nanoparticles as nanomaterials.

Using microwave irradiation (3 - 4s), I successfully carbonized a polydopamine layer while reducing EG at the same time. The prepared material was used as a lithium-ion battery anode and electrochemically tested. I think that this study has the following novelties. First, I show that EG is a very good microwave susceptor for microwave-assisted graphene nanocomposite synthesis since it does not require a mild reduction process to absorb microwave efficiently. Second, this method saves time and energy compared to the conventional heat treatment and is non-toxic and environmentally friendly compared to chemical reducing method. Third, it can be done with a commercial microwave. So it doesn't require any special expensive equipment. Fourth, I show that polydopamine can be carbonized by the heat generated from microwave irradiating of EG. This can potentially be an extremely rapid and simple general approach for carbonizing various carbon precursors or synthesizing many materials that require high temperature and much time.

2.2. Experimental method

Synthesis of electrochemically exfoliated graphene

Electrochemically exfoliated graphite was synthesized by electrochemically exfoliating graphite foil in two-electrode system. Graphite foil (Alfa Aesar, 99.8 %, 0.254mm) was used as a working electrode and a platinum wire was used as counter electrode. 0.1 M $(\text{NH}_4)_2\text{SO}_4$ solution (DAEJUNG chemicals, 99 %) was used as an electrolyte. 10 V was applied between two electrodes and kept until the exfoliation was finished. Then the product was collected by vacuum filtration using a cellulose membrane filter and washed with deionized water (DI water) several times to remove remaining salts. The washed product was redispersed in 2-propanol (SAMCHUN chemical, 99.5 %) and sonicated for 30 min. To remove non-exfoliated graphite aggregates, the product solution was centrifuged at 2000 rpm for 30 min.

Polydopamine coating for silicon nanoparticles

200 mg of silicon nanoparticles (<100 nm, American elements) were dispersed in ethanol (3 ml) and sonicated for 10 min. DI water (200 ml) was added to the suspension. Then, 10mM Tris-buffer solution (Sigma Aldrich) were added to the suspension. Then, dopamine hydrochloride solution (Sigma Aldrich, 3 mg mL⁻¹) was added to the above suspension and stirred for 15 min. After 15 min, the suspension was washed three times with DI water and freeze-dried for 24 h. Then, polydopamine-coated silicon nanoparticles were obtained.

Synthesis of reduced electrochemically exfoliated graphene-silicon nanocomposite film

For silicon-anodically exfoliated graphene film (Si-EG), silicon nanoparticles suspension (1 mg mL⁻¹) in 2-propanol (SAMCHUN chemical, 99.5 %) was put into as-prepared electrochemically exfoliated graphene suspension (0.16 mg mL⁻¹) by the volume ratio of 1.00:4.16 which corresponds to the 6:4

weight ratio of silicon nanoparticles to graphene. The mixture was sonicated for 30 min and was then vacuum filtered using an anodized aluminum oxide (AAO) membrane (Whatman, Anodisc 47, 0.2 μm pore diameter). A greenish film on the AAO membrane was dried at 80 $^{\circ}\text{C}$ in air for 30 min and gathered.

For polydopamine-coated silicon-electrochemically exfoliated graphene film (pSi-EG), as-prepared polydopamine-coated silicon nanoparticles suspension (1 mg ml^{-1}) in 2-propanol (SAMCHUN chemical, 99.5 %) was put into as-prepared electrochemically exfoliated graphene suspension (0.16 mg ml^{-1}) by the same volume ratio above. Then, the mixture was processed in the same manner with Si-EG.

For heat-treated silicon-anodically exfoliated graphite film (HTSi-EG) and heat-treated polydopamine-coated silicon-electrochemically exfoliated graphene film (HTpSi-EG), Si-EG or pSi-EG were thermally treated in Ar atmosphere for 5 h at 700 $^{\circ}\text{C}$ with a ramp rate of 5 $^{\circ}\text{C min}^{-1}$.

Microwave irradiation

Each Si-EG and pSi-EG film were cut into disks (1.1 cm diameter). Each disk was put into a vial. The vials were transferred to Ar-filled glove box (<1 ppm, O_2) and then sealed. The vials were irradiated in a commercial microwave (RE-C21VW, SAMSUNG, 700 W, 2.45 GHz,) for 3 - 4 seconds until blue plasma occurred.

Material characterization

Field emission scanning electron microscopy (FE-SEM, Hitachi S-4800, 15 kV) was used to examine the structural morphology of the sample. High resolution-transmission electron microscopy (HR-TEM) (JEOL JEM-2100F, 200 keV) equipped with an energydispersive X-ray spectrometer (EDS) was utilized for the detail structure examination. X-ray diffractometer (Bruker New D8 Advance, 40 kV, 40 mA) with a Cu target was used to measure the crystallinity of the sample. Raman spectrometer (Dongwoo optron, DM500i) equipped with an Ar laser (514 nm)

was utilized for Raman analysis. TGA/DSC 1 analyzer (Mettler Toledo) conducted Thermal gravimetric analysis (TGA) measurement with a ramp rate of 10 °C min⁻¹ in air. X-ray photoelectron spectroscopy (XPS) spectra were obtained by AXIS-His spectrometer (KRATOS). Electrical conductivity was measured by a resistivity meter (DASOLENG, FPP-40K).

Electrochemical measurement

The samples were used as electrodes directly. The loading mass is ~ 0.8 mg cm⁻². The specific capacity was calculated based on the total weight of electrode. The thickness of electrodes was about 25 µm. Coin-type cells (CR2016) were assembled in Ar-filled glove box (<1 ppm, O₂) with a lithium metal disk as a counter and a reference electrode. A separator was Celgard 2400. An electrolyte was 1.3 M LiPF₆ in 3:7(v/v) ethylene carbonate (EC) and diethylene carbonate (DEC) with 10 % fluoroethylene carbonate (FEC) (PANAX). The half-cells were galvanostatically measured with a voltage range between 0.01 - 2.0 V (vs. Li/Li⁺). Every galvanostatic evaluation and cyclic voltammetry was

performed on a WBCS3000S (Wonatech). Electrochemical impedance spectroscopy (EIS) was performed at open-circuit voltage in a frequency range between 100 mHz – 10 kHz with a voltage amplitude of 10 mV using a ZIVE SP1 (ZIVE Lab).

2.3. Results and discussion

Figure 2.1 depicts an experimental procedure to synthesize a microwave irradiated polydopamine-coated silicon-electrochemically exfoliated graphite film (MWpSi-EG). Electrochemically exfoliated graphene was prepared using the anodic exfoliation of graphite foil in 0.1M ammonium sulfate. Parvez et al. found that anodic exfoliation of graphite foil (0.13mm, Alfa Aesar) occurs very rapidly (<10 min) and produces graphene with very low oxygen content. Unlike their report, GF (0.254mm, Alfa Aesar) used in this experiment exfoliated slowly (~22 minutes) and longer exposed to the anodic oxidation. The yield was calculated to be 62.5% and the average thickness of the exfoliated graphite flake is nearly 4 nm (**Figure 2.2**). Raman and X-ray photoelectron spectroscopy (XPS) analysis were used to

analyze the oxidation degree of EG. **Figure 2.3a** shows the representative Raman spectra of the EG. The spectra exhibit three characteristic bands: G (1560 cm^{-1}), D (1320 cm^{-1}) and D' (1620 cm^{-1}) that are related to structure properties of graphitic carbons. D and D' bands (1620 cm^{-1}) are related to surface defects and G bands are related to in plane graphitic bonding. The D and G band intensity ratio (I_D/I_G) has been used to characterize the crystalline defects of graphitic materials. The EG shows the I_D/I_G of 1.25. In XPS analysis, the carbon/oxygen (C/O) ratio of EG determined is 4.6 (**Figure 2.3b**). These results indicate that EG is less oxidized compared to chemically prepared graphene oxides (C/O from 2.0 to 2.7).

This procedure utilizing microwave irradiation is much faster and requires less energy than a conventional heat treatment procedure to reduce graphene and carbonize polydopamine. During microwave irradiation, a red light appeared followed by blue plasma (**Figure 2.4**). The detailed mechanism of this phenomenon is not clear, but I assume that the red light is thermal radiation caused by intense heating. In conductive materials, microwave

irradiation drives free electron to oscillate collectively, resulting in Joule heating. Previous reports mention that the heat generated by microwave irradiation increases linearly with graphene's conductivity [35-37]. This intense heating could cause electrons in graphene to thermally emit light in the visible spectrum. This might be the origin of the red light emitted at the early stage of microwave irradiation. As explained above, microwave irradiation drives free electrons to oscillate collectively. During charge oscillation, sharp edges on graphene films produce a concentrated electric field. This concentrated electric field will cause ionization of the surrounding argon atmosphere, which is observed as blue light.

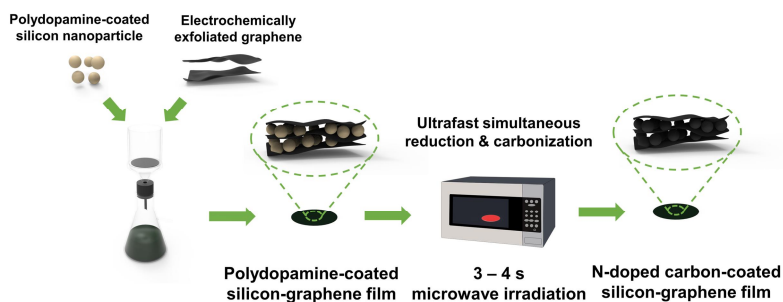


Figure 2.1. Schematic illustration of a synthesis procedure for microwave irradiated polydopamine-coated silicon-electrochemically exfoliated graphene film (MWpSi-EG).

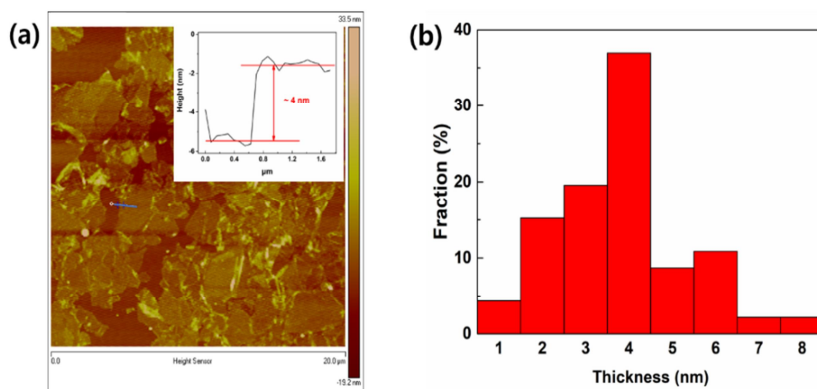


Figure 2.2. (a) AFM image on SiO_2 substrate and (b) thickness distribution of anodically exfoliated graphene (50 flakes)

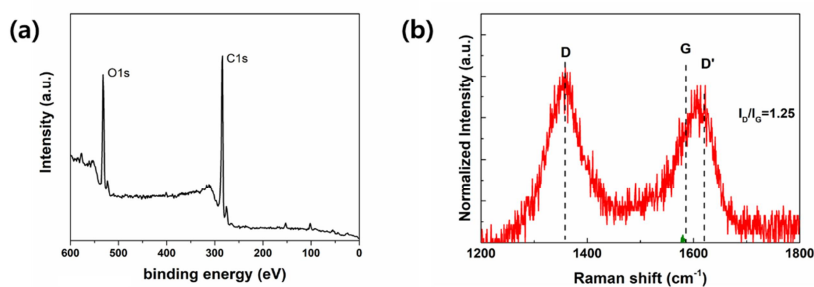
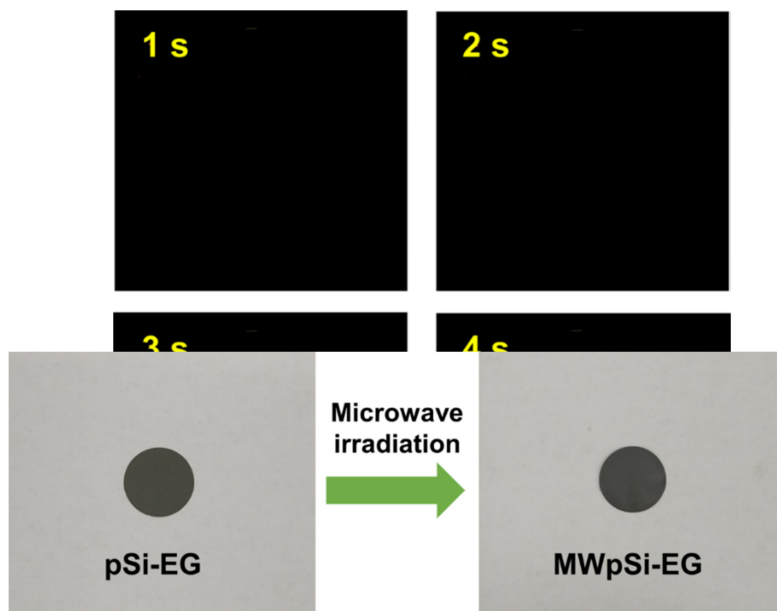


Figure 2.3. (a) Wide scan XPS spectra and (b) Raman

Figure 2.4. Digital photo images of a microwave irradiation process for pSi-EG. The yellow arrow indicates a red arc.

Figure 2.5 shows digital photo images of pSi-EG and MWpSi-



EG. The MWpSi-EG film maintains its original shape after microwave irradiation but exhibits small bumps on its surface, as shown in **Figure 2.6**. I hypothesize that these small bumps are generated by vapor from graphene and polydopamine during irradiation. Violent fuming could possibly generate these small bumps since the rapid carbonization and reduction might cause a relatively large amount of vapor. Therefore, these bumps can be an indirect evidence of reduction of graphene and carbonization of polydopamine.

Figure 2.5. Digital photo image of pSi-EG and MWpSi-EG.

Figure 2.6. SEM image of the surface of MWpSi-EG with low magnification. The yellow arrows indicate micro-sized bumps.

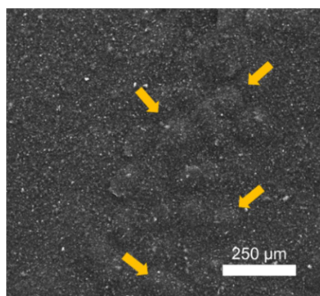


Figure 2.7 shows scanning electron microscopy (SEM) images of silicon-anodically exfoliated graphite film (Si-

EG), microwave irradiated silicon-electrochemically exfoliated graphene film (MWSi-EG) and microwave irradiated polydopamine-coated silicon-anodically exfoliated graphite film (MWpSi-EG). In Si-EG, silicon nanoparticles (< 100 nm) are well sandwiched between graphene sheets. Interestingly, microwave irradiated MWSi-EG film shows sintered and larger silicon nanoparticles, as shown in **Figure 2.8**.

During the microwave irradiation, silicon nanoparticles were sintered and smaller silicon nanoparticles merged with near bigger silicon nanoparticles because of large thermal energy. Sintering of silicon particles with oxide layers on its surface usually requires a very high temperature (> 1000 °C) [38]. Thus, sintered silicon nanoparticles is a direct evidence of high-temperature reaction conditions. On the contrary, MWpSi-EG shows almost the same morphology as Si-EG, which might be attributed to the polydopamine coating of silicon nanoparticles. Polydopamine coating may act as a protective layer so each silicon nanoparticle maintained its morphology at such high temperature [39, 40].

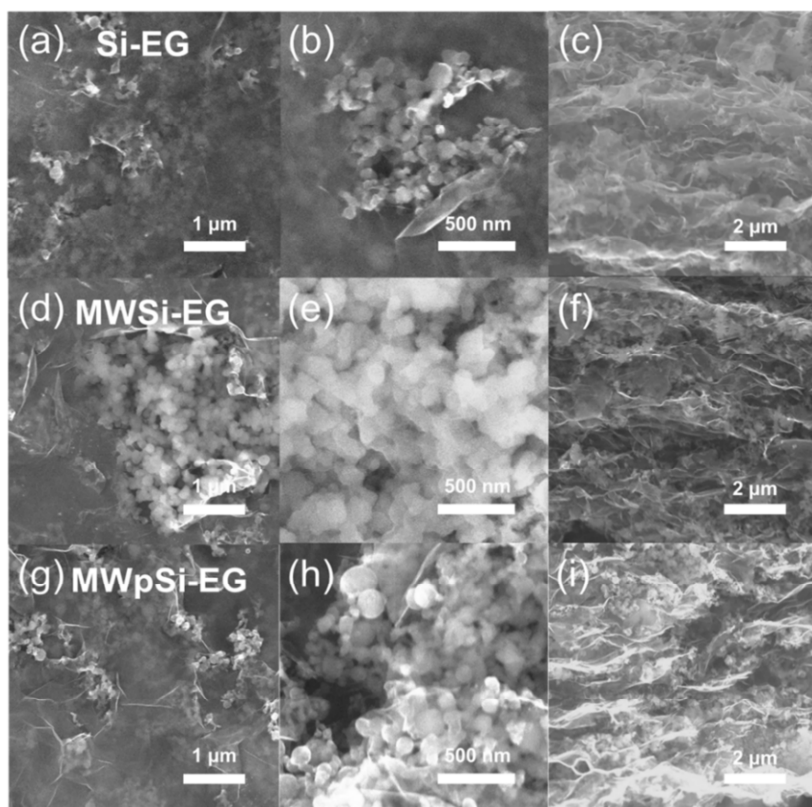
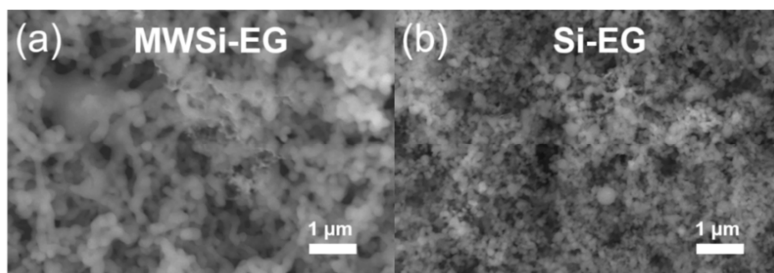


Figure 2.7. Surface SEM image of (a,b) Si-EG, (d,e) MWSi-EG and (g,h) MWpSi-EG with low and high magnification. Cross-



sectional SEM image of (c) Si-EG, (f) MWSi-EG and (i) MWpSi-

EG.

Figure 2.8. SEM image of the exposed surface of (a) MWSi-EG and (b) Si-EG.

To investigate the structure of MWpSi-EG in detail, high-resolution transmission electron microscopy (HR-TEM) was conducted. **Figure 2.9** shows silicon nanoparticles on graphene sheets. As shown in **Figure 2.9b-c**, each silicon nanoparticle is individually coated by a carbonized polydopamine layer. The crystal lattice of the carbon layer can be seen in **Figure 2.9d**. The d-spacing is measured as 0.42 nm which corresponds to the d-spacing of carbonized polydopamine [41]. As a reference, heat-treated polydopamine-coated silicon-anodically exfoliated graphite film (HTpSi-EG) was also examined using HR-TEM (**Figure 2.10**). The d-spacing of carbonized polydopamine in HTpSi-EG is 0.42 nm as expected. Since the thickness of the total layer is about 5 nm and an oxide layer on a silicon nanoparticle is about 2 - 3 nm (**Figure 2.11**), the thickness of carbon coating of MWpSi-EG is about 2- 3nm. **Figure 2.9e** shows Energy-

dispersive X-ray spectroscopy (EDS) analysis images of an N-doped carbon-coated silicon nanoparticle in MWpSi-EG. The silicon and the oxygen from the native oxide layer can be clearly observed. Importantly, **Figure 2.9e** clearly shows that the area of the mapped carbon is slightly larger than that of oxygen.

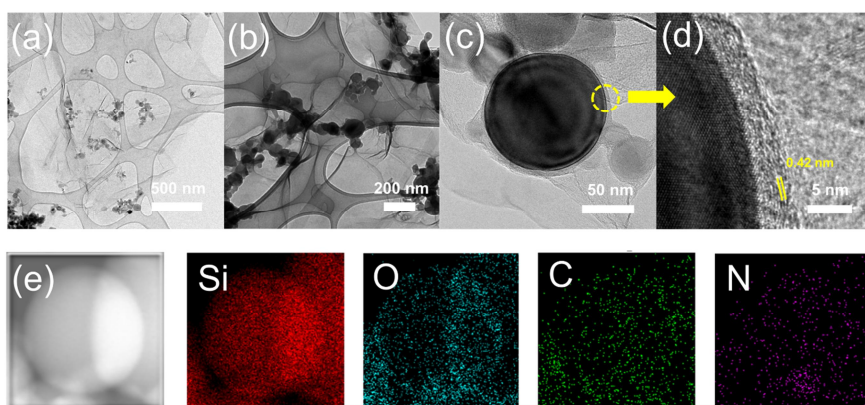


Figure 2.9. HR-TEM images of MWpSi-EG with (a-b) low magnification and (c-d) high magnification. (d) is a magnified image of yellow circled region in (c). (e) EDS analysis images of MWpSi-EG with the element mapping of silicon, oxygen, carbon and nitrogen.

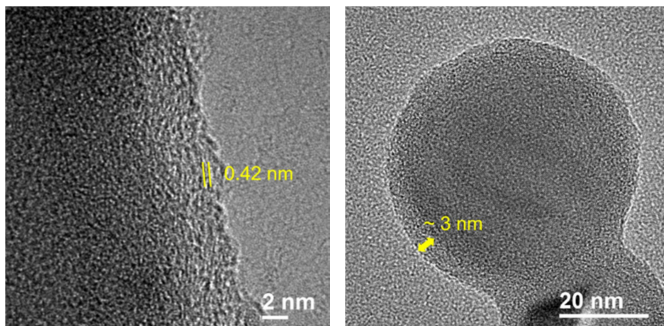


Figure 2.10. HR-TEM image of HTPSi-EG, **Figure 2.11.** bare silicon nanoparticle with a native oxide layer.

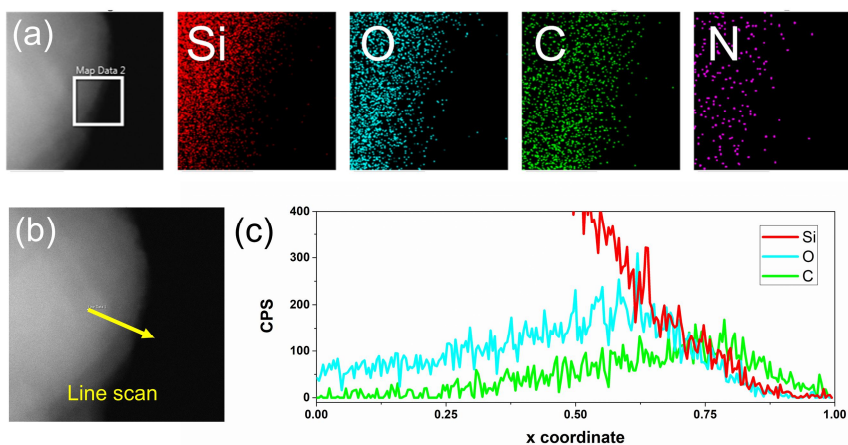


Figure 2.12. (a) EDS analysis images of MWpSi-EG with the element mapping of silicon, oxygen, carbon and nitrogen. (b) The EDS line scan region and the direction. (c) The EDS line scan profiles for silicon, oxygen and carbon.

As a cross reference, the EDS line scan profile shows that the silicon peak and the oxygen peak overlap around the 0.6 position, which corresponds to the SiO_x layer (**Fig. 2.12**). Notably, the carbon peak is located at higher x-coordinate than the silicon and oxygen peak. Along with the HR-TEM image, this proves that the silicon nanoparticle is carbon-coated. If polydopamine was not carbonized properly, the area of mapped oxygen and carbon should have the same size in EDS images and oxygen should be present at the same x-coordinates as carbon in the line scan profile, since polydopamine has oxygen in its molecular structure. Thus, this data proves that polydopamine was properly carbonized during the microwave irradiation. In addition, because the carbonization of polydopamine results in N-doped carbon, nitrogen was also mapped. The area of nitrogen mapped is very similar to the area of carbon, which means that the carbon layer is N-doped.

In order to examine properties of carbon, Raman spectroscopy was conducted. **Figure 2.13a-b** show a clear D and G band around 1360 cm⁻¹ and 1605 cm⁻¹ for all 6 samples (Si-EG, HTSi-

EG, MWSi-EG, pSi-EG, HTPSi-EG and MWpSi-EG), respectively. I_D/I_G ratios for Si-EG, HTSi-EG are 1.27, 0.97 and 0.94, respectively. During anodic exfoliation, EG is functionalized and gets defects in its graphitic structure [32-34]. EG is reduced and becomes more graphitic by heat treatment or microwave irradiation. Interestingly, I_D/I_G ratio of MWSi-EG is lower than the thermally reduced HTSi-EG [42]. This means that MWSi-EG is more graphitic than HTSi-EG, which might be due to the reduction temperature. As I discussed above, since the reduction temperature for MWSi-EG might be higher than that for Si-EG, the I_D/I_G ratio of MWSi-EG is lower than that of HTSi-EG [42]. For polydopamine-coated samples, I_D/I_G ratios of pSi-EG, HTPSi-EG and MWpSi-EG are 0.96, 0.91 and 0.84. Because polydopamine itself exhibits D and G bands just like carbon [43], the I_D/I_G ratios for the above samples are from the combination of graphene, polydopamine or carbonized polydopamine. Thus I_D/I_G ratio of pSi-EG is different from Si-EG. Similar to non-coated samples, I_D/I_G ratio of MWpSi-EG is lower than HTPSi-EG for the same reason. The crystal structure was investigated by X-ray

diffraction (XRD) and displayed in **Figure 2.13c** for pSi-EG, HTpSi-EG and MWpSi-EG. All samples clearly display the crystal lattices of silicon at 28° , 47° , 56° , 69° and 76° which correspond to (111), (220), (311), (400) and (331) reflections of silicon crystal, respectively. (JCPDS card no. 27-1402). For pSi-EG, the broad peak around 24° is assigned to the (002) reflection of graphene. For HTpSi-EG and MWpSi-EG, sharp peaks at 26° are observed, which correspond to the (002) reflection of graphite. After reducing graphene, the peak of the (002) reflection became sharp and shifted to 26° due to the restacking of graphene. Interestingly, the peak at 26° of MWpSi-EG is less sharp than that of HTpSi-EG. This can be attributed to the violent fuming I discussed above. Since the reaction time is so short, vapor evolution from graphene expands the gap between graphene nanosheets [32] and the graphene restacking was suppressed. No peak corresponding to carbonized polydopamine was observed. Since the carbon layer is very thin (2 - 3 nm), the peak might be too low compared to the background noise. In **Figure 2.14**, a weight percent of carbon content was measured by thermal

gravimetric analysis (TGA). The weight loss was calculated with a baseline of bare silicon nanoparticles since the oxidation increases the weight of silicon. The weight percent of carbon content in MWSi-EG and MWpSi-EG are 28.5 % and 34.2 %, respectively. In addition, the weight percent of polydopamine is 7.7 %. **Figure 2.15** shows XPS spectra of EG, pSi-EG, HTpSi-EG and MWpSi-EG. C1s spectra were deconvoluted up to four peaks, C=C/C-C, C-N, C-O and O-C=O peak. Every sample shows a clear C=C/C-C peak near 284.5 eV. EG displays relatively lower peak intensity of C-O at 286.4 eV compared to standard GO synthesized by Hummer's method [20, 44, 45], which means that Sp² domain of EG is preserved better than that of GO. Thus, I think that EG can absorb microwave better than GO so the mild reduction step is not necessary to give the efficient microwave energy conversion. pSi-EG, HTpSi-EG and MWpSi-EG exhibit C-N peak near 285.3 eV, which comes from polydopamine or carbonized polydopamine. The C-O peak intensity of HTpSi-EG is much lower than that of pSi-EG, which means that EG was reduced and recovered its Sp² domains. Like

HTpSi-EG, MWpSi-EG shows similar result, which proves that microwave irradiation successfully reduced EG. The O-C=O peak near 288.8 eV disappears after reduction. In order to examine nitrogen doping, N1s spectra was also obtained (**Figure 2.15e-f**). N1s spectra were deconvoluted into two peaks, pyrrolic N and pyridinic N. Both HTpSi-EG and MWpSi-EG clearly show pyrrolic N and pyridinic N at 400.1 eV and 398.2 eV, respectively. Therefore, I can conclude that HTpSi-EG and MWpSi-EG were N-doped. Interestingly, the intensity of pyridinic N of MWpSi-EG is lower than that of HTpSi-EG due to the reaction time. Since the microwave treatment is too rapid, many nitrogen atoms might not have enough time to arrange as pyridinic N.

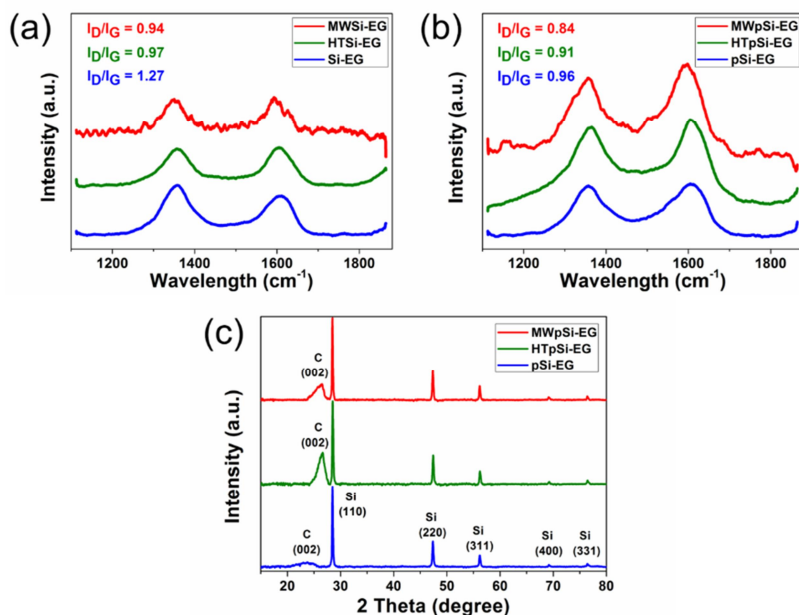


Figure 2.13. Raman spectra of (a) Si-EG, HTSi-EG, MWSi-EG, (b) pSi-EG, HTpSi-EG and MWpSi-EG. (c) XRD patterns of pSi-EG, HTSi-EG and MWpSi-EG.

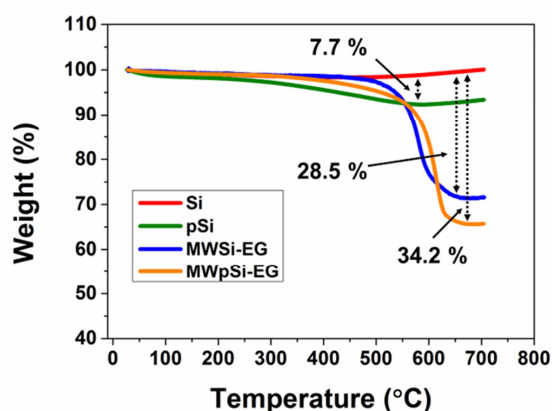


Figure 2.14. TGA data of Si, pSi, MWSi-EG and MWpSi-EG.

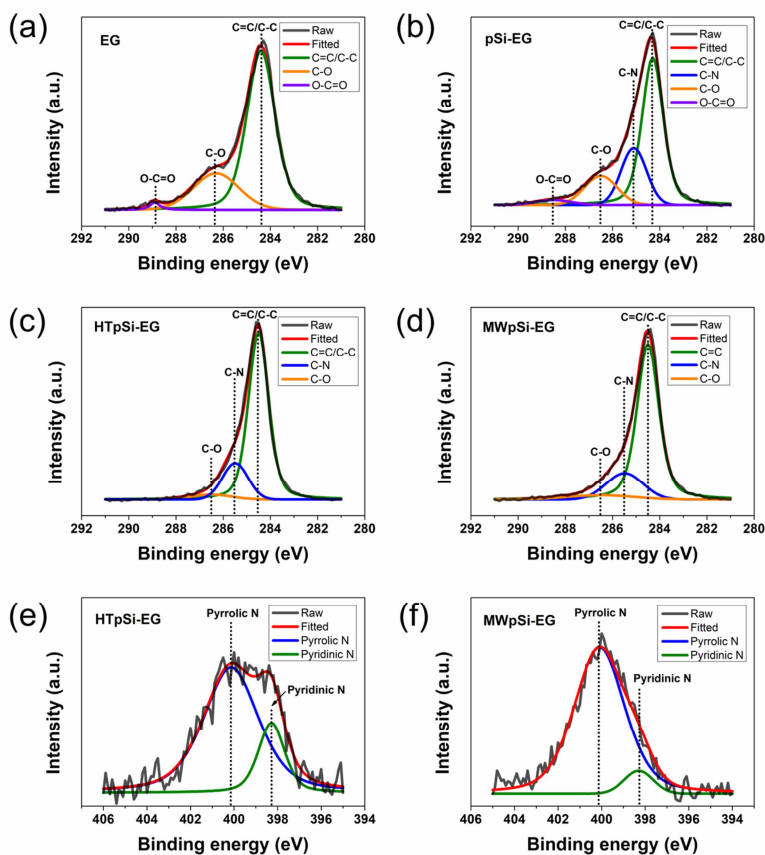


Figure 2.15. C1s XPS spectra of (a) EG, (b) pSi-EG, (c) HTPSi-EG and (d) MWpSi-EG. N1s XPS spectra of (e) HTPSi-EG and (f) MWpSi-EG.

Figure 2.16 shows galvanostatic charge/discharge profiles of Si-EG, pSi-EG, MWSi-EG and MWpSi-EG between 0.01 - 2.0 V (vs. Li/Li⁺). At the initial cycle with a current density of 0.1 A g⁻¹, Si-EG, pSi-EG, MWSi-EG and MWpSi-EG exhibit discharge specific capacities of 1627, 1606, 1890 and 2314 mAh g⁻¹, respectively. The initial coulombic efficiency of each sample are 51.2 %, 56.8 %, 68.7 % and 75.4 %, respectively. After microwave irradiation, initial capacity loss decreased. This may be attributed to the removal of oxygen moiety on graphene, which suppresses the side reaction with the electrolyte. Moreover, in the galvanostatic discharge profiles, the voltage of Si-EG and pSi-EG descended more slowly in the specific capacity region between 0 and 500 mAh g⁻¹ than MWSi-EG and MWpSi-EG. I suppose that this is because of the side reaction. Thus, I conclude that MWSi-EG and MWpSi-EG were successfully reduced by microwave irradiation. Interestingly, MWpSi-EG shows higher specific capacity than MWSi-EG. I think that this is owing to N-doped carbon coating from polydopamine. It enhances the electric

conductivity by providing the efficient electron path along with graphene. After 5 cycles, initially at 0.1 A g^{-1} and subsequently at 0.4 A g^{-1} , Si-EG, pSi-EG, MWSi-EG and MWpSi-EG exhibit discharge specific capacities of 485, 496, 1385 and 1602 mAh g^{-1} , respectively.

Figure 2.17a-b show cyclic voltammogram of MWSi-EG and MWpSi-EG between 0.01 - 2.0 V (vs. Li/Li^+) for 5 cycles with a scan rate of 0.1 mV s^{-1} . At the initial cycle, both samples show two cathodic peaks around 0.2 V and 1.1 V. The cathodic peak around 0.2 V corresponds to the silicon-lithium alloying reaction and the peak around 1.1 V might be solid electrolyte interphase (SEI) layer formation. Two anodic peaks around 0.36 V and 0.52 V are owing to silicon-lithium dealloying reaction. For both samples, the intensity of current peaks gradually increases throughout the subsequent cycles. I think that this is because of the activation process [46-48]. In order to evaluate the rate performance of MWSi-EG and MWpSi-EG, both samples were galvanostatically cycled with various current densities which are 0.1, 0.4, 0.8, 1.2, 1.6 and 2 A g^{-1} (**Figure 2.17c**). MWSi-EG

exhibits the discharge specific capacities of 1800, 1180, 947, 666, 492 and 370 mAh g⁻¹ at 0.1, 0.4, 0.8, 1.2, 1.6 and 2 A g⁻¹, respectively. In the same manner, MWpSi-EG shows the discharge specific capacities of 2318, 1608, 1367, 1057, 854 and 709 mAh g⁻¹. MWpSi-EG exhibits better rate performance than MWSi-EG. This may be attributed to the N-doped carbon coating on silicon nanoparticles. N-doped carbon coating enhances the electric conductivity so that the contact resistance between silicon nanoparticles and of silicon-graphene interphase decreases and suppresses electrode polarization. To show the effect of reduction and carbonization, Si-EG and pSi-EG were also evaluated (**Figure 2.18**). Both samples exhibit very bad performance due to poor electric conductivity. **Figure 2.17d** shows cycling performance of MWSi-EG and MWpSi-EG. MWSi-EG exhibits a discharge specific capacity of 667 mAh g⁻¹ after 50 cycles at 0.4 A g⁻¹ and a capacity retention of 59.5 %. On the other hand, MWpSi-EG shows a discharge specific capacity of 1370 mAh g⁻¹ with a capacity retention of 91.1 %. I think that the enhanced cycling performance of MWpSi-EG is owing to N-doped carbon coating.

Silicon is pulverized due to the mechanical stress caused by volume expansion (up to $\sim 300\%$) and contraction during lithiation/delithiation [49,50]. It causes a continuous SEI layer formation and a loss of electric contact, which results in bad cycling performance. Moreover, it is known that the cycling performance can be enhanced by reducing the size of silicon particles because the smaller particles experience the lower mechanical stress during lithiation/delithiation [51,52]. Therefore, the cycling performance of MWpSi-EG is enhanced by N-doped carbon coating that suppresses the volume expansion of silicon nanoparticles and prevents silicon nanoparticles from sintering during microwave irradiation. Furthermore, MWSi-EG which does not have a N-doped carbon layer shows poor cycling performance because the sintered silicon nanoparticles experience higher mechanical stress, resulting in fast capacity degradation. For long-term cycling performance evaluation, MWpSi-EG was electrochemically evaluated for 200 cycles at 1.0 A g^{-1} (**Figure 2.17e**). After 200 cycles, it exhibits a discharge capacity of 662 mAh g^{-1} with a coulombic efficiency of 98.1% . The capacity

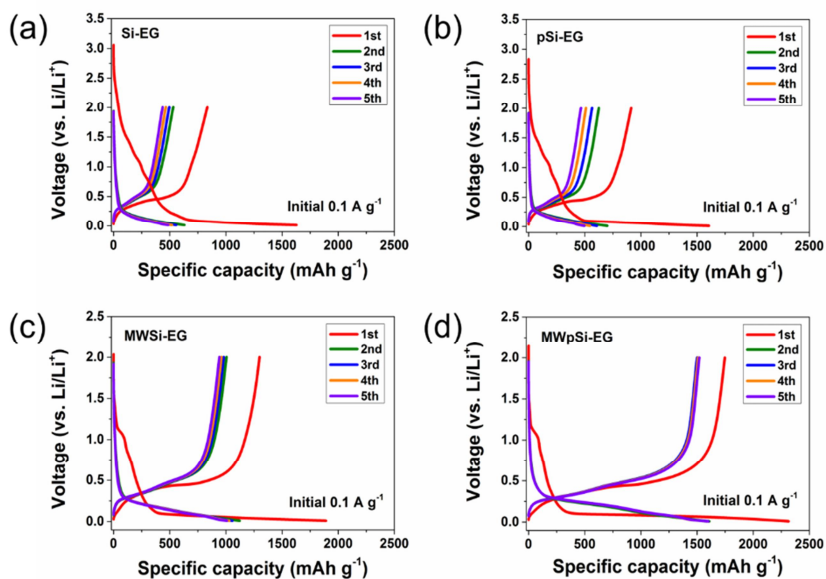
retention is 62.7 %. For further study, a MWpSi-EG electrode was examined by SEM after 120 cycles at 1.0 A g^{-1} (**Figure 2.20**). Silicon nanoparticles maintained its spherical morphology, which proves that the silicon nanoparticles were not pulverized during cycling.

To emphasize the benefit of reduction and carbonization via microwave irradiation, the thermally reduced and carbonized HTpSi-EG sample was also electrochemically tested (**Figure 2.18a**). HTpSi-EG exhibits a very similar rate performance with MWpSi-EG as expected. However, MWpSi-EG shows slightly better performance. This can be explained by electrochemical impedance spectroscopy (EIS) that I will discuss later. If polydopamine was not carbonized properly or graphene was not reduced, the electrochemical performance should be very different. Thus, along with material characterization data, I conclude that the microwave irradiation successfully carbonized polydopamine and reduced graphene. For deeper electrochemical evaluation, Electrochemical impedance spectroscopy (EIS) was performed (**Figure 2.18b**). All EIS test were done with electrodes

cycled in the rate performance. All samples show clear semi-circles related to the contact resistance. Semi-circles become larger in the sequence of MWpSi-EG, HTpSi-EG, MWSi-EG, pSi-EG and Si-EG. This means that MWpSi-EG has the lowest contact resistance even compared to HTpSi-EG due to the graphitic level of carbon. As Raman spectra already showed, microwave-irradiated samples have lower I_D/I_G than heat-treated samples. Since carbon that is more graphitic has higher electric conductivity, the contact resistance in MWpSi-EG is lower than HTpSi-EG. Interestingly, even though the contact resistance is very different between MWpSi-EG and HTpSi-EG, the rate performance is not that different. EIS data can be affected by many variables such as electrode thickness and mass [65]. However, I tried to match the mass (close to 0.8 mg) and the thickness (close to 25 μm) of the electrode as much as possible. In addition, the contact resistance is related to charge transfer, not mass transfer. Therefore, I think that such difference in the contact resistance might be unable to affect the rate performance considerably, since the rate performance is a summarized result

from both charge transfer and mass transfer. In addition, to give a better understanding of the electrochemical performance, the physical properties (mass, thickness, density and electrical conductivity) of MWSi-EG and MWpSi-EG are provided(**Table 2.2**).

Figure 2.16. Galvanostatic charge/discharge profiles of (a) Si-EG, (b) pSi-EG, (c) MWSi-EG and (d) MWpSi-EG. The initial cycle for each sample is at 0.1 A g^{-1} . The subsequent cycles are at 0.4 A g^{-1} .



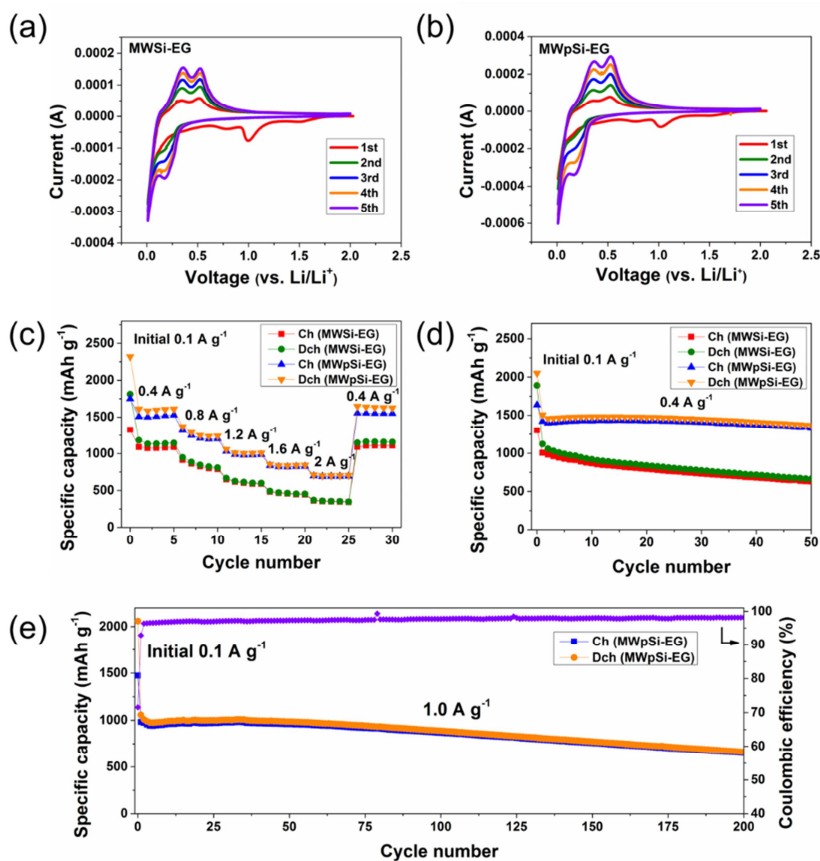


Figure 2.17. Cyclic voltammogram of (a) MWSi-EG and (b) MWpSi-EG for first 5 cycles with a scan rate of 10 mV s^{-1} in a voltage window between 0.01 - 2.0 V (vs. Li/Li^+). (c) rate performance of MWSi-EG and MWpSi-EG with various current densities. (d) Cycling performance of MWSi-EG and MWpSi-EG for 50 cycles. (e) long-term cycling performance of MWpSi-EG with a current density of 1.0 A g^{-1} except the initial cycle.

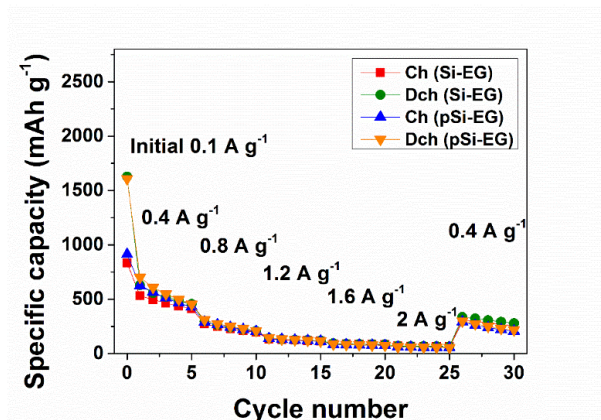
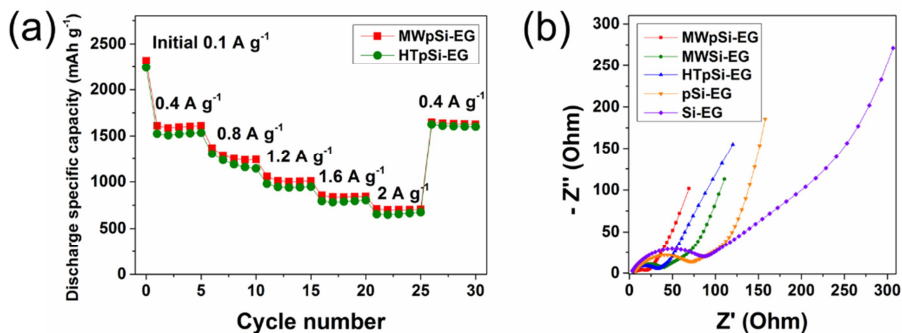


Figure 2.18. Rate performance of Si-EG and pSi-EG at various



current densities.

Figure 2.19. (a) rate performance of MWpSi-EG and HTpSi-EG at various current densities. (b) Nyquist plot of MWpSi-EG, MWSi-EG, HTpSi-EG, pSi-EG and Si-EG.

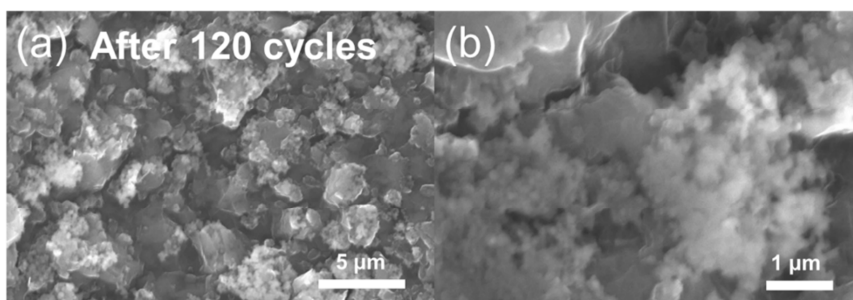


Figure 2.20. SEM images of MWpSi-EG after 120 cycles at 1.0 A g⁻¹ with (a) low and (b) high magnification.

Table 2.1. Physical properties of MWSi-EG and MWpSi-EG.

	MWSi-EG	MWpSi-EG
Mass (mg)	0.803±0.023	0.793±0.005
Thickness (μm)	27.83±0.76	25.16±0.28
Density (kg m⁻³)	303.7±12.0	331.8±4.2
Electrical conductivity (S cm⁻¹)	13.17±0.25	19.83±0.38

2.4. Conclusion

Microwave was used to reduce the partially oxidized EG and carbon coat the silicon nanoparticles. I showed that anodically prepared EG is a good microwave susceptor to generate heat in few seconds using a commercial microwave. Using EG saves time and energy since it does not need a mild reduction step, unlike GO which requires thermal treatment or chemical treatment. Few seconds of microwave irradiation was sufficient to successfully reduced graphene and carbonized the polydopamine coating. The as-prepared N-doped carbon-coated silicon-graphene film exhibits a reversible specific capacity of 1744 mAh g^{-1} at 0.1 A g^{-1} . At a high current density of 2.0 A g^{-1} , it shows a reversible capacity of 708 mAh g^{-1} . After 200 cycles at 1.0 A g^{-1} , it exhibits a reversible capacity of 662 mAh g^{-1} with 98.1 % coulombic efficiency. This method has the potential to be utilized as a general approach to synthesize various exfoliated graphite nanocomposites or to carbonize many carbon precursors within a few seconds. Therefore, microwave irradiation utilizing anodically exfoliated graphite has great potential for various applications including

energy storage devices.

2.5. Reference

- [1] Raccichini, R.; Varzi, A.; Passerini, S.; Scrosati, B. *Nat. Mater.*, **2015**, 14, 271-279.
- [2] Paek, S.-M.; Yoo, E.; Honma, I. *Nano Lett.*, **2009**, 9, 72-75.
- [3] Wang, H.; Cui, L.-F.; Yang, Y.; Casalongue, H. S.; Robinson, J. T.; Liang, Y.; Cui, Y.; Dai, H.; *J. Am. Chem. Soc.*, **2010**, 132, 13978-13980.
- [4] Wu, Z.-S.; Ren, W.; Wen, L.; Gao, L.; Zhao, J.; Chen, Z.; Zhou, G.; Li, F.; Cheng, H.-M.; *ACS Nano*, **2010**, 4, 3187-3194.
- [5] Wang, H.; Casalongue, H. S.; Liang, Y.; Dai, H.; *J. Am. Chem. Soc.*, **2010**, 132, 7472-7477.
- [6] Zhou, G.; Wang, D.-W.; Li, F.; Zhang, L.; Li, N. Wu, Z.-S.; Wen, L.; Lu, G. Q.; Cheng, H.-M.; *Chem. Mater.*, **2010**, 22, 5306-5313.
- [7] Chen, Y.; Li, Y.; Wang, Y.; Fu, K.; Danner, V. A.; Dai, J.; Lacey, S. D.; Yao, Y.; Hu, L. *Nano Lett.*, **2016**, 16, 5553-5558.
- [8] Zhu, P.; Nair, A. S.; Shengjie, P.; Shengyuan, Y.; Ramakrishna, S. *ACS Appl. Mater. Interfaces*, **2012**, 4, 581-585.
- [9] Kim, H.-i.; Moon, G.-h.; Monllor-Satoca, D.; Park, Y.; Choi, W. *J. Phys. Chem. C*, **2012**, 116, 1535-1543.
- [10] Bajpai, R.; Roy, S.; Kumar, P.; Bajpai, P.; Kulshrestha, N.; Rafiee, J.; Koratkar, N.; Misra, D. S. *ACS Appl. Mater.*

- Interfaces*, **2011**, 3, 3884-3889.
- [11] Kang, X.; Wang, J.; Wu, H.; Aksay, I. A.; Liu, J.; Lin, Y. *Biosens Bioelectron*, **2009**, 25, 901-905.
 - [12] Mao, S.; Lu, G.; Yu, K.; Bo, Z.; Chen, J. *Adv. Mater.*, **2010**, 22, 3521-3526.
 - [13] Lightcap, I. V.; Kosel, T. H.; Kamat, P. V. *Nano Lett.*, **2010**, 10, 577-583.
 - [14] Liang, Y. ; Li, Y.; Wang, H.; Zhou, J.; Wang, J.; Regier, T.; Dai, H. *Nat. Mater.*, **2011**, 10, 780-786.
 - [15] Li, Y.; Wang, H.; Xie, L.;Liang, Y.; Hong, G.; Dai, H. *J. Am. Chem. Soc.*, **2011**, 133, 7296-7299.
 - [16] Li, J. S.; Wang, Y.; Liu, C. H.; Li, S. L.; Wang, Y. G.; Dong, L. Z.; Dai, Z. H.; Li, Y. F.; Lan, Y. Q. *Nat. Commun.*, **2016**, 7, 11204.
 - [17] Peng, S.; Han, X.; Li, L.; Zhu, Z.; Cheng, F.; Srinivansan, M.; Adams, S.; Ramakrishna, S. *Small*, **2016**, 12, 1359-1368.
 - [18] Lim, E.; Jo, C.; Kim, M. S.; Kim, M.-H.; Chun, J.; Kim, H.; Park, J.; Roh, K. C.; Kang, K.; Yoon, S.; Lee, J. *Adv. Funct. Mater.*, **2016**, 26, 3711-3719.
 - [19] Bridewell, V. L.; Karwacki, C. J.; Kamat, P. V. *ACS Sensors*, **2016**, 1, 1203-1207.
 - [20] Pei, S.; Cheng, H.-M. *Carbon*, 2012, **50**, 3210-3228.
 - [21] Zhu, Y.; Murali, S.; Stoller, M. D.; Velamakanni, A.; Piner, R. D.; Ruoff, R. S. *Carbon*, **2010**, 48, 2118-2122.
 - [22] Chen, W.; Yan, L.; Bangal, P. R. *Carbon*, 2010, **48**, 1146-1152.
 - [23] Hu, H.; Zhao, Z.; Zhou, Q.; Gogotsi, Y.; Qiu, J. *Carbon*, **2012**, 50, 3267-3273.

- [24] Liu, N.; Wang, X.; Xu, W.; Hu, H.; Liang, J.; Qiu, J. *Fuel*, **2014**, 119, 163-169.
- [25] Lin, Y.; Baggett, D. W.; Kim, J. W.; Siochi, E. J.; Connell, J. W. *ACS Appl. Mater. Interfaces*, **2011**, 3, 1652-1664.
- [26] Hazarika, A.; Deka, B. K.; Kim, D.; Kong, K.; Park, Y.-B.; Park, H. W. *Sci. Rep.*, **2017**, 7, 40386.
- [27] Yang, M.; Lee, K. G.; Lee, S. J.; Lee, S. B.; Han, Y. K.; Choi, B. G. *ACS Appl. Mater. Interfaces*, **2015**, 7, 22364-22371.
- [28] Kannan, R.; Kim, A. R.; Nahm, K. S.; Lee, H. K.; Yoo, D. *J. Chem. Commun.*, **2014**, 50, 14623-14626.
- [29] Voiry, D.; Yang, J.; Kupferberg, J.; Fullon, R.; Lee, C.; Jeong, H. Y.; Shin, H. S.; Chhowalla, M. *Science*, **2016**, 353, 1413-1416.
- [30] Xia, Z. Y.; Wei, D.; Anitowska, E.; Bellani, V.; Ortolani, L.; Morandi, V.; Gazzano, M.; Zanelli, A.; Borini, S.; Palermo, V. *Carbon*, **2015**, 84, 254-262.
- [31] Li, L.; Li, X.; Du, M.; Guo, Y.; Li, Y.; Li, H.; Yang, Y.; Alam, F. E.; Lin, C.-T.; Fang, Y. *Chem. Mater.*, **2016**, 28, 3360-3366.
- [32] Yang, S.; Bruller, S.; Wu, Z. S.; Liu, Z.; Parvez, K.; Dong, R.; Richard, F.; Samori, P.; Feng, X.; Mullen, K.; *J. Am. Chem. Soc.*, **2015**, 137, 13927-13932.
- [33] Ambrosi, A.; Pumera, M. *Chem. Eur. J.*, **2016**, 22, 153-159.
- [34] Kim, K. H.; Cho, K. M.; Kim, D. W.; Kim, S. J.; Choi, J.; Bae, S. J.; Park, S.; Jung, H. T. *ACS Appl. Mater. Interfaces*, **2016**, 8, 5556-5562.
- [35] Kang, S.; Choi, H.; Lee, S. B.; Park, J. B.; Park, S.; Lee,

- Y.; Hong, B. H.; *2D Mater.*, **2017**, 4, 025037.
- [36] Wang, C.; Han, X.; Xu, P.; Zhang, X.; Du, Y.; Hu, S.; Wang, J.; Wang, X. *Appl. Phys. Lett.*, **2011**, 98, 072906.
- [37] Drahi, E.; Gupta, A.; Blayac, S.; Saunier, S.; Benaben, P. *Phys. Status Solidi A*, **2014**, 211, 1301-1307.
- [38] Oh, J.; Lee, J.; Hwang, T.; Kim, J. M.; Seoung, K.-d.; Piao, Y. *Electrochim. Acta*, **2017**, 231, 85-93.
- [39] Asoro, M. A.; Kovar, D.; Ferreira, P. J.; *Chem. Commun.*, **2014**, 50, 4835-4838.
- [40] Ryu, S.; Chou, J. B.; Lee, K.; Lee, D.; Hong, S. H.; Zhao, R.; Lee, H.; Kim, S. G. *Adv. Mater.*, **2015**, 27, 3250-3255.
- [41] Xin, G.; Sun, H.; Hu, T.; Fard, H. R.; Sun, X.; Koratkar, N.; Borca-Tasciuc, T.; Lian, J. *Adv. Mater.*, **2014**, 26, 4521-4526.
- [42] Li, H.; Aulin, Y. V.; Frazer, L.; Borguet, E.; Kakodkar, R.; Feser, J.; Chen, Y.; An, K.; Dikin, D. A.; Ren, F. *ACS Appl. Mater. Interfaces*, **2017**, 9, 6655-6660.
- [43] Stankovich, S.; Dikin, D. A.; Piner, R. D.; Kohlhaas, K. A.; Kleinhammes, A.; Jia, Y.; Wu, Y.; Nguyen, S. T.; Ruoff, R. S. *Carbon*, **2007**, 45, 1558-1565.
- [44] Schniepp, H. C.; Li, J.-L.; McAllister, M. J.; Sai, H.; Herrera-Alonso, M.; Adamson, D. H.; Prud'homme, R. K.; Car, R.; Saville, D. A.; Aksay, I. A. *J. Phy. Chem. B*, **2006**, 110, 8535-8539.
- [45] Chan, C. K.; Peng, H.; Liu, G.; McIlwrath, K.; Zhang, X. F.; Huggins, R. A.; Cui, Y. *Nat. Nanotechnol.*, **2008**, 3, 31-35.
- [46] Chang, J.; Huang, X.; Zhou, G.; Cui, S.; Hallac, P. B.; Jiang, J.; Hurley, P. T.; Chen, J. *Adv. Mater.*, **2014**, 26,

758-764.

- [47] Green, M.; Fielder, E.; Scrosati, B. Wachtler, M.; Moreno, J. S. *Electrochem. Solid-State Lett.*, **2003**, 6, A75.
- [48] Ryu, J. H.; Kim, J. W.; Sung, Y.-E.; Oh, S. M. *Electrochem. Solid-State Lett.*, **2004**, 7, A306.
- [49] Oumellal, Y.; Delpuech, N.; Mazouzi, D.; Dupré, N.; Gaubicher, J.; Moreau, P.; Soudan, P.; Lestriez, B.; Guyomard, D. *J. Mater. Chem.*, **2011**, 21, 6201.
- [50] Yang, J.; Winter, M.; Besenhard, J. O. *Solid State Ionics*, **1996**, 90, 281.
- [51] Kim, H.; Seo, M.; Park, M. H.; Cho, J.; *Angew. Chem. Int. Ed. Engl.*, **2010**, 49, 2146-2149.
- [52] Ogihara, N.; Itou, Y.; Sasaki, T.; Takeuchi, Y. *J. Phys. Chem. C*, **2015**, 119, 4612-4619.

Chapter 3. Facile and Scalable Approach to Develop Electrochemical Unzipping of Multi-walled Carbon Nanotubes to Graphene Nanoribbons

3.1. Introduction

Strips of graphene exhibiting a quasi-one-dimensional morphology, called graphene nanoribbons (GNRs), have attracted considerable attention due to their unique physical properties such as controllable behavior from semi-metallic to semi-conductive, and co-existence of both 1D and 2D structures[1–3]. Further, GNRs have been successfully utilized in a wide range of applications including nanoelectronics[4,5], catalysis[6–8],

battery[9–11], supercapacitor[12,13], and composite materials[14,15] To date, chemical unzipping of multi-walled carbon nanotube (MWCNTs) is the most practical method for large-scale GNR preparation.[16–18] Despite the scalability of the chemical unzipping method, this method introduces safety and environmental issues that are related to the use of strong chemical reagents such as mixture of $\text{H}_2\text{SO}_4/\text{KMnO}_4$ [16] or alkali metals[17]. Several eco-friendly or green synthetic approaches have been developed for producing GNRs but these methods suffer from low scalability and high costs due to high pressure, high temperature, and the use of complicated and/or resource intensive techniques [19–25]. Their utilization is further impeded by the need for precise control over the reaction steps that are associated with the demands of various applicable morphologies. For facile and eco-friendly production, electrochemical approaches have been explored to prepare two-dimensional (2D) materials[26,27]. Most studies on electrochemical preparation of 2D materials involved exfoliation of bulk layered materials[28–30]. Compared to electrochemical exfoliation, electrochemical

unzipping is rarely demonstrated and has not been systematically studied to date [31–33]. Previously reported electrochemical MWCNT unzipping methods involved the anodic oxidation of MWCNTs in diluted sulfuric acids. However, in several previous reports[34–38], the anodic oxidation of MWCNT in diluted acid electrolytes resulted in the destruction of the carbon surface rather than selective unzipping. Another issue with these processes is their limited scalability. In an electrochemical process, MWCNT powders should be fabricated into bulk electrodes to ensure electrical current supply. However, such unzipping has been performed using MWCNT thin films with a low loading mass ($\sim 5 \mu\text{g}$) as an electrode, resulting in low yield and limited scalability (**Table 1.3**)[31,33,39,40]. In addition, anodic oxidation in diluted sulfuric acid involves gas evolution, causing the MWCNT to detach from the electrode during the reaction [41].

Electrochemical approaches involve several operational conditions such as working electrodes, intercalants, and electrolytes. Therefore, regulation of these parameters would be necessary for developing a scalable and reliable electrochemical

unzipping method for MWCNTs. In this study, I developed a novel electrochemical process for a scalable preparation of GNRs. In brief, a MWCNT was attached to a working electrode using an apparatus designed by us. Then, the working electrode was anodically oxidized in concentrated sulfuric acid instead of previously used diluted sulfuric acid. Our designed apparatus enables the use of MWCNT powders (up to 25 mg cm^{-2}) for unzipping without additional additives and has the potential for large-scale production of GNRs once this setup is optimized (**Figure 3.1** and **Figure 3.3**). Concentrated sulfuric acid was chosen as it could drive unzipping through intercalation[17,42]. When MWCNTs become highly intercalated, internal pressure develops, initiating unzipping of the tube as confirmed by *ex-situ* X-ray diffraction technique, Raman scattering spectroscopy, and electrochemical analysis. Moreover, the usage of concentrated sulfuric acid enables the tuning of the C/O ratio and unzipping degree of the GNR product by simply regulating the anodic oxidation time. Further analysis confirmed that the concentration of the electrolyte served as an important factor for electrochemical

unzipping of carbon nanotubes. When MWCNTs are anodically oxidized in diluted electrolytes (concentration less than 15 M), the intercalation-driven unzipping is inhibited and the MWCNTs are subjected to random cleavage of C–C bonds by the radicals generated from the water oxidation or carbon oxidation reactions. GNRs are demonstrated as support for electrocatalytic hydrogen evolution reaction.

3.2. Experimental Method

Preparation of working electrode

MWCNT (length: 5-9 μm , outer diameter: 110-170 nm, Sigma-Aldrich, USA) powder was mounted on a glass fiber filter membrane using vacuum filtration. Then, MWCNT loaded filter membrane was placed in a Jig. MWCNT powder was electrically contacted with a platinum plate, which was then connected with platinum wire (**Figure 3.1.**). MWCNTs with a smaller diameter (S-MWCNTs, length: 20-100 μm , outer diameter: 20 nm, iCNT,

Korea) and MWCNTs with a medium diameter (M-MWCNTs, length: $> 5 \mu\text{m}$, outer diameter: 60-100 nm, Tokyo Chemical Industry, Japan) were unzipped by the same procedure.

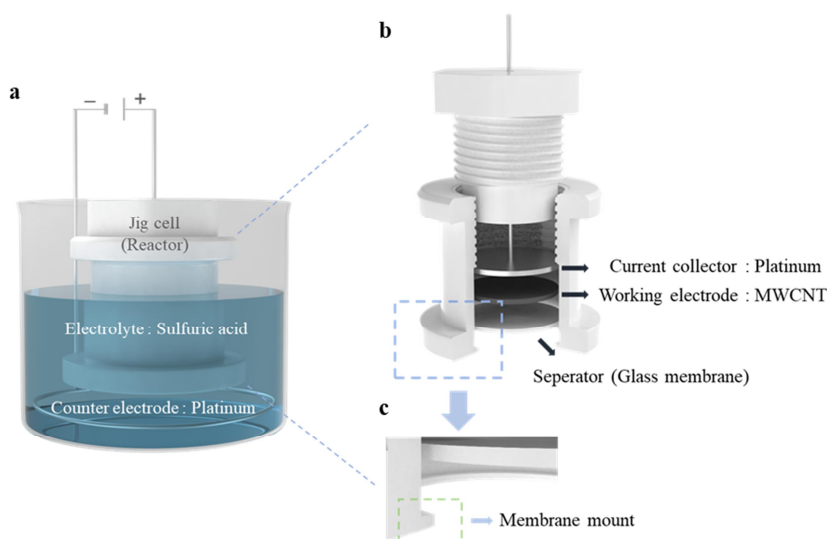


Figure 3.1. Schematic illustration of a home-made Jig setup for electrochemical unzipping of MWCNT. (b) The Jig consists of a cap (screw design), body, current collector (home-made platinum), working electrode (MWCNTs), and separator (glass fiber filter membrane was cut to fit the inside diameter (size: 20 mm) of the reactor). (c) Magnified view of the membrane mount used to support all parts of the reactor. Jig is made of

PTFE because it shows excellent acid resistance in concentrated sulfuric acid. The screw-type cap was designed to make good electrical contact between the current collector and the working electrode.

Electrochemical unzipping of multiwalled Carbon nanotubes (MWCNTs);

The electrochemical unzipping process was carried out in both three-electrode cell and two-electrode configuration (**Figure 3.2**). In a typical procedure for unzipping, concentrated sulfuric acid (> 96 %, Samchun, Korea) was used as an electrolyte. MWCNTs were performed using different diluted sulfuric acids (0.5 M, 10 M, and 15 M) to investigate the effect of H₂O molecule. Constant current 1 mA (0.5 mA cm⁻²) was applied to the Jig by an electrochemical workstation (ZIVE LAB, Korea). The stepwise unzipping was performed at different reaction conditions with the same charging current. For three-electrode configuration, Pt ring and Hg/Hg₂SO₄ (Sat. K₂SO₄) were used as a counter and reference electrode, respectively. For

smaller diameter MWCNT, electrochemical reactions were performed at 0.5 M and 18 M H_2SO_4 electrolytes, respectively.

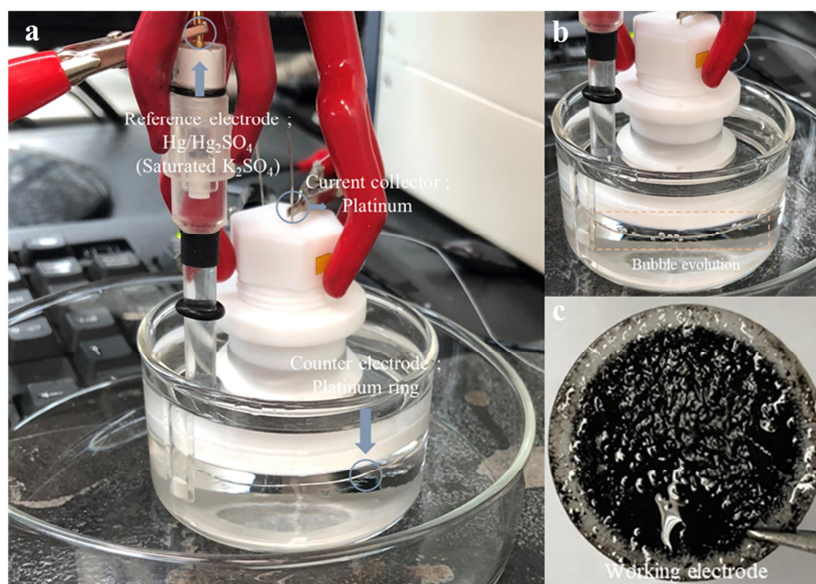


Figure 3.2. (a) Photograph of the three-electrode cell used to perform the electrochemical reaction in concentrated sulfuric acid. (b) Hydrogen evolution (dashed-line box) was observed on the Pt ring (counter electrode) during galvanostatic charging at a current density of 0.5 mA cm^{-2} . (c) Photograph showing the MWCNTs after the unzipping process.

Washing procedure

After unzipping the MWCNTs at different charging status, the products were collected through a PTFE filter membrane (pore size 0.2 μm , HYUNDAI Mirco, Korea) by vacuum filtration and washed with deionized water for several times.

Measurements of K-ion aqueous supercapacitor;

A typical three-electrode method was used to assess the electrochemical performance, consisting of glassy carbon as a working electrode, platinum wire, and Hg/HgO (1 M NaOH) as a counter electrode and a reference electrode, respectively. Typically, 10 mg of the sample was dispersed in 10 mL ethanol-water solution ($v/v = 1:1$) by sonication for 30 min. 5 μL of the above solution was dropped on a glassy carbon electrode. Cyclic voltammetry (CV), galvanostatic charge/discharge (GCD), and electrochemical impedance spectroscopy (EIS) measurements were carried out by an electrochemical workstation (CHI 660E

potentiostat) in 6 M KOH electrolyte. The specific capacitance from the GCD curve, C_m (F g⁻¹), was calculated according to the following equation S1: $C_m =$

$$I \times \Delta t / m \times \Delta V$$

, where I is the constant discharge current (A), Δt is the discharging time, m is the mass of active material, and ΔV is the potential window during the discharge process (excluding the IR drop).

Measurements of Li-ion organic supercapacitor;

The slurry to prepare the electrodes was composed of 90 wt% of active materials (pristine MWCNT and product a) and 10 wt% of the binder (polyvinylidene fluoride, PVDF) and NMP as processing solvent. The well-mixed slurry was coated on a copper foil and dried 80°C overnight. Coin-type (CR2016) cells were fabricated in an Ar-filled glove box with a Li metal as a reference

and counter electrode Celgard 2400 as a separator. 1.3 M LiPF_6 in ethylene carbonate (EC) and diethyl carbonate (DEC) (v/v = 3:7) with 10 vol % fluoroethylene carbonate (FEC) additive (PANAX) was used as an electrolyte. Galvanostatic charge/discharge and cyclic voltammetry curves were measured using a WBCS3000S cycler (WonATech, Korea) at a potential window from 0.1 to 2.5 V (vs. Li/Li^+).

Measurements of hydrogen evolution reaction (HER);

The electrochemical performance was investigated using an electrochemical workstation (Metrohm Autolab workstation, PGSTAT 302N) in a standard three-electrode system. The glassy carbon rotating disk electrode (RDE) modified with samples, graphite rod, and Ag/AgCl (Sat. KCl) were used as the working electrode, counter electrode and reference electrode, respectively. The rotation speed of RDE was 2400 rpm. 5 mg of the sample for testing was dispersed in a mixture of deionized water (950 μL),

followed by the addition of 5 wt% Nafion (50 μL , Aldrich). A homogeneous slurry was obtained by sonicating for 30 min. The dispersion (10 μL) was drop-casted on a glassy carbon electrode (GCE) and then dried using an infrared lamp. The mass loading of catalysts was 0.21 mg cm^{-2} . All measurements were calculated respect to reversible hydrogen electrode according to the Nernst equation S2:

$$E (\text{V vs RHE}) = E (\text{V vs Ag/AgCl}) + 0.197 + 0.0591 \times \text{pH}$$

. The linear scan voltammetry (LSV) curve was measured at a scan rate of 2 mV s^{-1} in 1 M KOH. Double-layer capacitance was evaluated under a potential window of 0.2 to 0.3 (V vs. RHE) with various scan rates from 20 mV s^{-1} to 80 mV s^{-1} using CV in 1 M KOH. All LSV data were corrected with iR losses during the measurements.

Material characterizations

The morphology analysis of the samples was carried out a field-emission scanning electron microscope (FE-SEM, Hitachi S-4800) and a high-resolution transmission electron microscope (HR-TEM, JEOL JEM-2010F) equipped with a Cs-corrected STEM and an energy dispersive X-ray (EDX) spectrometer. Electron energy loss spectroscopy (EELS) was performed using EELS spectrometer (GATAN, GIF Tridiem). The materials for SEM were prepared by drop-coating from ethanol suspensions (0.2 mg mL^{-1}) onto Si/SiO₂ substrate. The X-ray photoelectron spectroscopy (XPS) measurements were obtained using an AXIS-His spectrometer at a base pressure of 1×10^{-8} mbar, and XPS spectra were fitted using a Casa XPS software. UV-vis absorption spectra were measured using a Thermo Fisher Scientific Evolution 60 spectrophotometer. Fourier transform infrared spectra (FT-IR) were recorded using a Nicolet 6700 spectrometer (Thermo Fisher Scientific). Inductively coupled plasma mass spectrometry (ICP-MS, NexION 350D) were assessed for Fe isotope measurement. Thermogravimetric analysis (TGA, TGA/DSC 1) were obtained using a thermal

analyzer at a ramp rate of $10\text{ }^{\circ}\text{C min}^{-1}$ under N_2 and Air atmosphere, respectively. N_2 adsorption/desorption isotherms were performed using an adsorption analyzer (BELSORP-mini II). The sheet resistance ($\Omega\text{ sq}^{-1}$) of the samples was measured by using a four-point probe measurement (Advanced Instrument Technology CMT-100S). To investigate the sheet resistance, A slurry composed of 90 wt% of materials (pristine MWCNT and product a) and 10 wt% of binder (polyvinylidene fluoride, PVDF). Then, the slurry was spread on to the PET film (thickness: $100\text{ }\mu\text{m}$) using a doctor blade and dried at $60\text{ }^{\circ}\text{C}$ overnight. The thickness of the slurry ($43\text{ }\mu\text{m}$) was measured by using a digital Vernier caliper. Samples for ICP-MS analysis were prepared according to the following procedure. To obtain the sample 1, 15 mg of the MWCNT powder was dispersed in concentrated sulfuric acid (30 mL) for 2 days and the mixture was separated from solution by centrifugation (10 min at 6000 rpm). Then, the supernatant was diluted by deionized water ($v/v = 1:100$). For comparison, the sample 2 was prepared by galvanostatic charging

at a current density 0.5 mA cm^{-2} for 0.5 h using three-electrode cell. Rest of the procedures was same as described above.

Ex-situ Optical microscope, Raman spectroscopy and XRD measurements;

To observe intercalation, the samples with different charging status (*i*, *a*, *b*) were investigated by Optical microscope (OLYMPUS BX51), ex-situ Raman spectroscopy (LabRAM HV Evolution with an excitation laser wavelength of 532 nm), and X-ray diffraction (XRD, Bruker D8-advance with a Cu-K α source operating at 40 kV and 40 mA at a scan rate of 3° min^{-1}). Samples with concentrated H₂SO₄ were taken from the Jig cell, then samples on the PTFE filter membrane were scraped off using a home-made glass knife. Next, scrapped samples were placed between a glass holder and the coverslip (the coverslip was changed to Kapton film in the XRD analysis only). The optical image is obtained via transmitted light mode.)

3.3. Results and Discussion

3.3.1. Preparation of GNRs

As shown in **Figure 3.1** and **3.3a**, MWCNT electrode was first attached to a working electrode by vacuum filtration of MWCNT suspension on a glass fiber membrane mounted in our designed apparatus. The mounted glass fiber membrane served as both a holder and a separator for the anodic oxidation of MWCNT. Next, platinum current collector was placed on the filtered MWCNTs. Subsequently, MWCNTs were pressured together by a screw thread to ensure electrical contact between the MWCNTs and platinum current collector. The detailed process to form a working electrode is demonstrated in Supporting Experimental Methods. No binder or pelletizing process was needed to fabricate the MWCNT electrode, indicating the simplicity of our method. Additionally, the apparatus enabled the reaction of up to 50 mg for each anodic oxidation (**Figure 3.4**). Further, reactor engineering such as increasing the lateral size of the reactor and using an electrochemically inert current collector (e.g. boron-doped

diamond)[43] would realize kilogram-scale preparation of GNRs using the electrochemical approach.

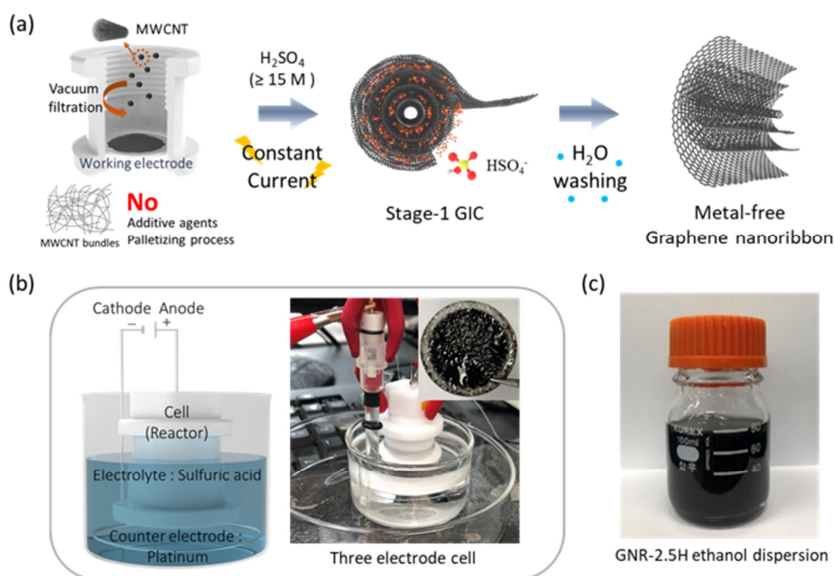


Figure 3.3. (a) Schematic representation of electrochemical process for unzipping MWCNT, (b) Schematic illustration of a designed cell for electrochemical unzipping of MWCNT and Photograph of the three-electrode cell used to perform the electrochemical reaction (inset: Photograph showing the MWCNTs after the unzipping process), and (c) GNR-2.5H

dispersion in ethanol (0.5 mg mL^{-1}) obtained by galvanostatic charging and washing processes for 2.5 hours.

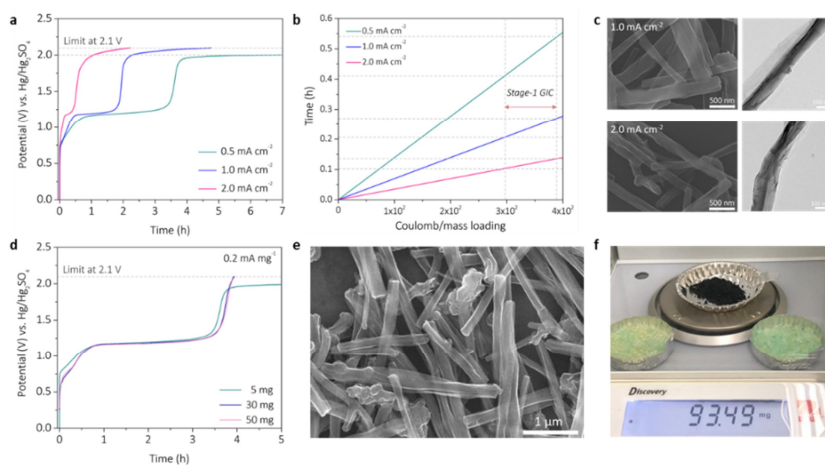


Figure 3.4. Electrochemical measurements of MWCNT in 18 M H₂SO₄ electrolyte. (a) Galvanostatic charge curve at various charging current densities (0.5 , 1.0 , and 2.0 mA cm^{-2}), (b) Time potential versus plotted Coulomb/mass loading during the electrochemical reaction, (c) SEM images of the related byproducts (current density: 1.0 and 2.0 mA cm^{-2}), (d) Galvanostatic charging curve of MWCNT with a current density of 0.2 mA mg^{-1} in 18 M H₂SO₄ electrolyte at different mass loading, (e) SEM images obtained after electrochemical reaction

for 2.5 hours, and (f) Milligram-scale synthesis of GNR-2.5H was done in the laboratory.

Figure 3.1b and **3.2** shows the anodic oxidation processes. The assembled MWCNT electrode was anodically oxidized in a two-electrode setup with a concentrated sulfuric acid (18 M) as an electrolyte and a platinum wire as a counter electrode. Concentrated sulfuric acid could be recycled for further reactions if the MWCNTs used for the reaction contains less impurities (**Table 3.1**). Constant current density of 0.5 mA cm^{-2} (or 0.2 A g^{-1}) was applied for different reaction times (0.5 h, 2.5 h, 4 h, and 7 h). For all reactions, the potential was limited to 2.1 V for safety purposes, as gas evolution became too pronounced above 2.1 V (**Figure 3.4**). GNRs were obtained by simply quenching the anodically oxidized MWCNTs with water. Water-quenched GNRs were then collected by filtration and thoroughly washed with deionized water. The yield was calculated by drying and weighing the filter cake. Nearly 100% production yield was obtained with our electrochemical unzipping method. Dried GNRs were re-dispersed in ethanol for further analysis (**Figure 3.3c**).

The unzipping degree of GNRs was tuned by simply changing the reaction time. GNRs obtained at different anodic oxidation time were denoted as GNR-2.5H, GNR-4H and GNR-7H. The GNR morphology was analyzed via scanning electron microscopy (SEM) and transmission electron microscopy (TEM) (**Figure 3.5**). Unlike pristine MWCNTs (**Figure 3.5a**), GNR-2.5H show MWCNTs with several longitudinal cuts. (**Figure 3.5b and f**) However, the GNRs remained foliated. I also observed longitudinal unzipping on MWCNTs that were anodically oxidized for 0.5 h (**Figure 3.6**). This result agrees with those of previous studies on intercalation-driven MWCNT unzipping[17,42]. GNRs lying on the substrate began to appear in GNR-4H (**Figure 3.5c and g**), and numerous GNRs were observed in GNR-7H (**Figure 3.5d and h**). GNR-7H comprising a few sheets was observed, indicating that further anodic oxidation reaction exfoliates GNR sheets into a few layers.

Sample	Fe [ppb; $\mu\text{g kg}^{-1}$]
1. MWCNT: 2 days	6.8

Table 3.1. The concentration of Fe element determined by ICP-MS measurement.

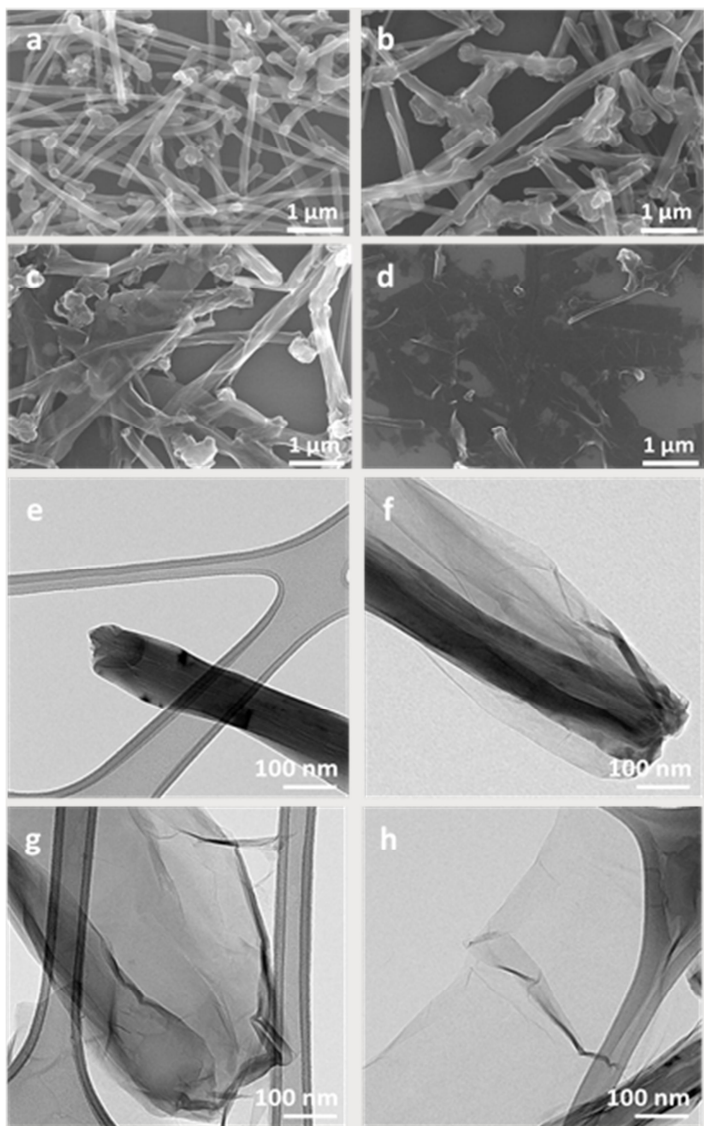


Figure 3.5. Morphology characterization of GNRs at various potential: SEM and TEM images of a, e) pristine MWCNT, b, f) GNR-2.5H, c, g) GNR-4H and d, h) GNR-7H, respectively.

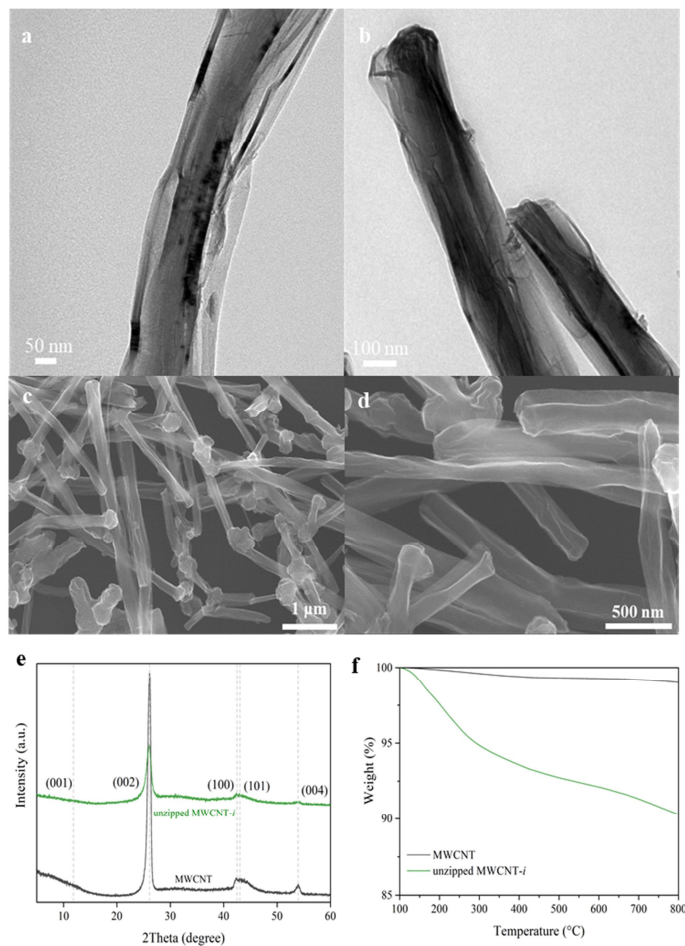


Figure 3.6. Material characterizations of the unzipped MWCNT. (denote as unzipped MWCNT-*i*) (a) and (b) TEM images, (c) XRD patterns, (d) and (e) SEM images, and (f) TGA curves. The weight loss of unzipped MWCNT-*i* observed at 800 °C is approximately 9.7 wt%.

I further investigated the effect of the current density and type of MWCNT on the electrochemical unzipping reaction (**Figure 3.4**, **Figure 3.7**, and **Figure 3.8**.) At higher current rates (1.0 and 2.0 mA cm⁻²), the time it takes to reach 2.1 V significantly decreased. Longitudinal unzipping was still observed in both cases, but GNR sheets were still attached to the MWCNT, implying that electrochemical reactions related to unzipping of MWCNT is faster than the reaction related to MWCNT exfoliation. When MWCNTs with various sizes were anodically oxidized, unzipping was observed on those with diameters larger than 20 nm (**Figure 3.7** and **Figure 3.8**).

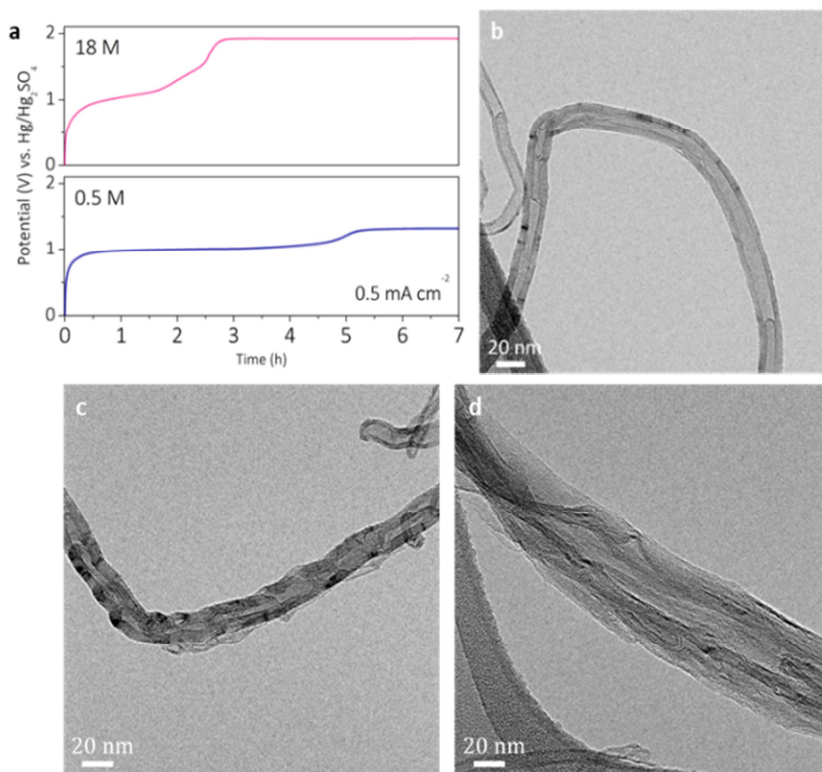


Figure 3.7. (a) Galvanostatic charge curve at current density of 0.5 mA cm^{-2} . (b) TEM images of pristine S-MWCNT, (c) surface oxidation of S-MWCNT performed in $0.5 \text{ M H}_2\text{SO}_4$ electrolyte, and (d) partially unzipped GNR performed in $18 \text{ M H}_2\text{SO}_4$ electrolyte.

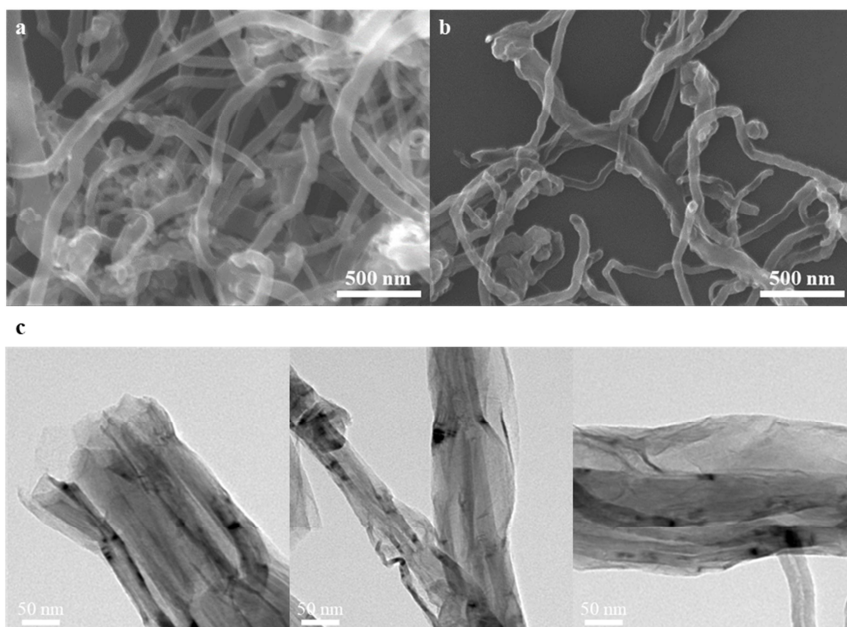


Figure 3.8. SEM image of (a) pristine M-MWCNTs. (b) and (c) SEM and TEM images of the partially unzipped GNR. The electrochemical charge reaction was performed in 18 M H_2SO_4 electrolyte at a current density of 0.5 mA cm^{-2} for 2.5 hours.

3.3.2. Physical and Chemical Characterization of GNRs

GNRs were investigated with X-ray diffraction (XRD) analysis to study the structure of the GNRs (**Figure 3.9a**). Pristine MWCNTs show a dominant peak at the (002) position, indicating the material has a highly graphitic structure. MWCNTs reacted for 0.5 h shows (002) and (004) peaks with decreased intensity, but the intensity is still greater compared to those of the GNRs (**Figure 3.6c**). Product is called as “unzipped MWCNT-*i*” in order to distinguish it from GNRs. By matching these results with the TEM observations (**Figure 3.6f, g, and h**), I speculated that layer stacking in GNR-2.5H is more disordered than that of unzipped MWCNT-*i* even when the morphologies of unzipped MWCNT-*i* and GNR-2.5H appear to be same. The (002) diffraction peak became obviously broad and weak with increasing reaction time, and the (004) diffraction peak was absent in the GNRs (**Table 3.2**). This observation indicates that long range (greater than four layers) order does not exist in the GNR sublattice. For all GNR products, (101) peak intensity decreased, which may be due to either

decreased translational order between the adjacent graphitic layers[44] or the removed catalyst residues from the MWCNT (**Figure 3.9b**)[45]. As the reaction prolonged for more than 4 hours, diffraction peaks related to the graphite oxide phase appeared in both the GNR-4H and GNR-7H samples.

The degree of oxidation was explored by Raman spectroscopy, X-ray photoelectron spectroscopy (XPS), and thermogravimetric analysis (TGA). In the Raman spectra, all GNRs show a clear G band at 1570 cm^{-1} (**Figure 3.9b**), indicating existence of graphitic phase in all samples. Importantly, the intensity of the D and D' bands increased as the reaction time increased. Spectra for GNR-4H and GNR-7H show not only the intense D and D' bands but also broadened D and G bands, indicating the existence of graphite oxide phase in the samples. The increase in the degree of oxidation of the products was further investigated with TGA in a nitrogen atmosphere and with XPS. According to the TGA graph (**Figure 3.9c**), weight loss related to the degree of oxidation increased with the increasing charging potential. For example, unzipped MWCNT-*i* showed a total weight loss of 5 % between

100 °C to 300 °C and weight loss of unzipped MWCNT-*i* observed at 800 °C is approximately 9.7 wt%, whereas GNR-7H showed a weight loss of 27 % in this temperature region. The oxygen/carbon (O/C) ratio of GNR-2.5H, GNR-4H, and GNR-7H determined by XPS was 0.16, 0.22, and 0.24, respectively, indicating the increase in the degree of oxidation with respect to increasing electrochemical reaction time (**Figure 3.9d**). Additionally, C 1s spectra for the GNRs (GNR-2.5H, GNR-4H, and GNR-7H) consist of the strong peak at 284.5 eV related to C–C bonds and the shoulder peak at 286.8 eV related to C–O bonds (**Figure 3.10**). The peak at 284.5 eV broadened and the peak at 286.8 eV further grew with reaction time, which is due to an increase in the degree of MWCNT oxidation[46].

Table 3.2. The full width at half maximum (FWHM) of the pristine MWNCT and all products was evaluated from the width of (002) peak using MDI Jade 6 software for multiple Gaussian function. A wider value of FWHM (B_{size} , °) indicates that the oxidation of MWCNT decreased the degree of crystallinity.

Sample	FWHM B_{size} [°]
--------	----------------------------

1. MWCNT	0.68
2. unzipped MWCNT- <i>i</i>	1.14
3. GNR-2.5H	1.29
4. GNR-4H	1.41
5. GNR-7H	1.53

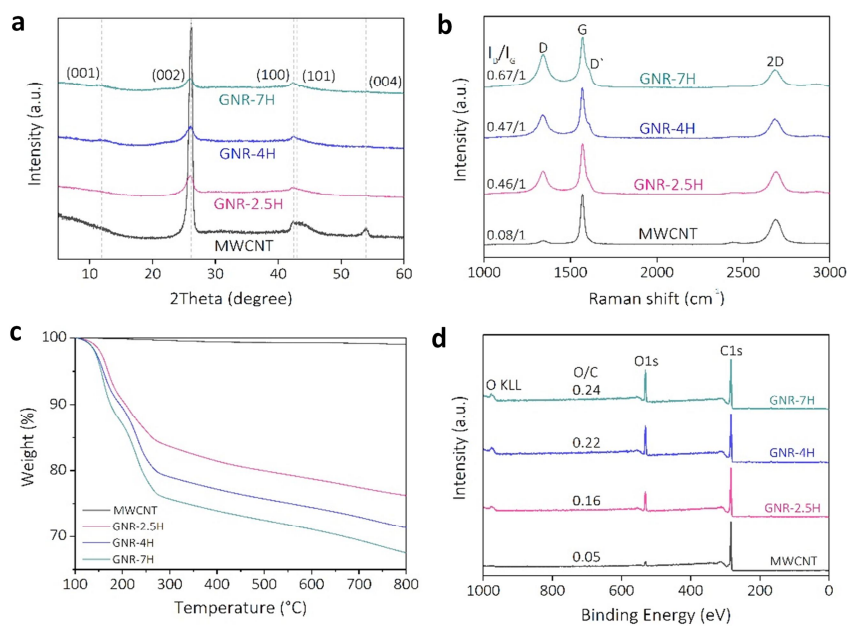


Figure 3.9. Physical and chemical characteristics of unzipped MWCNT products obtained at various potential: a) XRD patterns, b) Raman spectra, c) TGA curves for the decomposition of the products, and d) XPS spectra normalized to C1s intensity.

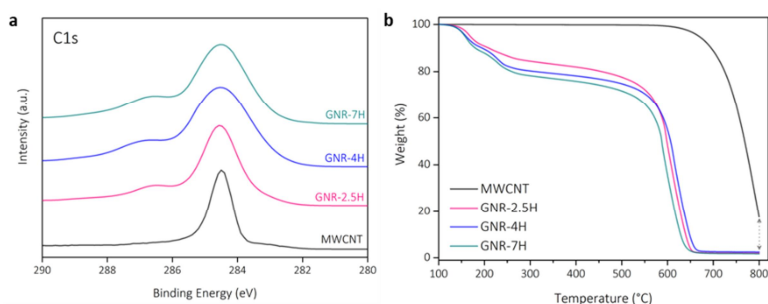


Figure 3.10. (a) High resolution XPS for C1s spectra of the as-prepared products and TGA thermogram of (b) concentrated sulfuric acid products. The thermogram of the products is obtained with a ramping rate of $10\text{ }^{\circ}\text{C min}^{-1}$ in air.

By increasing the anodic oxidation time, graphitic layer of MWCNT became more disordered, which matches with SEM and TEM analysis in **Figure 3.5**. Meanwhile, oxidation degree of GNRs increased respect to the anodic oxidation time. This implies that oxidation degree can be tuned by controlling the anodic oxidation time. Besides, Graphite oxide (GO) phase in GNR-4H, and GNR-7H indicates that graphitic layers in MWCNT needs to be significantly oxidized to GO in order to be exfoliated.

3.3.3. Mechanism of unzipping

For carbon with graphitic layers, including MWCNTs, the graphite intercalation compound (GIC) forms when intercalants are inserted between the graphitic layers of the host material[47,48]. The number of graphitic layers between the adjacent intercalant layers is defined as the stage number and, as such, the corresponding material is called stage-*n*-GIC. In order to investigate the structural evolution of MWCNTs during the anodic oxidation reaction, I performed *ex-situ* analyses, particularly, making use of Raman spectroscopy, XRD techniques, and optical microscopy at different charging times (0.5h: state-i, 2.5h: state-a, and 4h: state-b) using three-electrode setup with Hg/HgSO₄ as reference electrode and constant current density of 0.5 mA cm⁻² (**Figure 3.11a**). Interestingly, the charging curve does not show clear distinct potential steps below 1.24 V, which are related to the stage transformation of GIC (**Fig. 3.11b** and **Figure 3.12**).

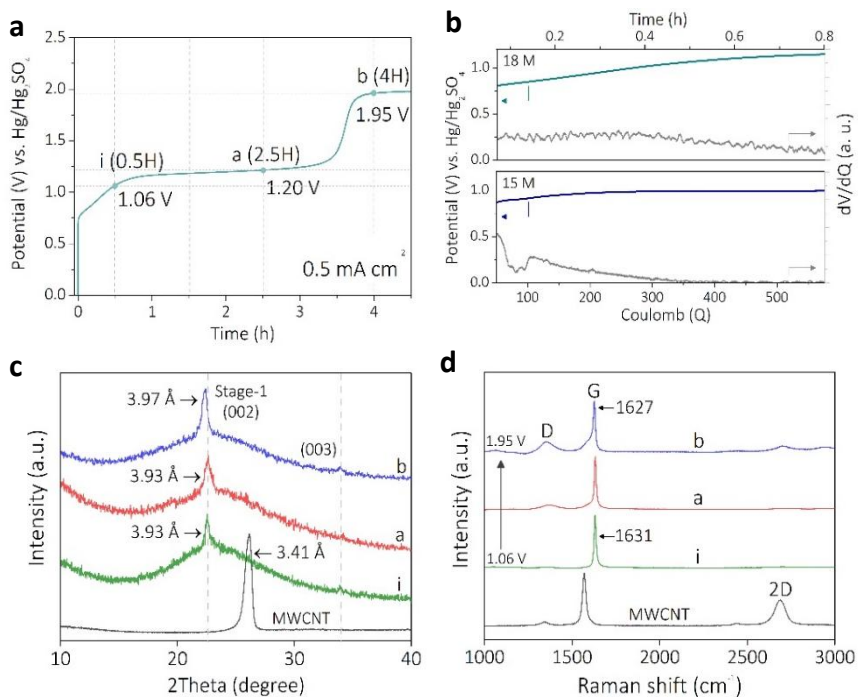


Figure 3.11. a) Galvanostatic charging curve of MWCNT working electrode with a platinum counter electrode and Hg/Hg₂SO₄ reference electrode, in 18 M H₂SO₄ electrolyte, recorded at current density of 0.5 mA cm⁻² at 25 °C. b) Cell potential (V) and derivative dV/dQ plotted versus Time (h) and Coulomb (Q). c) Raman spectra and d) XRD patterns of sulfuric

acid intercalated MWCNT formed at different voltage states (The broad background in XRD is due to the glass sample holder).

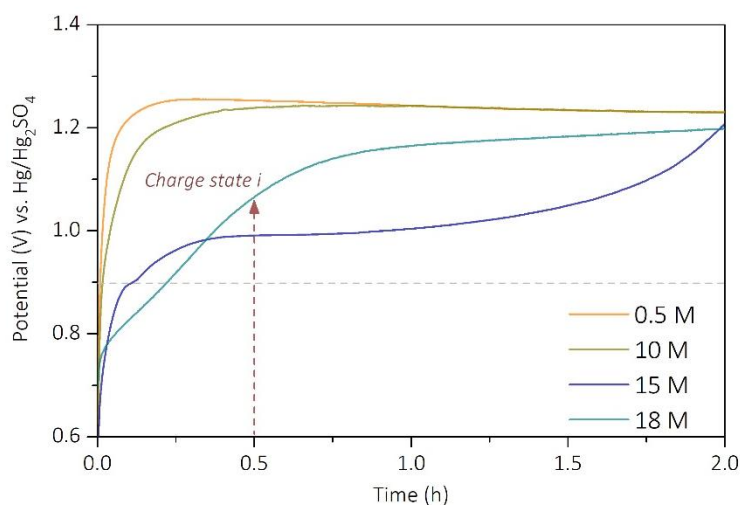


Figure 3.12. Galvanostatic charge (GC) curves for concentrations varying from 0.5 M to 18 M H_2SO_4 electrolytes.

XRD analysis confirmed the formation of GIC.⁵⁰ As shown in **Figure 3.11c**, the XRD spectra of all charged MWCNT samples show diffraction peaks at 22.5° , corresponding to the (002)

diffraction peak of stage-1-GIC H_2SO_4 .⁴² Interestingly, stage-1 GIC in the MWCNTs maintained its structure during the oxidation; there was no diffraction peak near 11.0° present on the graph. The observed difference was the broadening of the (002) diffraction peak, implying that the oxidation disordered the stage-1 GIC H_2SO_4 but was not sufficient to form a graphitic oxide phase. For instance, at state-a, where the oxidation of GIC was observed in the Raman analysis, the 22.5° peak became broad. Fig. 3.11d illustrates the acquired Raman spectra of MWCNTs at different potentials. At state-i the Raman graph shows a shifted G band at 1630 cm^{-1} and a decreased 2D band, which refers to stage-1 GIC. In state-a, the D band at 1370 cm^{-1} and a shoulder peak next to the G band at 1608 cm^{-1} appeared, which indicates oxidation or amorphization of stage-1 GIC. Further charging to state-b resulted in continued growth of the D band. This allowed me to speculate that the charges applied after state-i are used for oxidizing GIC. In the optical microscope, the color change of the MWCNTs from black to brown was observed as the charging time

increased from 0.5 h to 4 h, indicating oxidation of MWCNT have occurred (**Figure 3.13**).

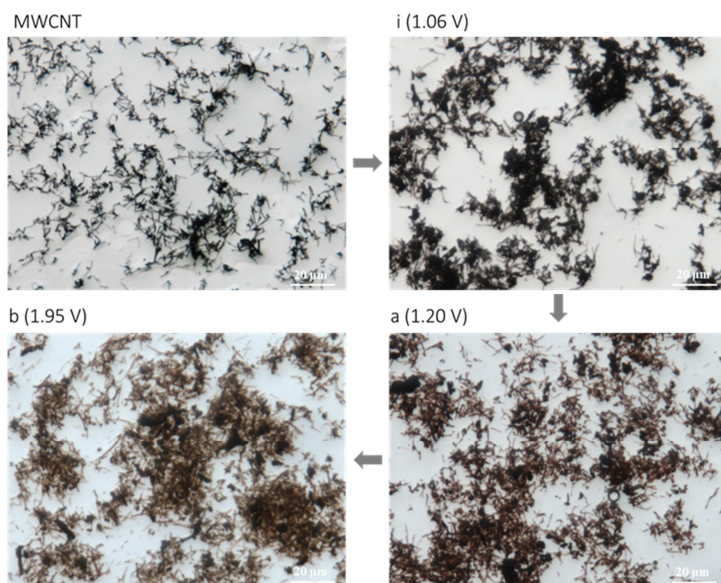


Figure 3.13. Ex-situ Optical microscope of MWCNTs with different charging states in concentrated H_2SO_4 electrolyte. The photographs of pristine MWCNT, charge states *i* (0.5 h), *a* (2.5 h), and *b* (4 h) shows grayish-blue, dark-navy, reddish-brown, and darkish-brown colors, respectively.

Electrolyte concentration is important factor for intercalation in aqueous electrolytes. When the graphitic material is subject to anodic oxidation in sulfuric acid with concentration higher than 15 M, the bisulfate molecules are inserted into the galleries of graphite, and low-stage GIC ($n \geq 2$) forms [51,52]. It has been reported that anodic oxidation of carbons in diluted acid generates oxygen and hydroxyl radicals. The driving force of anodic oxidative unzipping is reported to be oxidative cleavage of C–C bonds by these radicals [33,34]. However, these radicals are non-selective, which makes the anodic oxidative method unreliable to induce longitudinal cuts on the MWCNT.

To demonstrate the role of electrolyte concentration on unzipping, I used different concentrations (0.5 M, 10 M, 15 M, and 18 M) of electrolytes for unzipping MWCNTs. **Fig. 3.14.** shows the galvanostatic oxidation curves of MWCNTs in concentrations

ranging from 0.5 M to 18 M at a current density of 0.5 mA cm^{-2} . The onset potential increases with decreasing electrolyte concentration, which follows the Nernstian behavior (**Figure 3.14**). According to the electrochemical result, the concentration of the electrolyte had a pronounced effect on the appearance of the charging curves. Interestingly, the charging curve for 15 M concentration exhibits several distinct potential steps related to the stage transformations of GIC, oxidation, and hydrolysis [47,51]. For carbon with concentric walls, the structure must be unzipped (or fractured) in order for the intercalation to begin, which is also mentioned in the recent report by Dimiev et al.[42] The clear distinct potential steps below 1.24 V in 15 M may be interpreted as the role of water in intercalating sulfuric acid. For the charging curve of 15 M, the charging time to reach a potential above 1.20 V increased compared to that at 18 M, which could be attributed to the increased side reactions including water oxidation and carbon oxidation. I speculate that these side reactions generated defects on MWCNT and helped intercalate sulfuric acid, which resulted in the appearance of potential steps related to stage

transformation. However, a more detailed analysis is required to confirm this speculation.

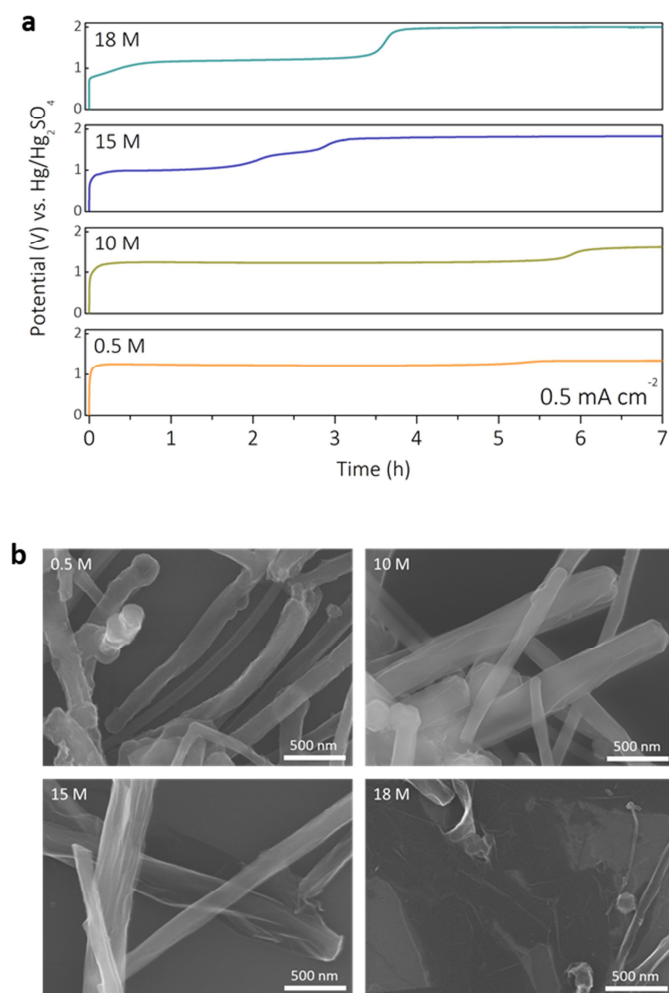


Figure 3.14. a) Galvanostatic charging curves of MWCNT working electrode with a platinum counter electrode and

Hg/Hg₂SO₄ reference electrode at different H₂SO₄ concentrations at a current density of 0.5 mA cm⁻² for 7 hours and b-e) their SEM images.

For the 0.5 M and 10 M sulfuric acid electrolytes, the potential reached 1.25 V without clear distinct potential steps; the difference between the two concentrations is that the potential of the latter increases more rapidly (**Figure 3.14a.**). The more rapid increase in potential in 0.5 M compared to that in 10 M is attributed to decreased overpotential for water oxidation or carbon oxidation reactions due to the increased water content.

Figure 3.14b. shows the scanning electron microscope (SEM) images of anodically oxidized MWCNTs in 0.5 M, 10 M, and 15 M, and 18 M sulfuric acid for 7 hours. A successful unzipping of MWCNTs is identified in the 15 M and 18 M products. Particularly for the 18 M product, numerous few-layered GNRs lying flat on the substrate are observed. For the 0.5 M and 10 M products, the MWCNTs appear to be intact.

The results agree well with the XRD data, where a long-range order along the (002) or (004) direction is related to the increase

in exfoliation degree with increasing concentration of the electrolyte (**Figure 3.15**). According to XRD data, a long-range order along the (002) or (004) direction decreased with the increasing concentration of the electrolyte. XRD data of 15 M GNR-7H product showed diffraction peak related to graphene oxide (near $\sim 10^\circ$), which was also observed in Raman observation. In Raman analysis, 0.5 M Ox-MWCNT-7H product shows the lowest I_D/I_G ratio. The FT-IR spectra of all products reveal the presence of sp^3C-H and sp^2C-H stretching band around 2922 cm^{-1} (dashed-box line), which presumably exhibit defects in the graphitic domains (**Figure 3.15c**). High oxidation levels (C-O-C stretch at 1250 cm^{-1} and C-O stretch at 1050 cm^{-1}) of 18 M GNR-7H and 15 M GNR-7H products may be due to the formation of GNR edges.

Transmission electron microscopy (TEM) investigation revealed changes in the 0.5 M and 10 M products after the anodic oxidation reaction; the latter shows MWCNTs with rough side walls, and the former shows a smooth surface (**Figure 3.16** and **Figure 3.17**). TGA curves, as shown in **Figure 3.18**, indicate that

the weight loss of products related to the oxidation degree decreased with the decrease in the concentration of electrolytes. Moreover, 0.5 M Ox-MWCNT-7H shows the lowest oxidation degree of ~10 wt% loss between 100 °C and 800 °C, which is even lower than the oxidation degree of GNR-2.5H (**Figure 3.18a**). The products reacted in different electrolyte concentrations were investigated with TGA analysis in the air to compare the remaining residual metallic impurity in MWCNT. Leached metal impurities were also observed during the investigation of unzipped MWCNT-*i* via Inductively Coupled Plasma Atomic Emission Spectroscopy (ICP-MS) (**Table 3.2**). Additionally, all products except those for the 0.5 M concentration showed decreased metallic impurities (approximately less than 2 wt% (**Figure 3.18b**)).

The detailed morphologies of the 0.5 M and 18 M products were characterized by high-resolution TEM (HR-TEM). Direct observation with HR-TEM revealed that GNRs lying flat on the substrate in the 18 M product consist of approximately three layers (**Figure 3.19a and b**). For the 0.5 M product, HR-TEM

revealed that the rough side walls consist of randomly cleaved graphene layers, which is the result of the random cleavage of C–C bonds by the radicals generated from the water oxidation reaction (**Figure 3.19c and d**). Moreover, it was found that the cleaved carbon layers in the 0.5 M-treated MWCNTs are nearly 5 nm and the rest of the MWCNTs remain constant which was also verified in the XRD analysis (**Fig. 3.15**).

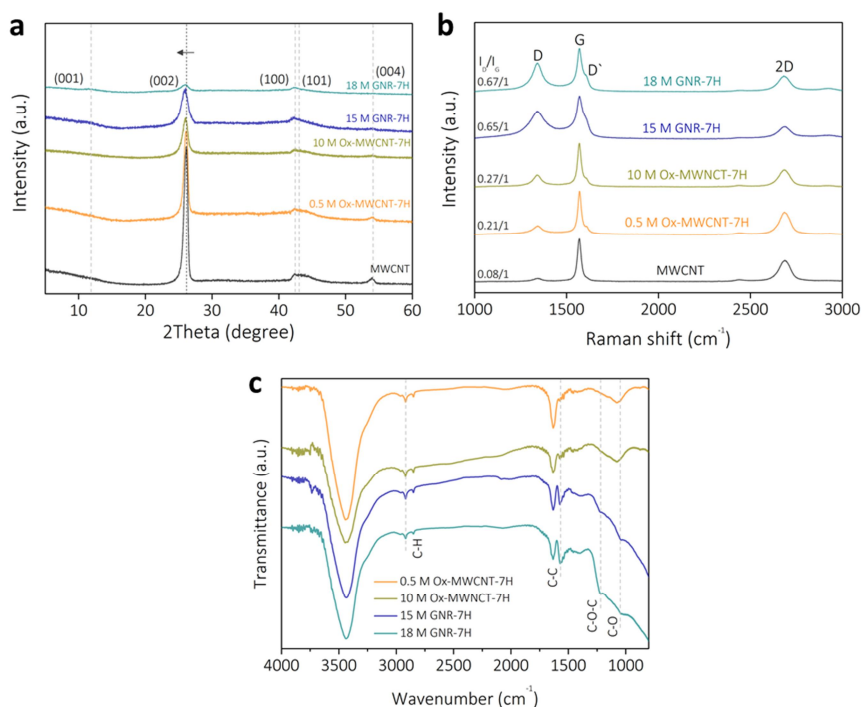


Figure 3.15. Characterization of products obtained by

electrochemical reactions at different concentrations of H_2SO_4 . (a) X-ray diffraction analysis, (b) Raman spectra, and (c) FT-IR spectroscopy.

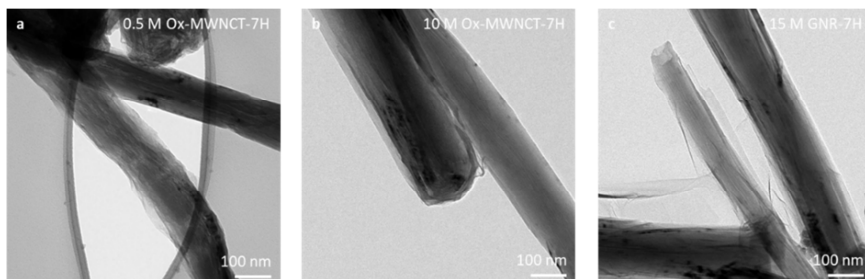


Figure 3.16. TEM images of the as-prepared products without caps; (a) 0.5 M Ox-MWNCT-7H, (b) 10 M Ox-MWNCT-7H, and (c) 15 M GNR-7H.

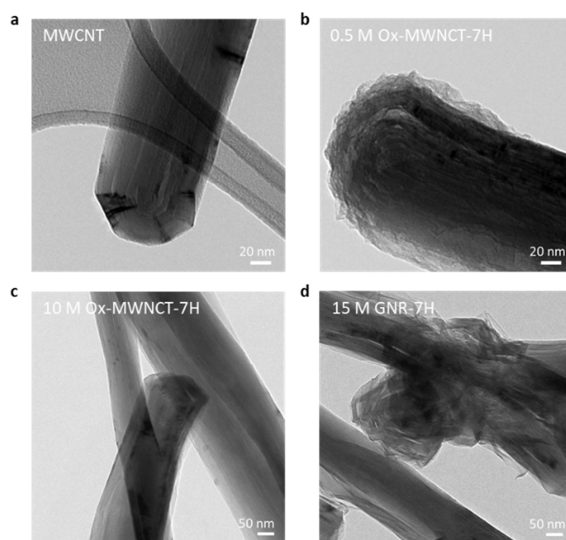


Figure 3.17. TEM images of the as-prepared products caps; (a) MWCNT, (b) 0.5 M Ox-MWNCT-7H, (c) 10 M Ox-MWNCT-7H, and (d) 15 M GNR-7H.

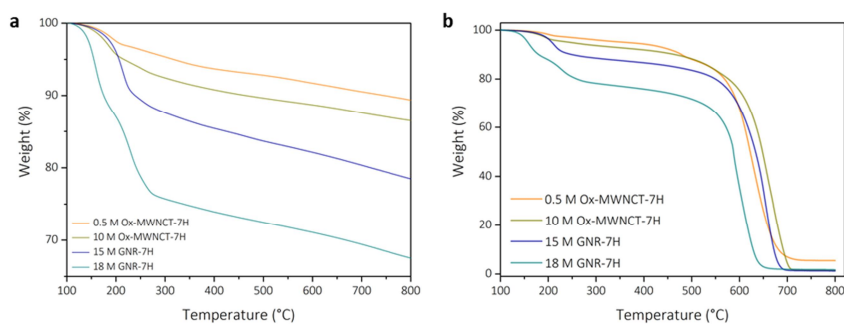


Figure 3.18. The thermogram of the products is obtained by the different concentration of sulfuric acid with a ramping rate of 10

°C min⁻¹ in N₂ and Air atmosphere; (a) N₂ and (b) Air.

Table 3.3. Detailed oxidation levels of the products in different electrolyte concentrations analyzed by XPS and TGA curves.

Sample	0.5 M Ox-MWCNT-7H	10 M Ox-MWCNT- 7H	15 M GNR- 7H	18 M GNR- 7H
XPS analysis				
Elemental composition	0.17	0.16	0.20	0.24
O/C [at %]				
TGA [%] ^{a)}	10.4	13.5	21.6	32.47

^{a)}(TGA [%] weight loss (%) from 100 to 800 °C under N₂ atmosphere.)

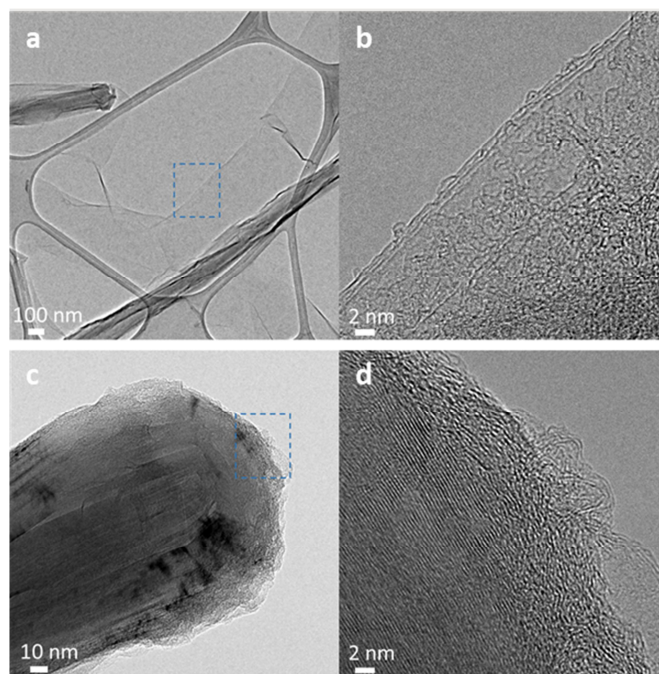


Figure 3.19. Characterization on morphology of (a-c) GNR (denoted as a GNR-7H) in 18 M H_2SO_4 and (e-g) oxidized MWCNT reacted in 0.5 M H_2SO_4 : a) and e) TEM, b) and f) High resolution TEM (HR-TEM) images of corresponding the blue dashed square in a) and e), c) and g)

Electron energy loss spectroscopy (EELS) was used to determine the surface chemical state of the 0.5 M and 18 M products (**Figure 3.20**). EELS can analyze the carbon K-edge consisting of the π^* and σ^* characteristic peaks of sp^2 carbon. The EELS

spectra of the edge (point 2) and basal plane (point 1) of the 18 m product consist of broad π^* and σ^* peaks, indicating that the loss of sp² carbon bonds or oxidation occurred uniformly on the few-layered GNRs. In comparison, the EELS spectrum of the side wall (point 2) of the 0.5 M-treated MWCNTs shows a broad π^* peak at 285.0 eV and a σ^* peak at 292.7 eV. However, unlike the side wall, narrow π^* and σ^* peaks are observed inside (point 1), indicating that the loss of the sp² carbon structure occurred on the MWCNT side walls. The observations above indicate that the mechanism of unzipping in this study is intercalation driven. Few-layered GNRs obtained through the anodic oxidation of MWCNTs in concentrated sulfuric acid (≥ 15 M), zipped MWCNTs observed in the 10 M product, and corroded MWCNTs observed in the 0.5 M product indicate the effectiveness of our electrochemical method.

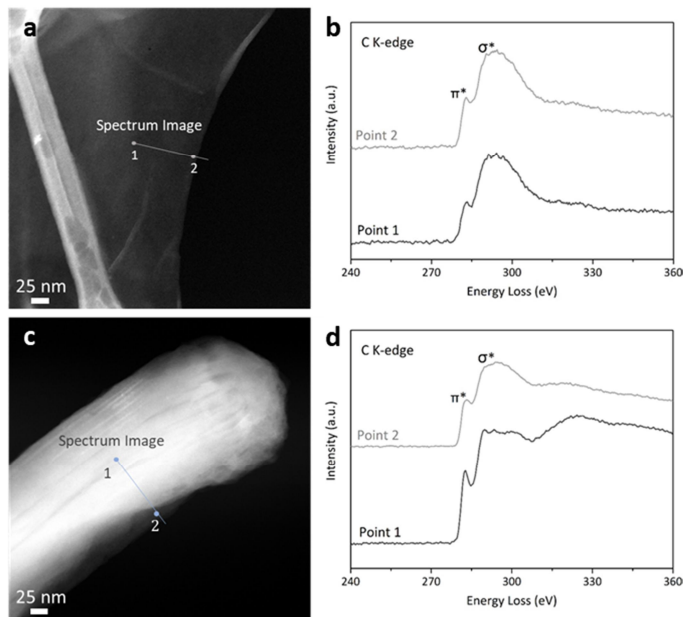


Figure 3.20. Aberration-corrected scanning transmission electron microscope (STEM) and a) and c) Electron energy-loss spectroscopy (EELS) spectra obtained from the selected points 1 and 2 in b) and d) respectively.

3.3.4. Applications

As examples, I demonstrated the use of GNR-*a* produced with 50 mg of loading mass to fabricate an alkali-ion capacitor. Surface area and electrical conductivity are important factors for capacitor applications. The Brunauer–Emmett–Teller (BET) specific surface area of GNR-*a* was determined to be $30 \text{ m}^2 \text{ g}^{-1}$, which is 2.5 times that of MWCNTs (**Figure 3.21**). I also measured the electrical resistivity of GNR-*a*. GNR-*a* shows slightly increased resistivity compared with that of pristine MWCNTs, even after 2.5 h of anodic oxidative reaction (**Table 3.4**).

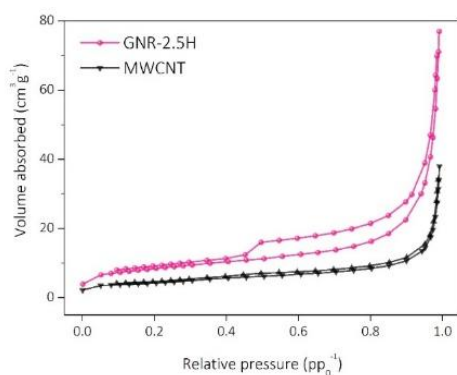


Figure 3.21 Brunauer–Emmett–Teller (BET) surface areas of

MWCNT and GNR-2.5H.

Table 3.4. The sheet resistance of the samples was investigated by a four-point probe measurement. This shows that the level of oxidation affects the conductivity of products.

Sample	Sheet resistance [$\Omega \text{ sq}^{-1}$]
1. MWCNT film	18.19
2. GNR-2.5H film	35.46

Alkali Ion capacitor

GNR-*a* with disordered structure and increased surface area was tested against the pristine MWCNTs as anodes for non-aqueous lithium ion capacitor (**Figure 3.22a–c**) and aqueous potassium ion capacitor (**Figure 3.22d–f**). **Fig. 3.22a** and **3.22b** shows the charge/discharge profiles of GNR-*a* and MWCNTs in lithium based organic electrolyte. The irreversible capacity during the first cycle is related to formation of a solid electrolyte interphase (SEI) layer. The larger irreversible capacity of GNR-*a* compared to that of MWCNTs may indicate that unzipping

increased the surface area available for growth of the SEI layer. After three cycles, both the MWCNT and GNR-*a* samples exhibited similar charge/discharge profiles. The discharge profile was distinguished with two different regions: The first region, between 2.5 V and 0.5 V, and a plateau below 0.5 V. The potential region lower than 0.5 V is related to a lithium intercalation reaction to form GICs, whereas the potential above 0.5 V is related to a faradaic reaction either on the graphene edges or the basal plane.[57] Interestingly, for GNR-*a*, most of the capacity originated from the potential region above 0.5 V, which may be due to the partially disordered and unzipped structure, exposing the GNR surface and edge planes. GNR-*a* shows specific capacities of 252.9 mA h g⁻¹ at a current density of 0.2 A g⁻¹ and remains at 75.6 mA h g⁻¹ when the current density increases to 4 A g⁻¹. The MWCNTs exhibit specific capacities of 180.5 mA h g⁻¹ at 0.2 A g⁻¹ and remains 12.6 mA h g⁻¹ at 4 A g⁻¹. As an anode for potassium ion capacitor (**Figure 3.22d–f**), GNR-*a* exhibits high reversible specific capacities of 238.0 F g⁻¹ at a current density of 0.5 A g⁻¹, which is larger than that of

MWCNTs (160.0 F g^{-1} at 0.5 A g^{-1}). The cyclic voltammetry curve of GNR-*a* possesses a nearly rectangular shape at a scan rate of 50 mVs^{-1} and maintains the shape at a scan rate 500 mVs^{-1} .

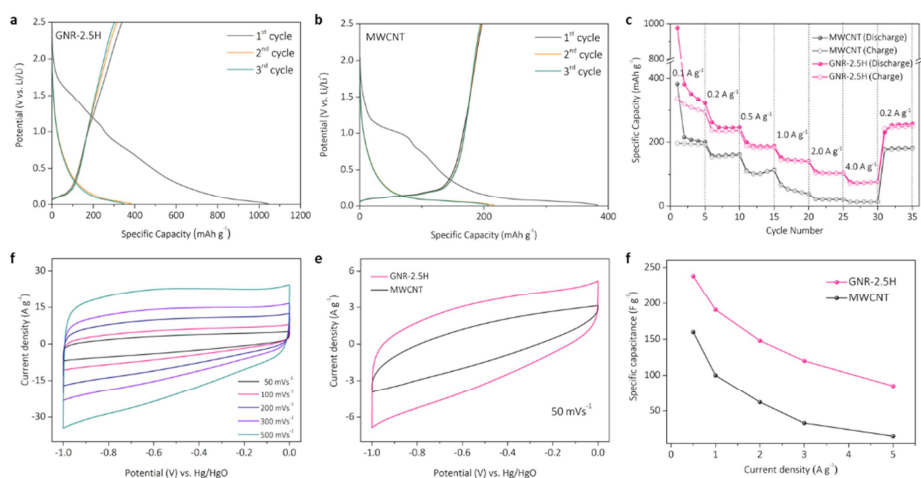


Figure 3.22. (a-f) Electrochemical measurements of the alkali-ion capacitor: (a-c) Li-ion capacitor and (d-f) K-ion capacitor. a, b) Charge/discharge curves of MWCNT and GNR-2.5H for first three cycles and c) Rate performance of MWCNT and GNR-2.5H

at various current densities. (d-f) Electrochemical double-layer capacitance (EDLC) performances of MWCNT and GNR-2.5H in a three-electrode system: d) Cyclic voltammetry (CV) curves at scan rate of 50 mV s^{-1} , e) CV curves of GNR-2.5H measured at various scan rates, and f) Specific capacitance at different current densities.

Catalyst support for hydrogen evolution reaction

Carbon nanomaterials such as graphene and carbon nanotubes have been proven to provide useful catalyst support for HER.[53,54] GNR-2.5H obtained from a 50-mg loading experiment showed a 2.5 fold increase in the specific surface area, but a slight increase in the resistivity when compared with that of the parent MWCNT (**Figure 3.21**), which makes GNR-2.5H an excellent candidate for HER catalyst support. I investigated the properties of GNR-2.5H as a catalyst support for HER by

depositing MoS₂ on GNR-2.5H. For comparison, MoS₂ was deposited on MWCNT and electrochemically exfoliated graphene (EEG) (**Figure 3.23**). As-prepared MoS₂-deposited GNR-2.5H, MWCNT, and EEG are denoted as MoS₂/GNR-2.5H, MoS₂/MWCNT, and MoS₂/EEG (**Figure 3.24**).

The HER properties of MoS₂/GNR-2.5H, MoS₂/MWCNT, and MoS₂/EEG were characterized by electrochemical measurements in a three-electrode setup with rotating glassy carbon disk as the working electrode, graphite rod as the counter electrode, and Ag/AgCl as the reference electrode. As shown in **Fig. 3.25a**, the polarization curve of MoS₂/GNR-2.5H shows an overpotential of 166 mV to achieve the current density of 10 mA cm⁻², which is lower than that of MoS₂/MWCNT (194 mV) and MoS₂/EEG (214 mV). Importantly, the HER reaction on MoS₂/GNR-2.5H is stable over several hours of continuous operation (inset in **Figure 3.25a**). **Fig. 3.25b** shows the Tafel slopes derived from the polarization curve. The Tafel slope of MoS₂/GNR-2.5H is 41 mV dec⁻¹, indicating that the electrochemical desorption of hydrogen atom is

the rate-limiting step [53]. The Tafel slopes for MoS₂/MWCNT and MoS₂/EEG are 53 mV dec⁻¹ and 43 mV dec⁻¹, respectively.

The electrochemical surface areas (ECSAs) of the synthesized samples were examined by calculating the double-layer capacitance (C_{dl}) in a non-Faradaic region (**Figure 3.25c** and **Figure 3.27**). MoS₂/GNR-2.5H possesses the highest C_{dl} (15.1 mF cm⁻²) value in comparison with MoS₂/MWCNT (9.4 mF cm⁻²) and MoS₂/EEG (0.6 mF cm⁻²). The relatively low ECSA of MoS₂/EEG is attributed to the serious stacking of EEG during the deposition of MoS₂ (**Figure 3.24b**). **Figure 3.25d** shows the Nyquist plots of the samples. The Nyquist plot of MoS₂/GNR-2.5H exhibits a semicircular shape, indicating the excellent electrical coupling between the catalyst and support [55]. Moreover, the Nyquist plot of MoS₂/GNR-2.5H has the smallest semicircle among the samples, indicating its low charge transfer resistance for HER.

By taking advantage of GNR with a quasi one-dimensional structure, MoS₂/GNR-2.5H exhibited higher catalytic

activity in terms of overpotential, Tafel slope, and charge transfer resistance than $\text{MoS}_2/\text{MWCNT}$ and MoS_2/EEG . The result highlights that GNR as a catalyst support not only decreases the contact resistance by providing better interfacial contact to the catalyst, but also provides an open structure with enhanced surface area, which leads to better performance than the MWCNT and EEG supports.

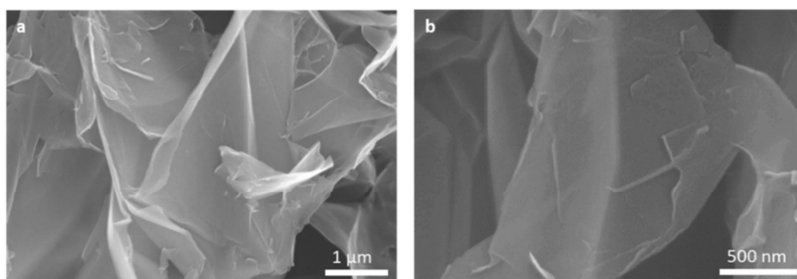


Figure 3.23. SEM images of the electrochemically exfoliated graphene (EEG); (a) Low and (b) High magnification.

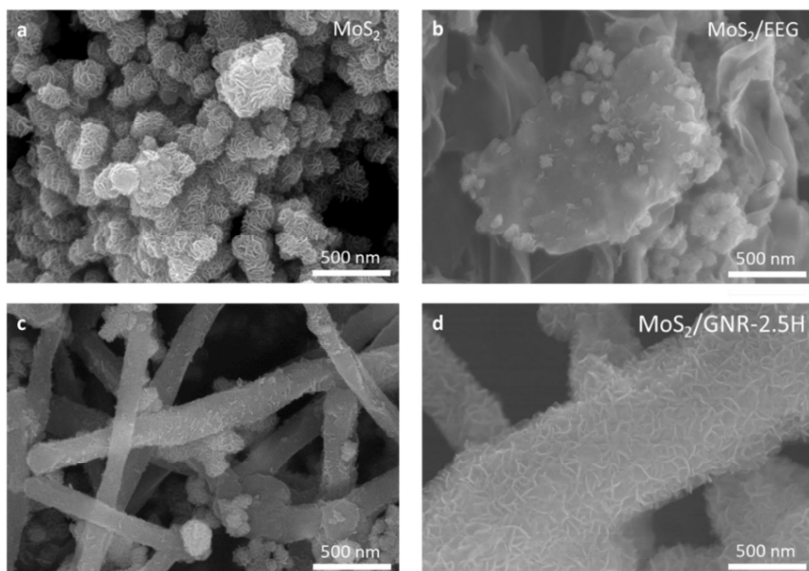


Figure 3.24. SEM images of (a) MoS₂, (b) MoS₂/EEG, (c) MoS₂/MWCNT, and (d) MoS₂/GNR-2.5H.

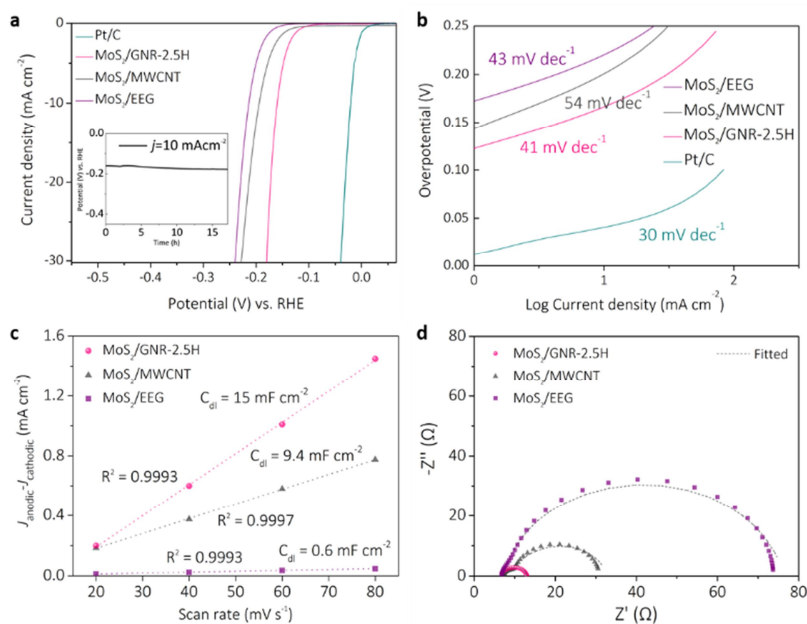


Figure 3.25. Electrochemical characterization of the as-prepared catalysts; (a) HER LSV curves at a scan rate of 2 mV s^{-1} in $0.5 \text{ m H}_2\text{SO}_4$ (Inset: long term stability test of the MoS₂/GNR-2.5H), (b) The corresponding Tafel plots of the catalysts. (c) Determined double layered capacitances (C_{dl}) performed by CV measurements, and (d) The electrochemical impedance spectroscopy (EIS) of the MoS₂/GNR-2.5H, MoS₂/MWCNT and MoS₂/EEG.

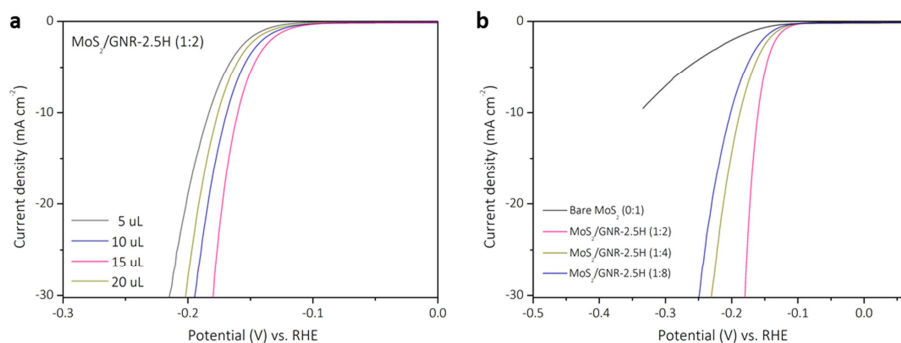


Figure 3.26. LSV curves at a scan rate of 2 mV s⁻¹ in 0.5 M H₂SO₄; (a) bare MoS₂ and MoS₂/GNR-2.5H according to the weigh ratio of the precursor (Ammonium tetrathiomolybdate, ATTm) and (b) the MoS₂/GNR-2.5H (1:2) at different mass loading.

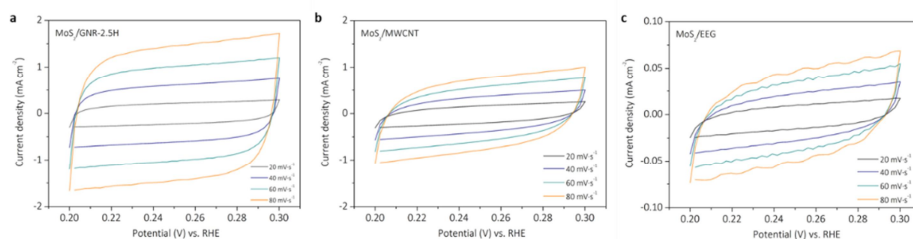


Figure 3.27. Cyclic voltammograms (CV) of (a) MoS₂/GNR-2.5H, (b) MoS₂/MWCNT, and (c) MoS₂/EEG recorded at scan rates of 20 to 80 mV s⁻¹.

3.4. Conclusion

In summary, I demonstrated synthesis of GNR by the anodic oxidation of MWCNTs in concentrated sulfuric acid which occurs through the intercalation mechanism. Highly concentrated sulfuric acid (≥ 15 M) plays a key role in longitudinal MWCNT unzipping. When diluted sulfuric acid is used for unzipping, intercalation is interrupted and the MWCNT side walls become randomly cleaved. The use of highly concentrated sulfuric acid enables the unzipping degree or oxidation degree to be tuned by simply altering the reaction time. Moreover, the approach enables the use of large amounts of MWCNT powders without any special interconnections, this is because the electrical conductivity of the electrode does not significantly decrease during the reaction, and gas evolving reactions can be avoided by precisely controlling the potential. Since the electrochemical reaction depends on the electrode area, large-scale GNR products can be realized by increasing the surface area or increasing the reaction rate by

increasing the current density. The use of sulfuric acid notwithstanding, strong reagents are not used; the synthesis is operated at room temperature and sulfuric acid was rendered recyclable. I also tested the versatility of our synthetic method by anodically oxidizing MWCNTs with different diameters; it was found that MWCNTs with diameters larger than 20 nm can be used as a parent material for production of GNRs (**Figure 3.7** and **Figure 3.8**). As demonstrated from the alkaline ion capacitor and catalyst experiments, the ability to produce graphene nanoribbons with unique properties on a large scale with a simple process will enable its application in a number of areas such as polymer composite materials, nanoelectronics and energy storage as well as conversion.

3.5. References

- [1] Li, X.; Wang, X.; Zhang, L.; Lee, S.; Dai, H. *Science*. **2008**, *319*, 1229.
- [2] Cai, J.; Ruffieux, P.; Jaafar, R.; Bieri, M.; Braun, T.; Blankenburg, S.; Muoth, M.; Seitsonen, A. P.; Saleh, M.; Feng, X. *Nature* **2010**, *466*, 470.
- [3] Rizzo, D. J.; Veber, G.; Cao, T.; Bronner, C.; Chen, T.; Zhao, F.; Rodriguez, H.; Louie, S. G.; Crommie, M. F.; Fischer, F. R. *Nature* **2018**, *560*, 204.
- [4] Wei, D.; Xie, L.; Lee, K. K.; Hu, Z.; Tan, S.; Chen, W.; Sow, C. H.; Chen, K.; Liu, Y.; Wee, A. T. S. *Nat. Commun.* **2013**, *4*, 1374.
- [5] Arias-Zapata, J.; Garnier, J. D.; Mehedi, H.; Legrain, A.; Salem, B.; Cunge, G.; Zelsmann, M. *Chem. Mater.* **2019**, *31* (9), 3154.
- [6] Gong, Y.; Fei, H.; Zou, X.; Zhou, W.; Yang, S.; Ye, G.; Liu, Z.; Peng, Z.; Lou, J.; Vajtai, R. *Chem. Mater.* **2015**, *27*, 1181.
- [7] Dou, S.; Tao, L.; Huo, J.; Wang, S.; Dai, L. *Energy Environ. Sci.* **2016**, *9* (4), 1320.
- [8] Wang, J.; Wu, Z.; Han, L.; Lin, R.; Xiao, W.; Xuan, C.; Xin, H. L.; Wang, D. *J. Mater. Chem. A* **2016**, *4*, 5678.
- [9] Yu, X.; Wang, B.; Gong, D.; Xu, Z.; Lu, B. *Adv. Mater.* **2017**, *29*, 1604118.
- [10] Li, L.; Raji, A. O.; Tour, J. M. *Adv. Mater.* **2013**, *25*, 6298.

- [11] Tan, K.; Liu, Y.; Tan, Z.; Zhang, J.; Hou, L.; Yuan, C. *J. Mater. Chem. A* **2020**, *8*, 3048.
- [12] Ujjain, S. K.; Ahuja, P.; Sharma, R. K. *J. Mater. Chem. A* **2015**, *3*, 9925.
- [13] Khandelwal, M.; Kumar, A. *J. Mater. Chem. A* **2015**, *3*, 22975.
- [14] Rafiee, M. A.; Lu, W.; Thomas, A. V.; Zandiatashbar, A.; Rafiee, J.; Tour, J. M.; Koratkar, N. A. *ACS Nano* **2010**, *4*, 7415.
- [15] Xiang, C.; Cox, P. J.; Kukovecz, A.; Genorio, B.; Hashim, D. P.; Yan, Z.; Peng, Z.; Hwang, C.-C.; Ruan, G.; Samuel, E. L. G. *ACS Nano* **2013**, *7*, 10380.
- [16] Kosynkin, D. V.; Higginbotham, A. L.; Sinitskii, A.; Lomeda, J. R.; Dimiev, A.; Price, B. K.; Tour, J. M. *Nature* **2009**, *458*, 872.
- [17] Kosynkin, D. V.; Lu, W.; Sinitskii, A.; Pera, G.; Sun, Z.; Tour, J. M. *ACS Nano* **2011**, *5*, 968.
- [18] Xu, X.; Ruan, S.; Zhai, J.; Zhu, H.; Yu, L.; Pei, J.; Cui, Z.; Zou, R.; Hu, J.; Lu, A.; Yu, M.; Tang, Z. *J. Mater. Chem. A* **2018**, *6*, 21327.
- [19] Silva-Santos, S. D.; Alencar, R. S.; Aguiar, A. L.; Kim, Y. A.; Muramatsu, H.; Endo, M.; Blanchard, N. P.; San-Miguel, A.; Souza Filho, A. G. *Carbon* **2019**, *141*, 568
- [20] Jeong, Y. C.; Lee, K.; Kim, T.; Kim, J. H.; Park, J.; Cho, Y. S.; Yang, S. J.; Park, C. R. *J. Mater. Chem. A* **2016**, *4*, 819.
- [21] Kim, W. S.; Moon, S. Y.; Park, N.-H.; Huh, H.; Shim, K. B.; Ham, H. *Chem. Mater.* **2011**, *23*, 940.
- [22] Kumar, P.; Yamijala, S. S. R. K. C.; Pati, S. K. *J. Phys. Chem. C* **2016**, *120*, 16985.

- [23] Morelos-Gómez, A.; Vega-Díaz, S. M.; González, V. J.; Tristán-López, F.; Cruz-Silva, R.; Fujisawa, K.; Muramatsu, H.; Hayashi, T.; Mi, X.; Shi, Y.; Sakamoto, H.; Khoerunnisa, F.; Kaneko, K.; Sumpter, B. G.; Kim, Y. A.; Meunier, V.; Endo, M.; Muñoz-Sandoval, E.; Terrones, M. *ACS Nano* **2012**, *6*, 2261.
- [24] Kim, K.; Sussman, A.; Zettl, A. *ACS Nano* **2010**, *4*, 1362.
- [25] Silva, A. A.; Pinheiro, R. A.; Rodrigues, A. C.; Baldan, M. R.; Trava-Airoldi, V. J.; Corat, E. J. *Appl. Surf. Sci.* **2018**, *446*, 201.
- [26] Yang, S.; Lohe, M. R.; Müllen, K.; Feng, X. *Adv. Mater.* **2016**, *28*, 6213.
- [27] Li, L.; Chen, L.; Mukherjee, S.; Gao, J.; Sun, H.; Liu, Z.; Ma, X.; Gupta, T.; Singh, C. V.; Ren, W.; Cheng, H.-M.; Koratkar, N. *Adv. Mater.* **2017**, *29*, 1602734.
- [28] Yang, S.; Zhang, P.; Wang, F.; Ricciardulli, A. G.; Lohe, M. R.; Blom, P. W. M.; Feng, X. *Angew. Chemie* **2018**, *130*, 15717.
- [29] Ambrosi, A.; Sofer, Z.; Pumera, M. *Angew. Chemie Int. Ed.* **2017**, *56*, 10443.
- [30] Yang, S.; Ricciardulli, A. G.; Liu, S.; Dong, R.; Lohe, M. R.; Becker, A.; Squillaci, M. A.; Samorì, P.; Müllen, K.; Feng, X. *Angew. Chemie Int. Ed.* **2017**, *56*, 6669.
- [31] Shinde, D. B.; Debgupta, J.; Kushwaha, A.; Aslam, M.; Pillai, V. K. *J. Am. Chem. Soc.* **2011**, *133*, 4168.
- [32] John, R.; Shinde, D. B.; Liu, L.; Ding, F.; Xu, Z.; Vijayan, C.; Pillai, V. K.; Pradeep, T. *ACS Nano* **2014**, *8*, 234.
- [33] Lim, J.; Maiti, U. N.; Kim, N.-Y.; Narayan, R.; Lee, W. J.; Choi, D. S.; Oh, Y.; Lee, J. M.; Lee, G. Y.; Kang, S. H.

- Nat. Commun.* **2016**, *7*, 10364.
- [34] Ohmori, S.; Saito, T. *Carbon* **2012**, *50*, 4932.
- [35] Zehtab Yazdi, A.; Roberts, E. P. L.; Sundararaj, U. *Mater. Res. Bull.* **2016**, *80*, 243.
- [36] Yi, Y.; Tornow, J.; Willinger, E.; Willinger, M. G.; Ranjan, C.; Schlögl, R. *ChemElectroChem* **2015**, *2*, 1929.
- [37] Lu, X.; Yim, W.-L.; Suryanto, B. H. R.; Zhao, C. *J. Am. Chem. Soc.* **2015**, *137*, 2901.
- [38] Senokos, E.; Rana, M.; Santos, C.; Marcilla, R.; Vilatela, J. J. *Carbon* **2019**, *142*, 599.
- [39] Debgupta, J.; Shinde, D. B.; Pillai, V. K. *Chem. Commun.* **2012**, *48*, 3088.
- [40] Sasikala, S. P.; Yun, T.; Choi, D. S.; Jeong, M. S. *ACS Appl. Mater. Interfaces* **2019**, *11*, 41, 38006.
- [41] Yu, P.; Tian, Z.; Lowe, S. E.; Song, J.; Ma, Z.; Wang, X.; Han, Z. J.; Bao, Q.; Simon, G. P.; Li, D.; Zhong, Y. L. *Chem. Mater.* **2016**, *28*, 8429.
- [42] Dimiev, A. M.; Khannanov, A.; Vakhitov, I.; Kiiamov, A.; Shukhina, K.; Tour, J. M. *ACS Nano* **2018**, *12*, 3985.
- [43] Lowe, S. E.; Shi, G.; Zhang, Y.; Qin, J.; Jiang, L.; Jiang, S.; Al-Mamun, M.; Liu, P.; Zhong, Y. L.; Zhao, H. *Nano Mater. Sci.* **2019**, *1*, 215.
- [44] Shih, C.-J.; Vijayaraghavan, A.; Krishnan, R.; Sharma, R.; Han, J.-H.; Ham, M.-H.; Jin, Z.; Lin, S.; Paulus, G. L. C.; Reuel, N. F.; Wang, Q. H.; Blankschtein, D.; Strano, M. S. Bi- and Trilayer Graphene Solutions. *Nat. Nanotechnol.* **2011**, *6*, 439.
- [45] Motta, M.; Moisala, A.; Kinloch, I. A.; Windle, A. H. *Adv. Mater.* **2007**, *19*, 3721.

- [46] Ganguly, A.; Sharma, S.; Papakonstantinou, P.; Hamilton, J. J. *Phys. Chem. C* **2011**, *115*, 17009.
- [47] Shioyama, H.; Fujii, R. *Carbon* **1987**, *25*, 771.
- [48] Besenhard, J. O.; Wudy, E.; Möhwald, H.; Nickl, J. J.; Biberacher, W.; Foag, W. *Synth. Met.* **1983**, *7*, 185.
- [49] Iwashita, N.; Shioyama, H.; Inagaki, M. *Synth. Met.* **1995**, *73*, 33.
- [50] Dimiev, A. M.; Ceriotti, G.; Behabtu, N.; Zakhidov, D.; Pasquali, M.; Saito, R.; Tour, J. M. *ACS Nano* **2013**, *7*, 2773.
- [51] Beck, F.; Jiang, J.; Krohn, H. *J. Electroanal. Chem.* **1995**, *389*, 161.
- [52] Kang, F.; Zhang, T.-Y.; Leng, Y. *Carbon* **1997**, *35*, 1167.
- [53] Li, Y.; Wang, H.; Xie, L.; Liang, Y.; Hong, G.; Dai, H. *J. Am. Chem. Soc.* **2011**, *133*, 7296.
- [54] Ekspong, J.; Sandström, R.; Rajukumar, L. P.; Terrones, M.; Wågberg, T.; Gracia-Espino, E. *Adv. Funct. Mater.* **2018**, *28*, 1802744.
- [55] Sun, Y.; Alimohammadi, F.; Zhang, D.; Guo, G. *Nano Lett.* **2017**, *17*, 1963

Chapter 4. Conclusion

In this Ph.D. thesis, electrochemical preparation of graphene and GNRs and their applications in energy storage/conversion applications have been demonstrated. Particular attention was given to the electrochemical preparation method, which has been regarded as a promising alternative to produce two-dimensional materials in liquid media.

In the second chapter of the thesis, I studied the anodic exfoliation of graphite in an aqueous inorganic sulfate salt. Anodically exfoliated graphene with moderate oxidation degree was used as a precursor and susceptor to prepare a carbon-coated silicon-graphene nanocomposite film. After a few seconds of microwave irradiation, partially oxidized EG absorbed the microwave radiation and generated heat to simultaneously reduce the graphene and carbonize the polydopamine carbon precursor. The as-prepared carbon-coated

silicon-graphene film was then used as a LIB anode and exhibited a reversible capacity of 1744 mAh g⁻¹ at a current density of 0.1 A g⁻¹ and 662 mAh g⁻¹ at 1.0 A g⁻¹ after 200 cycles. Thus, this method can potentially be a general approach to prepare various graphene nanocomposites in an extremely short time.

In the third chapter, electrochemical unzipping of MWCNTs was systematically studied. Previously, several electrochemical unzipping approaches have been proposed to unzip MWCNTs but most of them are unscalable or are incapable of selective unzipping. In this chapter, an electrochemical intercalation strategy under ambient conditions was presented for the scalable preparation of GNRs. When MWCNTs were anodically oxidized in a concentrated acid electrolyte, they became longitudinally unzipped as soon as the material was completely intercalated; furthermore, few-layered GNRs were formed by a subsequent anodic oxidation reaction. This method can control the C/O ratio from 4 to 20 and the GNR unzipping level from partial to full unzipping. Moreover, the method can be scaled up to a rate of 100 g h⁻¹ if a square meter-sized electrode is used with simple washing

processes. The as-prepared GNRs in this study were used as anodes for alkali ion capacitors in both organic and aqueous electrolytes and catalyst support for HER.

The studies presented in this thesis provide a deeper insight into the electrochemical methods, which may contribute to the development of possible solutions to enable commercialization of graphene- or graphene-related products. However, several challenges remain in electrochemical methods that have not been addressed in this thesis. One of the biggest challenges for electrochemical methods is the polydispersity in layer numbers, oxidation degree, or lateral sizes. This originates from the heterogeneous reactions in this system. Such challenge may be overcome by designing the optical cell architecture or coupling homogeneous chemical reactions to oxidation-reduction processes at the electrode surface. These strategies are challenging but are expected to make a breakthrough in the current electrochemical methods for preparing graphene, GNRs, or other two-dimensional materials.

국문초록

지난 10 년 동안 그래핀 기반 나노 물질들은 에너지 저장 및 전환 분야에서 우수한 물리적 및 화학적 특성으로 인해 연구가 활발히 이루어졌으나 높은 가격과 낮은 생산성으로 인해 상용화하기에는 어려움이 많았다. 현재 그래핀 및 그래핀 나노리본은 저렴하고 단순한 화학적 공정을 통해 합성할 수 있지만, 아직도 폭발의 위험성과 합성에 사용되는 강산화제 또는 강환원제로 인해 환경 오염을 유발시키는 문제점을 갖고 있다. 본 학위논문에서는 이러한 문제점들을 해결할 수 있는 전기화학법을 사용해 그래핀 및 그래핀 나노리본을 합성하였다.

첫번째 연구에서는 그래핀은 전기화학적 방법 중 하나인 산화 박리법을 이용해 합성되었다. 전기 화학적 박리된 그래핀은 마이크로파를 흡수하여 열을 발생시켰다. 발생된 열은 그래핀을 환원시켰고 동시에 실리콘 나노 입자에 코팅된 폴리 도파민 탄소 전구체를 탄화 시켰다. 탄소 코팅 된 실리콘 나노 입자-그래핀 복합체는 리튬 이온 배터리 음극으로 사용되었다. 다음으로는 전기 화학적 방법 중 하나인 삽입법을 사용하여 다중 벽 탄소 나노 튜브 (MWCNT)를 압축 해제(unzipping) 하였다. MWCNT가 진한 황산 전해질에서 전기화학적으로 산화될 때, 황산이 MWCNT 내부로 삽입되고, MWCNT가 압축 해제 되 그래핀 나노리본이 형성된다. 합성된 그래핀 나노리본은 유기와 수계 전해질에서 알칼리 이온 커패시터 전극, 수소 발생 반응을 위한 MoS_2 촉매 지지체로 사용되었다.

본 학위논문에서는 전기화학방법을 이용해 그래핀과 그래핀 나노리본을 합성하는 방법을 제시하였다. 본 연구의 결과들은 그래핀 나노물질들을 산업에 응용하는데

있어서 유용하게 사용될 수 있으며 실제 제품에서
적용되는 것을 앞당길 수 있을 것으로 기대한다.